Hawley, Ryan Daniel (2022) *Applications and practical considerations of polarisation structuring by a Fresnel cone.* PhD thesis.

https://theses.gla.ac.uk/82650/

Applications and practical considerations of polarisation structuring by a Fresnel cone

Ryan Daniel Hawley

A thesis submitted in fulfilment of the requirements for the degree of
Doctor of Philosophy

School of Physics and Astronomy
College of Science and Engineering
University of Glasgow

January 2022

Abstract

The polarisation property of light has been known about for hundreds of years. Often its use in technology has been limited to uniform states, however, more recently light with structured polarisation has gained interest. This is largely prompted by availability of spatial light modulators for generation, and increased computation speed to model complex focal fields. My PhD research has extended upon work carried out during a master's project where we investigated the use of a solid glass cone (so-called Fresnel cone) for generating vector vortex beams. The aim of this thesis is to report on the potential use of a Fresnel cone in microscopy and polarimetry applications, and practical implications discovered. Expanding on the previous work, enhanced fidelity polarisation states are measured and a newly developed Fresnel cone coupling technique is shown, allowing high-efficiency annular vector vortex beam generation. We demonstrate through simulations based on vector diffraction theory that azimuthally polarised light with OAM generated using a Fresnel cone can provide sub-diffraction limited focal spots, below those of more well-known radially polarised light. Practical implications were encountered, prompting investigation into the effects of phase aberrations on resulting focal spots, and experimental measurement of cone surface topology. We find the uniformity of the Fresnel cone shape and apex angle is crucial to the focussing properties. For polarimetry application, full details are provided for a single-shot full-Stokes polarimeter technique and proof-of-principle experiment, where broadband operation is demonstrated. I conclude by summarising the findings of my research and suggest potential future work in this area.

Contents

List of Figures

Acknowledgements

I would like to extend my deepest gratitude to my supervisor, Sonja Franke-Arnold, for the patient guidance and support given throughout my time as a student. Through the multitude of discussions in the lab, continual proof-readings of my work or the encouragement provided to believe in myself, I could not have asked for a better supervisor.

Secondly, I cannot begin to express my thanks to Neal Radwell for mentoring me from my first days in the Optics group. I am indebted for all the time given teaching me experimental optics, answering my many questions, and never going easy on me in '*Through the Ages*'.

Special thanks to my second supervisor, Caroline Muellenbroich, for advising me in microscopy and the experimental skills gained working together. I would also like to gratefully acknowledge Rachel Offer, Claire Cisowski and Graham Gibson for extensive assistance in the lab.

Aside from academic endeavors, I would like to thank everyone in the Optics group for making it such a friendly and welcoming environment. I am especially grateful to Adam Selyem, Francesco Castellucci, Daan Stellinga, Euan Cowie, Sara Restuccia, Kyle Nutt, Thomas Gregory and Steven Johnson for the many boardgame evenings!

Finally, the completion of this thesis would not have been possible without the incredible amount of support and encouragement from both my parents and my wife, Ugne - thank you.

This work was supported by the Engineering and Physical Sciences Research Council (EPSRC) Centre for Doctoral Training (CDT) in Intelligent Sensing and Measurement, Grant Number EP/L016753/1.

Declaration of Authorship

I hereby declare that this thesis is the result of my own work, except where explicit reference is made to the work of others, and has not been presented in any previous application for a degree at this or any other institution.

Ryan D. Hawley

Publications

The following is a list of papers and conference proceedings where I am either first author, or co-authored during my PhD. Where these are currently in preparation, this will be stated.

1. Hawley, R. D., Cork, J., Radwell, N., Franke-Arnold, S. ‘Passive broadband full Stokes polarimeter using a Fresnel cone.’ Sci Rep 9, 2688 (2019).
2. Hawley, R. D., Offer, R., Radwell, N., Franke-Arnold, S. ‘Tight focal spots using azimuthally polarised light from a Fresnel cone,’ Proc. SPIE 11359, Biomedical Spectroscopy, Microscopy, and Imaging, 1135910 (1 April 2020).
3. Hawley, R. D., Cisowski, C. M., Franke-Arnold, S. ‘High efficiency generation of annular vector vortex beams’ *Manuscript in preparation.*
4. Hawley, R. D., Offer, R., Franke-Arnold, S. ‘Tight focal spots using a Fresnel cone and their stability to phase aberrations’ *Manuscript in preparation.*

Below is a list of papers I have co-authored outside of my PhD work.

1. Radwell, N., Hawley, R. D., Götte, J. B., & Franke-Arnold, S. ”Achromatic vector vortex beams from a glass cone,” Nat. Commun. 7, 10564 (2016).

Chapter 1

Introduction

‘Everything starts somewhere, although many physicists disagree.’ - Terry Pratchett

1.1 The vector nature of light

The study of light is perhaps humanity’s oldest scientific endeavour. There is evidence for elementary optical theories dating back to the 5th-6th centuries B.C. originating separately in ancient India, China and Greece [1]. After the works of Euclid and Ptolemy in Greece on geometrical optics, a vast amount of knowledge on the behaviour of light was gained in the Islamic world over several hundred years, including a correct explanation of the rainbow (circa 900 A.D.) [2]. The following centuries saw the basic laws of reflection and refraction expanded upon, and employed practically in components such as lenses and mirrors, eventually culminating in inventions such as the telescope in 1608 [3].

The history of the vector nature of light however, began in 1669, when Rasmus Bartholin (1625-1698) discovered the phenomenon of double refraction of light by calcite [4]. Christiaan Huygens (1629-1695) was able to show that the twin beams refracted by calcite had a certain ‘sidedness’, though neither he, using a wave description of light, nor Isaac Newton (1642-1727) pursuing a corpuscular theory of light, could explain this [5]. It was not until a hundred years later or so that pivotal investigations by Étienne-Louis Malus (1775-1812) on the reflection of light also revealed this ‘sidedness’, and the term ‘polarisation’ was conceived. Following Huygens’ wave description of light, Thomas Young (1773-1829) reasoned that light behaves as a transverse wave, oscillating orthogonal to the direction of propagation. These discoveries led Augustin Jean Fresnel (1788-1827) to deduce his famous formulae for light's complex amplitude coefficients upon reflection and transmission [6]. Though the results of Fresnel are hundreds of years old, they are an important discovery and are in fact still useful in optics manufacturing and research today (see chapter 3).

With the first telescopes, the first microscopes were also developed during the 17th century, alongside the initial discoveries of polarised light. It was not until the mid-20th century however, that the mathematical techniques to calculate the effects of high-angle (non-paraxial) focussing on polarisation were developed, and so for a long time the effects of polarisation upon focussing were neglected. It was much later still that the computational power was available to model complex focal fields involving three-dimensional polarisation (where the longitudinal z-direction is considered). For a lens, a higher numerical aperture relates to a reduction in the resulting focal spot size, where often in applications it is desirable to obtain the smallest possible focal spot. Hence, widespread use of high numerical aperture lenses in both technology and research means that the effects of polarisation should not be ignored. Furthermore, investigations on the effects of polarisation in the non-paraxial regime have revealed that previously thought fundamental limits on focal spot volume to be surpassed (see chapter 4).

Though evidently known about since the times of Huygens and Newton, this vector property of light is only relatively recently finding application in both common and complex technology [7–10]. In order to work with polarisation it must be measurable, and while the measurement of intensity (brightness) and wavelength (colour) is well-understood and ubiquitously found in optical devices, polarisation is often neglected in the design of common detectors. This is largely due to conventional cameras and the human eye[1] being insensitive to electric field orientation, making measurement difficult. Polarisation characterisation is hence an active area of current research (see chapter 5).

---

[1] With the exception of 'Haidinger's brush' - an entoptic phenomenon whereby the eye produces a faint image of a fuzzy yellow bar (with orthogonal blue/purple bar) whose direction depends on polarisation!

1.2 Motivation for my research

1.2.1 Vector beams and the Fresnel cone

The ability to produce tailored light fields is not new, though for decades the customisation was limited to intensity patterns ignoring phase and polarisation. These were generated using amplitude masks [11] or diffractive optical elements [12], often for use in photolithography. Interestingly however, amplitude and phase are inherently linked in propagating beams through the phenomenon of interference. This is strikingly evident in the Talbot effect [13, 14] for example. Here, upon incidence at a diffractive grating element it is shown that periodic phase patterns evolve into intensity patterns and back - eventually re-imaging the original grating at a certain distance. Interest in the structuring of light's phase gained traction upon the discovery of light beams carrying orbital angular momentum (OAM) [15]. These OAM beams possess a helical phase front with a phase singularity on the optic axis (optical vortex), where the phase is undefined and the intensity goes to zero. Interesting beam structures have been subsequently studied, such as the optical 'bottle beam' [16] or 'Ferris wheel' [17]. In three dimensional space these vortices are lines, where more complicated optical knots and loops have also been shown [18]. This phase-structuring of light, while clearly very interesting to study, is also finding application in a range of areas from optical communications [19] to particle trapping [20].

Following the structuring of light's amplitude and phase it was inevitable that polarisation structuring would also emerge. In the past only beams with homogeneous polarisation states were considered, where the polarisation is unchanged across the beam's cross-section, while these structured polarisation beams (vector beams) have a spatially dependent state in the transverse plane. Anything deviating from a homogeneous state was previously considered unwanted and actually something to be fixed. Beams with polarisation structuring that also carry OAM are of particular interest (vector vortex beams), exhibiting classical entanglement [21–23]. The term classical entanglement here refers to the non-separability of these beams in their polarisation state and spatial distribution. Correlations akin to quantum entanglement are observed, however, an important distinction is the lack of non-locality [24]. Since the early 2000s, there has been a rapid increase in the publication of new methods for generating these sorts of beams [25–27]. This has been largely prompted by the availability of technology such as liquid-crystal spatial light modulators [28, 29] digital micro-mirror devices [30, 31], and q-plates [32], along with interest in polarisation effects reported in the non-paraxial regime (particularly effects which allow focussing below the conventional diffraction limit - see subsection 1.2.2). Passive methods for generating vector beams within the laser cavity have also been developed [33]. Structured light is now not only used to investigate fundamental physics [34, 35], but is applied in a wide variety of areas [36–39]. The impact is clearly evidenced when considering the Nobel prize awarded in 2014 for Stimulated Emission-Depletion (StED) Microscopy [40]. There are now various approaches to this technique, however, to put it simply a sample is illuminated by two beams - the first focusses light to a diffraction-limited spot, while the second beam is structured in a way that focusses to a doughnut-shaped intensity (known as the StED beam). This StED beam is used to photobleach fluorophores excited by the first beam, forcing them to their ground state. The result of this is that only the remaining excited fluorophores at the centre of the doughnut mode are able to fluoresce, revealing a significantly reduced spot size.

The polarisation property of light is most commonly controlled by introducing a phase difference between orthogonal polarisation components through differential optical path lengths, through the use of birefringent optical elements (such as quarter- and half-wave plates). Less commonly known however, a phase difference can also be achieved by a geometric phase effect [41]. Conversely, this allows modulation of the optical wavefront of a beam through control of its polarisation [42]. This can be implemented through a number of different ways [43–45], however, this thesis explicitly uses the spin-redirection geometric phase effect found when operating a Fresnel cone in a back-reflection mode [46]. This uses a phase-shift between s and p polarisation components upon total internal reflection at a boundary between glass and air. Unlike the common methods for introducing phase-shifts through differential optical path length (such as the use of birefringent material), this phase shift upon total internal reflection allows use with relatively broadband light (see subsection 3.3.1).

I first became familiar with the ability of a Fresnel cone to be used to structure the polarisation of light during my Masters project, prior to beginning my PhD research. Initially this work was intended as a short project driven entirely by curiosity, however, the practical and technological applications in areas such as laser machining, microscopy and polarimetry soon became clear and collaborative projects with industry partners began. Since then we have improved upon the generated polarisation states and developed high-efficiency coupling techniques ($\sim$ 100% efficiency as opposed to the previous $\sim$ 25%), one of which generates annular vector vortex beams. In chapter 2, I will give full details on the theory, formalisms and conventions used throughout my thesis, before describing the Fresnel cone high-efficiency coupling investigations in chapter 3.

1.2.2 Non-paraxial light and 3D polarisation

In 1959, Richards and Wolf reported a numerical method for calculating the resulting focal field in a high focussing-angle system, taking into account the full vector nature of light [47, 48]. It is only during the last few decades however that research has been taken up in this area, as in the past computational power was not sufficient to attempt these problems. It may be at first surprising that a beam with Gaussian intensity profile, that is strongly focussed by a circularly symmetric lens, does not necessarily have a circularly shaped focal spot. In a strong focussing regime, a longitudinal polarisation component emerges from the focussed radial polarisation component of the incident beam (as is discussed in chapter 4). If focussing linearly polarised light for example, the radial component is non-uniform in the azimuthal direction at the lens aperture, and the resulting focal spot is an elongated elliptical shape with an orientation depending on the linear polarisation orientation of the incident beam [49]. This is perhaps detrimental for certain applications, such as scanning microscopy (however, a circular focal spot is still easily achievable by focussing circularly polarised light[2]). For example, see Figure 1.1 where I show experimentally measured focal spots under strong focussing for certain polarisation input states, highlighting this polarisation dependence[3]. The knowledge that both size and shape of a focal volume depends on the incident polarisation has brought about a recent interest into both tight [50–52] and customised focal spots [53–56].

---

[2] Circular focal spot shapes are also possible from more complicated polarisation structures, as well as when focussing unpolarised light - as this is an ensemble of photons with random polarisations, resulting in an averaged focal spot with contributions from every polarisation state.

[3] I note here that the simulated focal spots are produced using the simulation described in chapter 4.

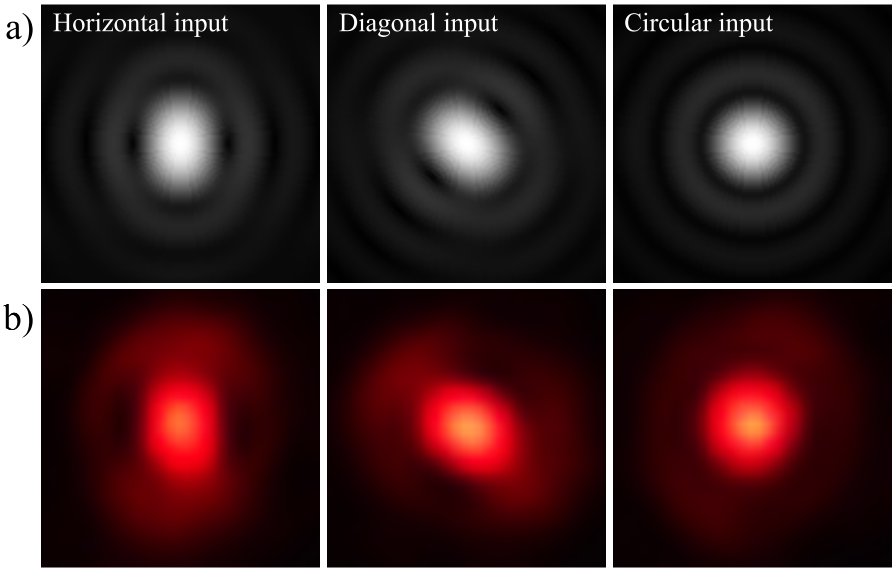

FIGURE 1.1: a) Simulated focal spots for certain input polarisation states with high NA focussing b) experimental measured focal spots.

In the early-2000s, the effects of high angle focussing of cylindrical vector beams became a topic of particular interest, where focal spots with a size below the conventional diffraction limit were reported possible [25]. More recently, a further reduction in size was reported by strongly focussing a beam with both spatially dependent polarisation and phase [57]. Given that lenses are ubiquitous in optical technology, applications for these tight focal volumes can be found not only in optical microscopy, but in a wide range of areas [58–61].

Following the report in 2016 of Fresnel cone vector vortex beams, we investigated the strong focussing properties of these beams by simulating the resulting focal spots using Richards and Wolf vector diffraction theory. In chapter 4, the details of the strong focussing investigation are given. We discovered through simulation that a Fresnel cone can be used to generate beams which allow sub-diffraction limited focal spots. Experimentally we found that the surface flatness and manufacturing quality of a Fresnel cone are crucial factors in the focussing ability of the resulting beams. Detrimental polarisation effects can also be found when using these beams in real microscope system, however, it is shown in this thesis that these effects can be pre-compensated for. This work is reported in the SPIE proceedings [62].

1.2.3 Polarimetry

In the previous sections, emphasis has been on the statement that there has been a rapid increase in reports of generation methods for light beams with structured polarisation, and how these beams can be useful. It is important however, not only to be able to generate useful polarisation states but also to have the ability to measure them.

Light can become at least partially polarised when it is reflected or transmitted through optically transparent media. The resulting polarisation state can depend on the surface geometry of the interacting object, or the birefringence and/or dichroic properties of the media transmitted through. This means that the polarisation property of light can contain information about its source, complimentary to the information usually gained from measuring wavelength and intensity. As already raised, polarisation is essentially invisible to conventional detectors, however, devices do exist which can reveal the polarisation state of incident light, known as polarimeters. These devices are found in a wide range of fields, including astronomy, remote observation, medical diagnosis and target detection, to name just some [63].

Numerous measurement domains exist for performing polarimetry on light, each with various benefits and drawbacks. The most common of these modulate the incident light in either a spatial, temporal or spectral manner - this will be discussed in more detail in chapter 5. A ‘rotating waveplate’ approach is preferred for commercial devices as it is fairly low-cost and compact, however, these devices rely on moving parts and contain birefringent components (limiting the use to specific wavelengths). In chapter 5 I will show that the same back-reflection technique for structuring light’s polarisation with a Fresnel cone given in chapter 3 can be used to reveal the incident polarisation state, in a single-shot polarimeter device. Unlike the rotating waveplate approach this technique contains no moving parts and allows broadband use. I will also give details about future work on developing a portable Fresnel cone polarimeter demonstrator, for use with high-power ultra-short pulse laser systems for characterisation.

Chapter 2

Background theory and conventions

2.1 Introduction

In this chapter I will provide the background theory from which the work shown in this thesis is derived, particularly with respect to the simulations developed, reasons for experimental decisions and the visual representations of polarised light I have used. In the real world, many light sources are both incoherent and unpolarised, such as sunlight, candlelight, or light from an incandescent bulb. Light in these cases is a random composition of different wavelengths, complex amplitudes, polarisation states and spatial distributions. In order to understand the characteristics and interactions of electromagnetic waves with optical components, I will initially consider the case of uniformly polarised coherent plane waves (sinusoidal waves that have a single wavelength and amplitude). As any wave can be decomposed into a sum of plane waves, the general theory can then be expanded to include other spatial distributions and compositions of light. The decomposition of a propagating wave as a sum of plane waves is an important concept and leads to the angular spectrum representation of optical fields, and will be important later in this chapter.

2.2 Complex vector light fields

Through this section I show how the vectorial electromagnetic wave nature of light emerges from Maxwell's equations with a few reasonable assumptions.

2.2.1 Revealing the wave equation

In the absence of any charges and assuming a vacuum, Maxwell's famous four equations become

$$\nabla \cdot \mathbf{E} = 0, \tag{2.1}$$

$$\nabla \cdot \mathbf{B} = 0, \tag{2.2}$$

$$\nabla \times \mathbf{E} = -\frac{\partial \mathbf{B}}{\partial t}, \tag{2.3}$$

$$\nabla \times \mathbf{B} = \epsilon_0 \mu_0 \frac{\partial \mathbf{E}}{\partial t}, \tag{2.4}$$

where $\mathbf{E}$ and $\mathbf{B}$ are the electric and magnetic fields respectively (in space and time, $\mathbf{E}(x, y, z, t)$ and $\mathbf{B}(x, y, z, t)$), ∇ is the nabla operator[1], ϵ_0 is the permitivitty of free space, μ_0 is the permeability of free space and t is time [6]. Upon taking the curl of both sides of Equation 2.3, we have

$$\nabla \times \nabla \times \mathbf{E} = -\frac{\partial(\nabla \times \mathbf{B})}{\partial t}. \tag{2.5}$$

We can use Equation 2.4 to eliminate $\mathbf{B}$ in Equation 2.5, obtaining

$$\nabla \times \nabla \times \mathbf{E} = -\epsilon_0 \mu_0 \frac{\partial}{\partial t}\left(\frac{\partial \mathbf{E}}{\partial t}\right). \tag{2.6}$$

Using the known vector identity

$$\nabla \times \nabla \times \mathbf{E} = \nabla(\nabla \cdot \mathbf{E}) - \nabla^2 \mathbf{E}, \tag{2.7}$$

and realising that in the absence of any free charges $\nabla \cdot \mathbf{E} = 0$ [6], we can simplify Equation 2.6 to

$$-\nabla^2 \mathbf{E} = -\epsilon_0 \mu_0 \frac{\partial^2 \mathbf{E}}{\partial t^2}. \tag{2.8}$$

---

[1] Where $\nabla \cdot \mathbf{E}$ is the divergence and $\nabla \times \mathbf{E}$ is the curl of the field in Cartesian coordinates.

Gathering the terms onto one side reveals the vector wave equation for the electric field $\mathbf{E}(\mathbf{r}, t)$ in free-space,

$$\nabla^2 \mathbf{E}(\mathbf{r}, t) - \epsilon_0 \mu_0 \frac{\partial^2 \mathbf{E}(\mathbf{r}, t)}{\partial t^2} = 0. \tag{2.9}$$

This is a three-dimensional vector equation containing three separate equations for the components of the electric field in Cartesian coordinate directions x, y and z. For each component there is a second derivative in space associated with a second derivative in time - this coupled-space and -time dependence is a hallmark of the general differential wave equation. Equation 2.9 written as

$$\nabla^2 \mathbf{E}(\mathbf{r}, t) - \frac{1}{c^2} \frac{\partial^2 \mathbf{E}(\mathbf{r}, t)}{\partial t^2} = 0, \tag{2.10}$$

implies the speed of the wave in free-space is $c = 1/\sqrt{\epsilon_0 \mu_0}$. An important solution to the vector wave equation is the plane wave solution,

$$\mathbf{E}(\mathbf{r}, t) = E_0 \ \mathrm{e}^{[i(\mathbf{k} \cdot \mathbf{r} - \omega t + \phi)]} \mathbf{e_r}, \tag{2.11}$$

where E_0 is the amplitude of the wave, ω is angular frequency, i is the imaginary number, ϕ is the phase offset at $t = 0$, $\mathbf{e_r}$ is a unit vector in the direction of oscillation, and $\mathbf{k}$ is the wavevector. The wavevector $\mathbf{k}$ has magnitude equal to the wavenumber $k = 2\pi/\lambda$ (λ being the monochromatic wavelength), and direction perpendicular to surfaces of constant phase ($\mathbf{k} \cdot \mathbf{r} - \omega t + \phi = \mathit{constant}$). Importantly, any linear superposition of solutions such as Equation 2.10 are also solutions to the wave equation. The common convention of exponential notation is used (specifically Euler's formula is made use of) as this can simplify algebra, however it is important to note that care must be taken to examine only the real part of this wave when considering the physical electric field.

Similar treatment can be given to the magnetic field, $\mathbf{B}$, and the concept of oscillating electromagnetic waves is established. These electromagnetic waves follow the restrictions given by Maxwell's equations, where it is particularly important to note that this restricts the electric and magnetic field to be oscillating transverse waves - both perpendicular to each other, as well as to the direction of propagation. In this thesis I will only consider the electric field, $\mathbf{E}$, and the magnetic field is largely disregarded from this point on (but could easily be established from the electric field through Maxwell's equations).

2.2.2 Polarisation

In the previous section I established that Maxwell's equations allow the propagation of electromagnetic plane waves in free space[2]. As shown in Equation 2.11, $\mathbf{e_r}$ describes the oscillation direction (or orientation) of the electric field, and it is this which is conventionally used to specify the polarisation of the light[3]. In the general case and given that a superposition of plane waves is also a solution to the vector wave equation, the electric field can be written

$$\mathbf{E}(z,t) = \frac{1}{\sqrt{2}}(E_{0x}\ \mathrm{e}^{[i(kz-\omega t+\phi_x)]}\mathbf{e}_x + E_{0y}\ \mathrm{e}^{[i(kz-\omega t+\phi_y)]}\mathbf{e}_y). \tag{2.12}$$

If the electric field vector orientation is constant, the wave is said to be linearly polarised. As an example, for an electromagnetic wave travelling in the positive z-direction and polarised in the x-direction, the electric field is written

$$\mathbf{E}(z,t) = E_{0x}\ \mathrm{e}^{[i(kz-\omega t+\phi)]}\mathbf{e}_x. \tag{2.13}$$

As a further example of a special case of linear polarisation, if $E_{0x} = E_{0y} = E_0$ and $\phi_x = \phi_y = \phi$, then

$$\mathbf{E}(z,t) = \frac{1}{\sqrt{2}}(E_0\ \mathrm{e}^{[i(kz-\omega t+\phi)]}\mathbf{e}_x + E_0\ \mathrm{e}^{[i(kz-\omega t+\phi)]}\mathbf{e}_y), \tag{2.14}$$

resulting in an electric field polarised in the $(\mathbf{e}_x + \mathbf{e}_y)$ direction at 45° to the x-axis (see Figure 2.1).

---

[2] Note that these are not the only solutions, for example, spherical and cylindrical waves are also possible.

[3] Conventionally the electric field of an electromagnetic wave is used to specify the polarisation direction as when light interacts with matter, the force exerted on electrons by the electric field is much greater in magnitude than that of the magnetic field [64].

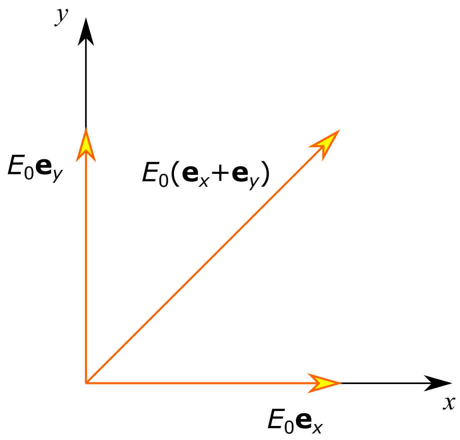

FIGURE 2.1: Vector addition of two linearly polarised waves in the x- and y-directions, resulting in a single linearly polarised wave at 45° to the x-axis.

In the above example, $E_{0x} = E_{0y} = E_0$, but if this is not the case then the result is simply linearly polarised light propagating in the $+z$-direction, but with a polarisation angle θ to the x-axis with $\theta = \tan^{-1}(E_{0y}/E_{0x})$. These linear combinations are simply vector additions of two linearly polarised waves with $\phi_x = \phi_y = \phi$.

Exploring this further, if $E_{0x} = E_{0y} = E_0$ but the phases are not equal, elliptical polarisation states are possible. Given a phase difference of $+\pi/2$ (and equal amplitudes) a special case is found. This is known as circular polarisation:

$$\mathbf{E}(z,t) = E_0\ \mathrm{e}^{[i(kz-\omega t+\phi)]}\mathbf{e}_x + E_0\ \mathrm{e}^{[i(kz-\omega t+\phi+\pi/2)]}\mathbf{e}_y. \tag{2.15}$$

The second term on the right can be expanded as

$$E_0\ \mathrm{e}^{[i(kz-\omega t+\phi+\pi/2)]}\mathbf{e}_y =\ \mathrm{e}^{(i\pi/2)}\ \mathrm{e}^{[i(kz-\omega t+\phi)]}. \tag{2.16}$$

Since $\mathrm{e}^{(i\pi/2)} = i$,

$$\mathrm{e}^{(i\pi/2)}\ \mathrm{e}^{[i(kz-\omega t+\phi)]} = i\ \mathrm{e}^{[i(kz-\omega t+\phi)]}, \tag{2.17}$$

and the resulting electric field can be written as

$$\mathbf{E}(z,t) = E_0\ \mathrm{e}^{[i(kz-\omega t+\phi)]}(\mathbf{e}_x + i\mathbf{e}_y). \tag{2.18}$$

For this wave the electric field vector rotates around the propagation axis with the tip tracing out a circle in the x-y plane, which is why it is known as circular polarisation. The handedness of the rotation depends on whether the $\pi/2$ phase shift is added or subtracted. I would like to note here that when superposing two electromagnetic waves, one right- and one left-circularly polarised with equal amplitudes, the result is a linearly polarised wave (with orientation dependent on the phase offset between the two circularly polarised waves) [6]. For example, the case just mentioned is

$$\begin{aligned}\left[E_0\ \mathrm{e}^{[i(kz-\omega t+\phi)]}(\mathbf{e}_x + i\mathbf{e}_y)\right] + \left[E_0\ \mathrm{e}^{[i(kz-\omega t+\phi)]}(\mathbf{e}_x - i\mathbf{e}_y)\right]& \\ = E_0\ \mathrm{e}^{[i(kz-\omega t+\phi)]}\mathbf{e}_x + E_0\ \mathrm{e}^{[i(kz-\omega t+\phi)]}i\mathbf{e}_y& \\ + E_0\ \mathrm{e}^{[i(kz-\omega t+\phi)]}\mathbf{e}_x - E_0\ \mathrm{e}^{[i(kz-\omega t+\phi)]}i\mathbf{e}_y& \\ = 2E_0\ \mathrm{e}^{[i(kz-\omega t+\phi)]}\mathbf{e}_x,& \qquad (2.19)\end{aligned}$$

which is horizontally linearly polarised light with amplitude twice that of the individual circularly components.

What I have described in this section is just a set of specific special cases, and given a linear combination of two monochromatic waves with $E_{0x} \neq E_{0y}$ and $\phi_x \neq \phi_y$ a whole range of elliptical polarisation states are possible. In all cases however, the electric and magnetic fields are always perpendicular to each other and to the direction of propagation.

2.3 Polarisation formalisms and conventions

In the previous section I have discussed the orientation of the electric field vector of the light to represent the polarisation state. When viewed looking towards the light source the tip of the electric field vector traces out the shape of an ellipse as it oscillates, where circles and lines are special cases (representing circularly and linearly polarised light). I note here that these oscillations are far too fast to be experimentally measured by conventional detectors and any polarisation measurement is an average in time of many oscillations. In this section I will detail useful mathematical descriptions for polarised light. The most well known formalisms for dealing with polarisation interactions with optical elements include Jones calculus [65], Mueller calculus [66] and coherency matrices [67]. In my research I have made use of the Jones formalism as it is especially concise (when using the normalised form), and the Mueller formalism as it involves experimentally measurable observables (intensities), so I explain these two descriptions in this section.

2.3.1 Jones formalism

In the paraxial regime[4] where only small angles are made with respect to the optical axis, polarisation is considered to be purely transverse to the direction of propagation. This means that any polarisation state can be decomposed into two orthogonal components, where in a Cartesian coordinate system this is usually an x- and y-components. Established by Robert Clark Jones in 1941 [65], Jones calculus shows that light's polarisation can be represented by a Jones vector, which is a 2×1 vector consisting of the complex amplitudes of the orthogonal x and y electric field components. Optical elements which act on a Jones vector are represented by 2×2 Jones matrices. These are transformation matrices that reveal the resulting output Jones vector when taking the product of the Jones matrix with the incident Jones vector. As mentioned, this representation is often preferred as it is very concise, however, it should be noted that it can only deal with fully polarised states (for partially or unpolarised light see subsection 2.3.2). Propagating in the $+z$-direction, the electric field, $\mathbf{E}$ can be written as

$$\mathbf{E}(z,t) = E_{0x}\ \mathrm{e}^{[i(kz-\omega t+\phi_x)]}\mathbf{e}_x + E_{0y}\ \mathrm{e}^{[i(kz-\omega t+\phi_y)]}\mathbf{e}_y. \tag{2.20}$$

The polarisation is not time dependent so time can be neglected, and we consider the instantaneous case at $z = 0$. This can be written in vector form as a Jones vector

$$\mathbf{J} = \begin{bmatrix} E_x(0,0) \\ E_y(0,0) \end{bmatrix} = \begin{bmatrix} E_{0x}\exp(i\phi_x) \\ E_{0y}\exp(i\phi_y) \end{bmatrix}, \tag{2.21}$$

where E_{0x} and E_{0y} are amplitudes, ϕ_x and ϕ_y are phases. It is just the difference in phase which is important[5], so we can arbitrarily set ϕ_x to 0. The intensity I can be calculated using

$$I = \begin{bmatrix} {E_x}^* {E_y}^* \end{bmatrix} \begin{bmatrix} E_x \\ E_y \end{bmatrix} = E_x{E_x}^* + E_y{E_y}^* = |E_x|^2 + |E_y|^2. \tag{2.22}$$

---

[4] Here, the paraxial regime refers to situations where the paraxial approximation is assumed. This is a small-angle approximation requiring that rays only make small angles to an optical axis (an imaginary line defining the direction in which light propagates in a system), such that $\sin\theta \approx \theta$, $\cos\theta = 1$ and $\tan\theta \approx \theta$.

[5] Unless nonlinear processes, e.g. the interference between multiple light beams, are considered.

By normalising I to 1, the Jones vector representation for a horizontal ($\mathbf{J}_{\mathrm{H}}$) and vertical ($\mathbf{J}_{\mathrm{V}}$) polarisation states for example is then

$$\mathbf{J}_{\mathrm{H}} = \begin{bmatrix} E_{0x} \exp\left(i\phi_x\right) \\ 0 \end{bmatrix} = \begin{bmatrix} 1 \\ 0 \end{bmatrix} \tag{2.23}$$

and

$$\mathbf{J}_{\mathrm{V}} = \begin{bmatrix} 0 \\ E_{0y} \exp\left(i\phi_y\right) \end{bmatrix} = \begin{bmatrix} 0 \\ 1 \end{bmatrix}. \tag{2.24}$$

If $E_{0x} = E_{0y}$ and $\phi_x = \phi_y$ in Equation 2.21, then

$$\mathbf{J} = \begin{bmatrix} E_{0x} \exp\left(i\phi_x\right) \\ E_{0x} \exp\left(i\phi_x\right) \end{bmatrix}. \tag{2.25}$$

This Jones vector is normalised by dividing both components by $\sqrt{2}E_{0x}\ \mathrm{e}^{(i\phi_x)}$ to get

$$\mathbf{J}_{\mathrm{D}} = \frac{1}{\sqrt{2}} \begin{bmatrix} 1 \\ 1 \end{bmatrix}, \tag{2.26}$$

which is the Jones vector for diagonally polarised light (45° to the x-axis). Similarly anti-diagonal light is represented by

$$\mathbf{J}_{\mathrm{A}} = \frac{1}{\sqrt{2}} \begin{bmatrix} 1 \\ -1 \end{bmatrix}. \tag{2.27}$$

Finally considering the case for circularly polarised light, where $E_{0x} = E_{0y}$ and $\phi_x = \phi_y + \pi/2$, as shown in [6] we get

$$\mathbf{J} = \begin{bmatrix} E_{0x}\ \mathrm{e}^{(i\phi_x)} \\ E_{0x}\ \mathrm{e}^{i(\phi_x + \pi/2)} \end{bmatrix}, \tag{2.28}$$

where upon dividing both elements by $\sqrt{2}E_{0x}\ \mathrm{e}^{(i\phi_x)}$ becomes

$$\mathbf{J}_{\mathrm{R}} = \frac{1}{\sqrt{2}} \begin{bmatrix} 1 \\ \mathrm{e}^{(i\pi/2)} \end{bmatrix} = \frac{1}{\sqrt{2}} \begin{bmatrix} 1 \\ i \end{bmatrix}. \tag{2.29}$$

This is the normalised Jones vector for right-handed circular polarisation. Similarly it can be found that

$$\mathbf{J}_{\mathrm{L}} = \frac{1}{\sqrt{2}} \begin{bmatrix} 1 \\ -i \end{bmatrix} \tag{2.30}$$

for left-handed circular polarisation. I note here that the sign of the second element in the circular polarisation state only depends on the frame of reference defined - i.e. these could be oppositely signed if considering the case looking away from the light's source rather than towards it (a simple but important distinction to make clear when defining one's polarisation basis).

Two complex vectors are orthogonal if $\mathbf{X} \cdot \mathbf{Y}^\star = 0$, and it can be shown that

$$\mathbf{H} \cdot \mathbf{V}^\star = \mathbf{A} \cdot \mathbf{D}^\star = \mathbf{R} \cdot \mathbf{L}^\star = 0. \tag{2.31}$$

Hence, horizontal/vertical, diagonal/anti-diagonal and right-/left-circular polarisation are orthogonal sets which are mutually unbiased and form six basis states used throughout this thesis - see Figure 2.2 for a diagram depicting these defined states.

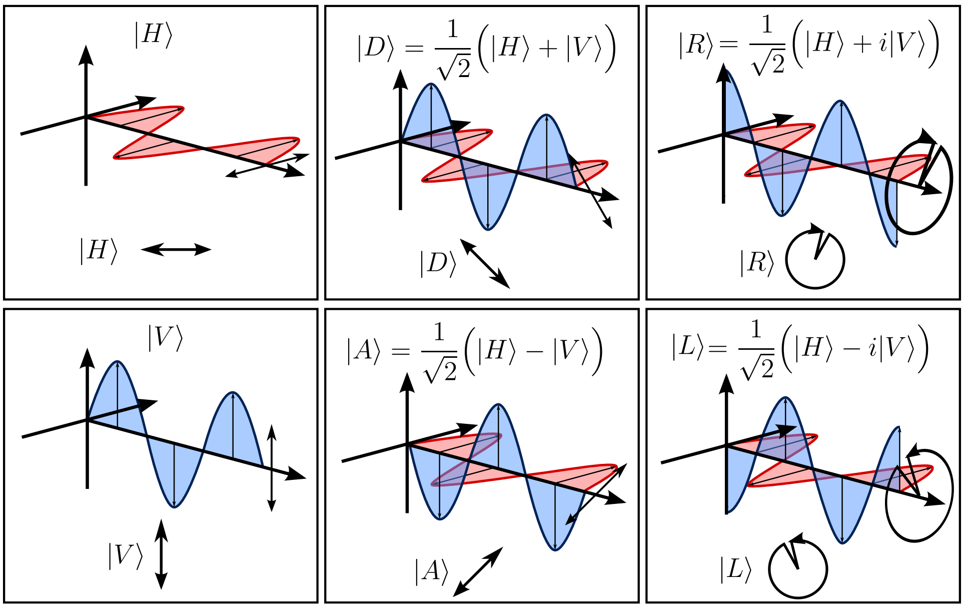

FIGURE 2.2: Diagram showing the six polarisation basis states and conventions used throughout this thesis.

By using Jones vectors and the Jones calculus approach, optical components such as simple mirrors and polarising filters can be represented by 2×2 Jones matrices (which are commonly known) to represent the action of these components, and the output state of a given system ($\mathbf{J}_{\text{out}}$) can be calculated for a known input state ($\mathbf{J}_{\text{in}}$) as

$$\mathbf{J}_{\text{out}} = \mathbf{N} \cdot \mathbf{J}_{\text{in}}. \tag{2.32}$$

When a system contains multiple components, $\mathbf{N}$ is the product of the matrices of the separate components such as $\mathbf{N} = \mathbf{N}_3 \cdot \mathbf{N}_2 \cdot \mathbf{N}_1$ (the order of multiplication is important, $\mathbf{N}_1$ should act on the input Jones vector first).

2.3.2 Stokes and Mueller formalisms

Although a Jones vector can be used to completely specify the polarisation state of light, it is limited to fully polarised states. In reality, whether in nature or experiment this is hardly ever the case as many objects either partially polarise light or cause depolarisation, resulting in partially or unpolarised light. Importantly, the phases contained in a Jones vector are not experimentally accessible.

Fortunately, a polarisation state can also be represented using a Stokes vector $\mathbf{S}$, which is a four-element vector containing parameters that are related to measurable intensities [66], written as

$$\mathbf{S} = \begin{bmatrix} S_0 & S_1 & S_2 & S_3 \end{bmatrix}^T . \tag{2.33}$$

These four parameters (S_0, S_1, S_2 and S_3) are related to intensities of the light when it is projected into six polarisation basis states (namely horizontal $\langle |E_x|^2 \rangle$, vertical $\langle |E_v|^2 \rangle$, diagonal $\langle |E_d|^2 \rangle$, anti-diagonal $\langle |E_a|^2 \rangle$, right-circular $\langle |E_r|^2 \rangle$ and left-circular $\langle |E_l|^2 \rangle$ polarisations, where $\langle ... \rangle$ signifies a time average) as follows:

$$\begin{aligned}
S_0 &= \langle |E_x|^2 \rangle + \langle |E_y|^2 \rangle = \langle |E_d|^2 \rangle + \langle |E_a|^2 \rangle = \langle |E_r|^2 \rangle + \langle |E_l|^2 \rangle, \\
S_1 &= \langle |E_x|^2 \rangle - \langle |E_y|^2 \rangle, \\
S_2 &= \langle |E_d|^2 \rangle - \langle |E_a|^2 \rangle, \\
S_3 &= \langle |E_r|^2 \rangle - \langle |E_l|^2 \rangle.
\end{aligned}$$

As before, the total intensity I is conventionally normalised to 1, giving the states shown in the table below.

Basis state	**Stokes vector**
$\lvert H\rangle$	$\begin{bmatrix} 1 & 1 & 0 & 0 \end{bmatrix}^T$
$\lvert V\rangle$	$\begin{bmatrix} 1 & -1 & 0 & 0 \end{bmatrix}^T$
$\lvert D\rangle$	$\begin{bmatrix} 1 & 0 & 1 & 0 \end{bmatrix}^T$
$\lvert A\rangle$	$\begin{bmatrix} 1 & 0 & -1 & 0 \end{bmatrix}^T$
$\lvert R\rangle$	$\begin{bmatrix} 1 & 0 & 0 & i \end{bmatrix}^T$
$\lvert L\rangle$	$\begin{bmatrix} 1 & 0 & 0 & -i \end{bmatrix}^T$

By using Stokes vectors and a Mueller calculus approach [68], the action of optical components is represented by 4×4 Mueller matrices (which are again commonly known), and the output polarisation state of a given system can be calculated for a known input using

$$\mathbf{S}_{\text{out}} = \mathbf{M}\,\mathbf{S}_{\text{in}}, \tag{2.34}$$

where $\mathbf{S}_{\text{in}}$ and $\mathbf{S}_{\text{out}}$ are the initial and final polarisation states and $\mathbf{M}$ is the Mueller matrix representing the optical system. When a system contains multiple components, $\mathbf{M}$ is the product of the matrices of the separate components such as $\mathbf{M} = \mathbf{M}_3{\cdot}\mathbf{M}_2{\cdot}\mathbf{M}_1$ (the order of multiplication is important, $\mathbf{M}_1$ should act on the input Stokes vector first). Stokes vectors are also applicable to polarisation states that are not fully polarised.

As detectors are only sensitive to intensity and not the phase or orientation of the electric field, the Stokes formalism is ideal for application in polarimetry.

2.3.3 Jones-to-Stokes conversions

It has often been useful for me to be able to convert from a Jones vector to a Stokes vector. The method to carry this out will be described here. Given the Jones vector shown in Equation 2.21, and the Stokes parameters

$$\begin{aligned}
S_0 &= |E_h|^2 + |E_v|^2 \\
S_1 &= |E_h|^2 - |E_v|^2 \\
S_2 &= |E_d|^2 - |E_a|^2 \\
S_3 &= |E_r|^2 - |E_l|^2 ,
\end{aligned} \tag{2.35}$$

where the subscripts h, v, d, a, r and l are used to signify the horizontal, vertical, diagonal, anti-diagonal, right-circular and left-circular polarisation components, and

$$\begin{aligned} E_d &= \frac{1}{\sqrt{2}}(E_h + E_v) \\ E_a &= \frac{1}{\sqrt{2}}(E_h - E_v) \\ E_r &= \frac{1}{\sqrt{2}}(E_h + iE_v) \\ E_l &= \frac{1}{\sqrt{2}}(E_h - iE_v), \end{aligned} \tag{2.36}$$

the Stokes parameters in terms of the $E_{h,v}$ components are thus

$$\begin{aligned} S_0 &= E_h E_h^* + E_v E_v^* \\ S_1 &= E_h E_h^* - E_v E_v^* \\ S_2 &= E_h^* E_v + E_h E_v^* \\ S_3 &= -i(E_h^* E_v - E_h E_v^*). \end{aligned} \tag{2.37}$$

Following this, the individual amplitudes and phases are found to be

$$\begin{aligned} E_{0x} &= \sqrt{E_h E_h^*} = \sqrt{\frac{S_0 + S_1}{2}} \\ E_{0y} &= \sqrt{E_v E_v^*} = \sqrt{\frac{S_0 - S_1}{2}} \\ \phi_h - \phi_v &= \arctan\frac{S_3}{S_2} \\ \phi_v &= -\arctan\frac{S_3}{S_2} \quad \text{when} \quad \phi_h = 0. \end{aligned} \tag{2.38}$$

Throughout my research it has also been necessary to convert from a Jones matrix to a Mueller matrix. Here I will show how to convert from a 2 × 2 Jones matrix to a 4 × 4 Mueller matrix following the method described by Azzam [64]. As I have previously explained, a Jones vector describes the complex x- and y-components of the electric field, while a Stokes vector describes intensities of light according to different polarisation states. The conversion method is thus derived by calculating light intensities from electric fields. In order to do this a mathematical operation known as the Kronecker product is needed, which constructs a 4 × 4 matrix when applied to 2×2 Jones matrices. For example, if $\mathbf{A}$ and $\mathbf{B}$ are two Jones matrices

$$\mathbf{A} = \begin{bmatrix} a_{11} & a_{12} \\ a_{21} & a_{22} \end{bmatrix} \tag{2.39}$$

and

$$\mathbf{B} = \begin{bmatrix} b_{11} & b_{12} \\ b_{21} & b_{22} \end{bmatrix}, \tag{2.40}$$

then

$$\mathbf{A} \otimes \mathbf{B} = \begin{bmatrix} a_{11}\mathbf{B} & a_{12}\mathbf{B} \\ a_{21}\mathbf{B} & a_{22}\mathbf{B} \end{bmatrix} = \begin{bmatrix} a_{11}b_{11} & a_{11}b_{12} & a_{12}b_{11} & a_{12}b_{12} \\ a_{11}b_{21} & a_{11}b_{22} & a_{12}b_{21} & a_{12}b_{22} \\ a_{21}b_{11} & a_{21}b_{12} & a_{22}b_{11} & a_{22}b_{12} \\ a_{21}b_{21} & a_{21}b_{22} & a_{22}b_{21} & a_{22}b_{22} \end{bmatrix}. \tag{2.41}$$

With knowledge of how to apply the Kronecker product to two matrices, the next step in the conversion considers a Jones matrix $\mathbf{N}$ acting on an input Jones vector $\mathbf{J}_{in}$ as

$$\begin{bmatrix} J_x \\ J_y \end{bmatrix}_{\text{out}} = \begin{bmatrix} N_{11} & N_{12} \\ N_{21} & N_{22} \end{bmatrix} \begin{bmatrix} J_x \\ J_y \end{bmatrix}_{\text{in}}. \tag{2.42}$$

By taking the Kronecker product of Equation 2.42 with its complex conjugate we can express the Jones vectors in terms of intensities:

$$\mathbf{J}_{\text{out}} \otimes \mathbf{J}^*_{\text{out}} = (\mathbf{N} \otimes \mathbf{N}^*)(\mathbf{J}_{\text{in}} \otimes \mathbf{J}^*_{\text{in}}). \tag{2.43}$$

The Kronecker product of $\mathbf{J} \otimes \mathbf{J}^*$ results in a 4×1 coherency vector $\mathbf{C}$ as

$$\mathbf{C} = \begin{bmatrix} J_x \\ J_y \end{bmatrix} \otimes \begin{bmatrix} J^*_x \\ J^*_y \end{bmatrix} = \begin{bmatrix} J_x J^*_x \\ J_x J^*_y \\ J_y J^*_x \\ J_y J^*_y \end{bmatrix}. \tag{2.44}$$

Thus,

$$\mathbf{C}_{\text{out}} = (\mathbf{N} \otimes \mathbf{N}^*)\mathbf{C}_{\text{in}}. \tag{2.45}$$

Using the coherency vector, a Stokes vector $\mathbf{S}$ can be expressed as

$$\mathbf{S} = \mathbf{X}\mathbf{C}, \tag{2.46}$$

where

$$\mathbf{X} = \begin{bmatrix} 1 & 0 & 0 & 1 \\ 1 & 0 & 0 & -1 \\ 0 & 1 & 1 & 0 \\ 0 & i & -i & 0 \end{bmatrix}. \tag{2.47}$$

Multiplying out Equation 2.46 we get

$$\begin{bmatrix} S_0 \\ S_1 \\ S_2 \\ S_3 \end{bmatrix} = \begin{bmatrix} J_x J_x^* + J_y J_y^* \\ J_x J_x^* - J_y J_y^* \\ J_x J_y^* + J_y J_x^* \\ i(J_x J_y^* - J_y J_x^*) \end{bmatrix}, \tag{2.48}$$

which agrees with Equation 2.37 for the definition of the Stokes vector. Additionally, Equation 2.46 can be rearranged for both the input and output cases as $\mathbf{C}_{\text{in}} = \mathbf{X}^{-1}\mathbf{S}_{\text{in}}$ and $\mathbf{C}_{\text{out}} = \mathbf{X}^{-1}\mathbf{S}_{\text{out}}$, which, by inserting into Equation 2.45 it can be shown that

$$\mathbf{S}_{\text{out}} = \mathbf{X}(\mathbf{J} \otimes \mathbf{J}^*)\mathbf{X}^{-1}\mathbf{S}_{\text{in}}. \tag{2.49}$$

Here, $\mathbf{X}(\mathbf{J} \otimes \mathbf{J}^*)\mathbf{X}^{-1}$ represents a Mueller matrix $\mathbf{M}$ in terms of Jones matrices (acting on an input Stokes vector as described in subsection 2.3.2), allowing conversion from Jones-to-Mueller. It is important to note here that when performing this conversion it must be assumed that the system represented by the Jones matrix does not depolarise the light, even though the resulting Mueller matrix can describe depolarisation.

2.3.4 Measuring the Mueller matrix of a system

As described in previous sections there are various methods for analysing polarisation, using either Jones matrices [65], Mueller calculus [66] or coherency matrices [67]. For experimental determination of the polarisation properties of a system, Mueller matrices are the most straightforward to work with as these rely on experimental intensity measurements. Here a system could be a single optical component, transmission through an optically transparent sample, reflection from a surface, or a series of a combination of any number of these. For example, in chapter 4 I show that I determine a single Mueller matrix for an entire microscope system, consisting of multiple mirror reflections and transmissions through dichroic beam-splitters. I will now describe the method I used for experimentally determining the Mueller matrix, closely following that laid out in [69]. Matrix normalisation is discussed in chapter 5, while this section deals only with the experimental measurement and subsequent determination of the Mueller matrix.

Firstly some assumptions must be made clear - as the elements of a Mueller matrix can depend on wavelength and angle of incidence on the component being measured, these are assumed to be fixed. The general setup used for measuring the Mueller matrix is shown in Figure 2.3.

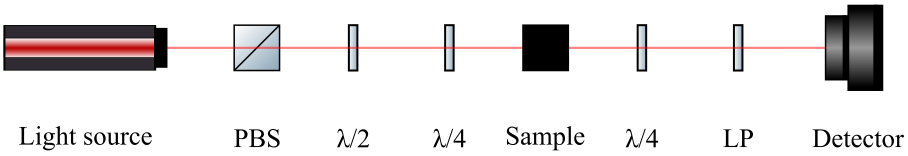

FIGURE 2.3: Diagram showing typical setup used to measure a Mueller matrix. PBS is a polarising beam-splitter, $\lambda/2$ and $\lambda/4$ are half- and quarter-wave plates respectively, and LP is a linear polariser.

In Figure 2.3, PBS is a polarising beam-splitter, $\lambda/2$ and $\lambda/4$ are half- and quarter-wave plates respectively, and LP is a linear polariser. The light source can be either a laser, where care must be taken to ensure the waveplates are of the correct wavelength specification, or alternatively a white light source can be used to investigate the Mueller matrix across the visible spectrum. If using a white light source however, Fresnel rhombs should be used in place of waveplates as they allow achromatic operation (See subsection 2.4.3). The detector used can be any detector capable of providing a quantitative intensity measurement. The PBS is used to ensure a clean polarisation input state[6]. The waveplates prior to the sample are used to generate the required input polarisation states, while the waveplate and linear polariser after the sample are used to analyse the polarisation state.

In general, a total of 36 measurements $q = 0, 1, 2...35$ are made in order to determine all 16 elements of a Mueller matrix $\mathbf{M}$ (using the 6 polarisation basis state settings for both the polarisation state generator and analyser) . As there are technically only 16 unknown values in a 4×4 Mueller matrix, full matrix determination could be made with 16 measurements if the required generator and analyser settings are known. Using a half- and quarter-wave plate, polarisation states are generated with Stokes vectors $\mathbf{G}_q$. Following the Stokes and Mueller formalism described

---

[6] A spirit level can be used to ensure the PBS is aligned with the optical table.

in subsection 2.3.2, the resulting polarisation state after the sample is $\mathbf{MG}_q$. These resulting states are then analysed using a quarter-wave plate and linear polariser, which have an analyser Stokes vector $\mathbf{A}_q$. The intensity on the detector is then $I_q = \mathbf{A}_q^T\mathbf{MG}_q$. From a set of intensity measurements, a system of linear equations can be solved for certain Mueller matrix elements. For example, if setting the generated state to be horizontally linearly polarised (H) and the analyser state to analyse horizontally (H), we get

$$\begin{aligned} I = \mathbf{A}_H^T\mathbf{MG}_H &= \frac{1}{2}\begin{bmatrix} 1 & 1 & 0 & 0 \end{bmatrix}\begin{bmatrix} m_{00} & m_{01} & m_{02} & m_{03} \\ m_{10} & m_{11} & m_{12} & m_{13} \\ m_{20} & m_{21} & m_{22} & m_{23} \\ m_{30} & m_{31} & m_{32} & m_{33} \end{bmatrix}\frac{1}{2}\begin{bmatrix} 1 \\ 1 \\ 0 \\ 0 \end{bmatrix} \\ &= \frac{m_{00}+m_{01}+m_{10}+m_{11}}{4}. \end{aligned}$$

It can be seen that the intensity observed on the detector with the generated and analyser states both set to horizontal, depends on the Mueller matrix elements m_{00}, m_{01}, m_{10}, and m_{11} of $\mathbf{M}$. Carrying out this process with both horizontally and vertically aligned generator and analyser settings in the four combinations H/H, H/V, V/H and V/V (for generator/analyser) yields intensities

$$I_0 = \frac{m_{00}+m_{01}+m_{10}+m_{11}}{4}, \tag{2.50}$$

$$I_1 = \frac{m_{00}-m_{01}+m_{10}-m_{11}}{4}, \tag{2.51}$$

$$I_2 = \frac{m_{00}+m_{01}-m_{10}-m_{11}}{4}, \tag{2.52}$$

and

$$I_3 = \frac{m_{00}-m_{01}-m_{10}+m_{11}}{4}. \tag{2.53}$$

These four equations form a set of linear equations which can be used to solve for the four matrix elements as

$$\begin{bmatrix} m_{00} \\ m_{01} \\ m_{10} \\ m_{11} \end{bmatrix} = \begin{bmatrix} I_0+I_1+I_2+I_3 \\ I_0+I_1-I_2-I_3 \\ I_0-I_1+I_2-I_3 \\ I_0-I_1-I_2+I_3 \end{bmatrix} \tag{2.54}$$

This process is repeated using generator and analyser settings including diagonal and anti-diagonal linear polarisation (D and A) and right- and left-circular polarisation (R and L) for a total of 36 intensity measurements, to obtain intensities for determining the remaining Mueller matrix elements. For completeness, the following table shows the intensity calculations with generator/analyser settings required for the remaining Mueller matrix elements.

Mueller element	**Intensity equation**
m_{00}	$I_{HH} + I_{VH} + I_{HV} + I_{VV}$
m_{01}	$I_{HH} - I_{VH} + I_{HV} - I_{VV}$
m_{10}	$I_{HH} + I_{VH} - I_{HV} - I_{VV}$
m_{11}	$I_{HH} - I_{VH} - I_{HV} + I_{VV}$
m_{02}	$I_{AA} - I_{DA} + I_{AD} - I_{DD}$
m_{20}	$I_{AA} + I_{DA} - I_{AD} - I_{DD}$
m_{22}	$I_{AA} - I_{DA} - I_{AD} + I_{DD}$
m_{03}	$I_{RR} - I_{LR} + I_{RL} - I_{LL}$
m_{30}	$I_{RR} + I_{LR} - I_{RL} - I_{LL}$
m_{33}	$I_{RR} - I_{LR} - I_{RL} + I_{LL}$
m_{12}	$I_{AH} - I_{AV} - I_{DH} + I_{DV}$
m_{21}	$I_{HA} - I_{VA} - I_{HD} + I_{VD}$
m_{13}	$I_{RH} - I_{RV} - I_{LH} + I_{LV}$
m_{31}	$I_{HR} - I_{VR} - I_{HL} + I_{VL}$
m_{23}	$I_{RA} - I_{LA} - I_{RD} + I_{LD}$
m_{32}	$I_{AR} - I_{DR} - I_{AL} + I_{DL}$

It is worth noting that from the 36 measurements taken there are multiple combinations to determine the element m_{00}, which could be used as a simple check. Over-complete determination can also help to analyse and reduce errors, as is done for the Fresnel cone polarimeter work described in chapter 5.

2.3.5 Polarisation ellipse and the Poincaré sphere

As well as understanding the various useful mathematical methods for describing polarised light, visual representations can also be useful as they often facilitate an intuitive interpretation. In this section I will detail the polarisation ellipse and the Poincaré sphere.

The polarisation of light is described as being elliptical, as when looking towards the source of a light beam the electric field vector $\mathbf{E}$ traces out the shape of an ellipse in the x-y plane. Linear and circular are simply special cases of elliptical polarisation. From [70], the Stokes parameters are related to the eccentricity e (ratio of semi-minor axis to semi-major axis), orientation θ and chirality (sign of S_3) of a polarisation ellipse through

$$S_1 = \frac{e^2 \cos(2\theta)}{2 - e^2} \tag{2.55}$$

$$S_2 = \frac{e^2 \sin(2\theta)}{2 - e^2} \tag{2.56}$$

$$S_3^2 = \frac{4(1 - e^2)}{2(2 - e^2)} \tag{2.57}$$

Derivation is found in the appendix of [70]. These can be rearranged to find

$$e^2 = \frac{2\sqrt{S_1^2 + S_2^2}}{1 + \sqrt{S_1^2 + S_2^2}} \tag{2.58}$$

$$\tan(2\theta) = \frac{S_1}{S_2} \tag{2.59}$$

The handedness, denoted by the sign of S_3 can be incorporated into the eccentricity to give $-1 \leq e \leq 1$ (-1 and 1 represent left- and right-circularly polarised light, while 0 represents linear). The angle θ is measured clockwise from the negative x-axis. Figure 2.4 shows the plotted ellipses and colour scheme used throughout this thesis to visually represent polarisation. Note that when these ellipses are plotted for experimental data, a resolution of 21 × 21 superpixels will be used which encompasses an average Stokes vector for the superpixel.

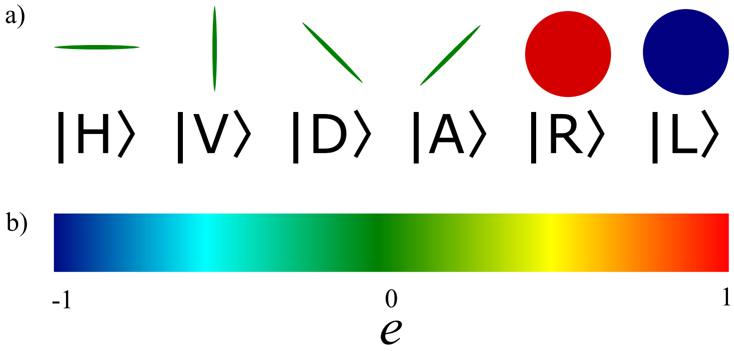

FIGURE 2.4: a) Polarisation ellipses plotted from theoretical Stokes vectors for the six basis states. b) The colour scheme used to depict all ellipticities.

Polarisation states can also be visually represented as points on a Poincaré sphere, shown below in Figure 2.5 in Cartesian coordinates. This is a sphere of unit radius, so that fully polarised states which have $\sqrt{S_1^2 + S_2^2 + S_3^2} = 1$ lie on the surface of the sphere, while partially polarised states lie within the sphere. In this depiction, conventionally right- and left-circular polarisation are positioned at the poles, all linear states lie on the equator of the Poincaré sphere and antipodal points are orthogonal states.

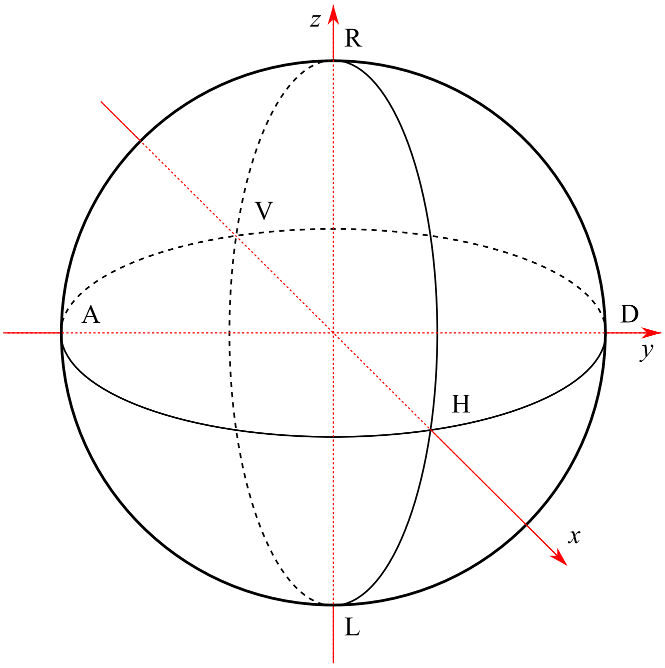

FIGURE 2.5: Diagram showing the Poincaré sphere.

2.3.6 Polarimetry conventions

Optical polarimetry is employed in a wide range of fields, and while the same mathematics and Stokes formalism is used in each case, different terms and naming conventions can be found - I will briefly discuss these here.

In the previous sub-section I elected to use throughout this thesis $[S_0, S_1, S_2, S_3]^T$ to denote the Stokes parameters, which is also the convention often used in the fields of target detection and remote sensing. This designation is convenient when considering element-indexing while working with linear algebra and matrices, however, care must be taken when using this convention as occasionally $[S_1, S_2, S_3, S_4]^T$ is used instead by some authors. Additionally, S_i is sometimes used to denote signal measurements. The second most common naming convention for the Stokes parameters is the use of $[I, Q, U, V]^T$ for historical reasons in the field of astronomy, as these were used by Chandrasekhar in 1947 [71] when re-introducing the work of Stokes from 1852.

In addition to the various naming conventions for the Stokes parameters, it is important to be clear on the coordinate system being used. For example, defining the polarisation basis states using a right- or left-handed coordinate system may affect the sign of S_1, S_2, or the handedness of the circular component, S_3. Similarly, it is important to state for the definition of the handedness of S_3 whether the observer is looking towards the light source (often used in astronomy) or away from the light source (often used in particle and quantum physics). Here I restate that throughout my thesis I choose to use the convention of looking towards the light source (motivated by use of a camera to record data), as well as using a right-handed coordinate system.

2.4 Polarisation and interactions with optical elements

In this section I will describe the effects on the polarisation of light as it interacts with different optical components. The optical elements I will discuss will primarily be those used in an optics laboratory as these are most relevant for this thesis, such as the use of linear polarisers, transmission through birefringent material and reflections at glass-air boundaries.

2.4.1 Dichroism

When beginning work with polarisation in an optics laboratory, the first component one usually encounters is a linear polariser. These rely on (linear) dichroism (sometimes referred to as diattenuation), which is the property of a material to selectively absorb one polarisation state while transmitting the orthogonal state[7].

---

[7] Most commonly the polariser will be a linear polariser, however, circular polarisers do exist where the phenomenon is known as circular dichroism.

A wire-grid polariser consists of a set of parallel conducting wires. When an electromagnetic wave is incident on this wire-grid, it can be decomposed into two orthogonal fields - one parallel and one perpendicular to the wire-grid orientation. The component of the electric field aligned with the wire-grid interacts with electrons in the conducting wires and causes a current to flow, transferring energy. The electrons are not able to move much in the perpendicular direction and the component of the wave in this direction is almost fully transmitted [6]. This is perhaps contrary to intuition where it is often thought that the electric field component parallel to the wire-grid spaces is that allowed to pass - this is not the case (as depicted in Figure 2.6.

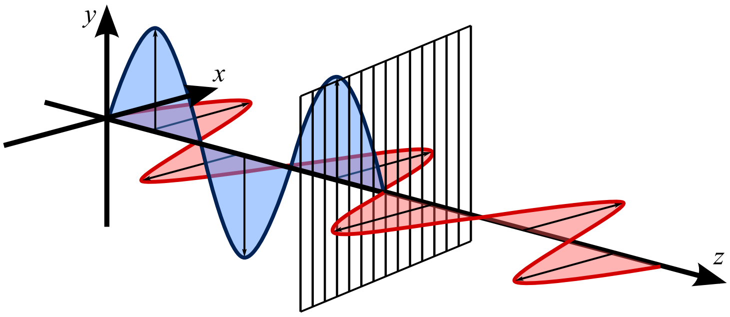

FIGURE 2.6: Figure showing the transmission of the electric field component orthogonal to the orientation of parallel wires in a wire-grid polariser. Here the blue (red) field component is parallel (perpendicular) to the wire-grid orientation.

Today most linear polarisers are instead based on a polaroid sheet. These consist of a polyvinyl alcohol sheet which is stretched causing hydrocarbon molecules to configure into long chains, which are analogous and function similarly to the wire-grid polariser [6]. When selecting a linear polariser, it is important to note the operational wavelength range and the transmission:extinction ratio. Crystal based polarisers also exist which can provide a high extinction ratio, though these rely on birefringence.

2.4.2 Birefringence

The common method for inducing a differential phase-shift between orthogonal polarisation components is through birefringence. This phenomenon is present in optically anisotropic crystals which have two separately defined refractive indices for orthogonal polarisation components[8]. The result of this is that the two polarisation components propagate through the crystal at different phase velocities, inducing a phase shift between them. By manufacturing a plate of this material with specific thickness, one obtains an optical component for modulating light's polarisation state in a controlled way without diverting or attenuating the beam[9]. These are known as waveplates and are most commonly manufactured to induce a quarter- or half-wavelength phase shift (quarter- or half-wave plate respectively). It is important to note that these components operate accurately only for a specific wavelength.

When selecting a waveplate to use there is often the option of zero-order and multi-order features. Multi-order waveplates are manufactured to have an integer multiple of the required phase-shift, for example a thickness of $50\lambda/2$ for a half-wave plate. Zero-order plates achieve the exact required phase-shift by combining two multi-order plates oppositely orientated so that the resulting phase-shift is, for example, $\lambda/2$ for a half-wave plate[10]. The error for deviating from the specified operational wavelength is thus much larger in a multi-order waveplate, however, zero-order plates are much more expensive. I have used wave-plates of both types throughout my experiments, however, I have also used what are known as Fresnel rhombs for the same result when using broadband white light - these are explained in the next section.

2.4.3 Total internal reflection

The optical phenomenon of total internal reflection (TIR) is well known, by which light incident above a certain critical angle[11] at a boundary between a higher refractive index and lower refractive index material is completely reflected (there is no refracted light). What is often not so well known is the more subtle phenomena of “attenuated internal reflection” due to absorption of the evanescent wave, and an accompanied phase-shift upon TIR between orthogonal polarisation components, parallel and perpendicular at the boundary plane of incidence. It is the latter of these which is important for this thesis and so I will go into more detail here.

---

[8] Such as calcite or quartz.

[9] experimentally there is often a very slight attenuation

[10] The reason for doing this is perhaps not obvious, but it would not be practical to manufacture a waveplate for the lab with a thickness of only $\lambda/2$.

[11] Approx. 49° for a water-to-air and 42° for glass-to-air.

Augustin-Jean Fresnel discovered during his work with polarisation in the 1800s, that upon TIR there is an associated non-trivial phase-shift. The polarisation vector of the incident light at a boundary where the condition for TIR is satisfied can be decomposed into two orthogonal components, perpendicular and parallel to the plane of incidence. These are commonly known as s and p polarisation, for perpendicular and parallel, respectively (from the German *senkrecht* and *parallel*, meaning perpendicular and parallel). Fresnel deduced equations for the reflection coefficients for s and p polarisation components (r_s and r_p respectively), which when taking into consideration an exponentially decaying transmitted evanescent wave can be shown as

$$r_s = \frac{n\cos(\theta_i) - i\sqrt{n^2\sin^2(\theta_i) - 1}}{n\cos(\theta_i) + i\sqrt{n^2\sin^2(\theta_i) - 1}} \tag{2.60}$$

and

$$r_p = \frac{n\cos(\theta_i) - in\sqrt{n^2\sin^2(\theta_i) - 1}}{n\cos(\theta_i) + in\sqrt{n^2\sin^2(\theta_i) - 1}}, \tag{2.61}$$

where $n = n_1/n_2$ (the ratio of the refractive index of the two materials) and θ_i is the angle of incidence at the boundary. If $\theta_i > \theta_c$ (where θ_c is the critical angle for TIR to occur), then the magnitude $r_p = r_p = 1$ and only the phase is affected by the reflection. As shown in [46], when the angle of incidence is 45° (an angle of incidence of particular importance for chapter 3 and chapter 4) the relative phase-shift between s and p components is

$$\delta = \arg(r_s) - \arg(r_p) = \arg\left(\frac{n^2 + i\sqrt{1 - 2n^2}}{1 - n^2}\right). \tag{2.62}$$

For a typical glass-air interface (where $n_{\text{glass}} = 1.55$ and $n_{\text{air}} = 1$) the reflection coefficients, phases and phase shift δ are plotted for different θ_i in Figure 2.7. The grey shaded region shows the region above θ_c, where both reflection coefficients are equal to 1 showing TIR. Note that Brewster's angle can be seen on this plot ($\sim 32.8°$) where r_p is 0 and the phase of the p component abruptly changes from 180° to 0°. The dotted line in Figure 2.7 shows a 45° angle of incidence, which coincides with a relative phase-shift of $\sim \pi/4$ (indicated by the solid black line, equal to $\phi_p - \phi_s$).

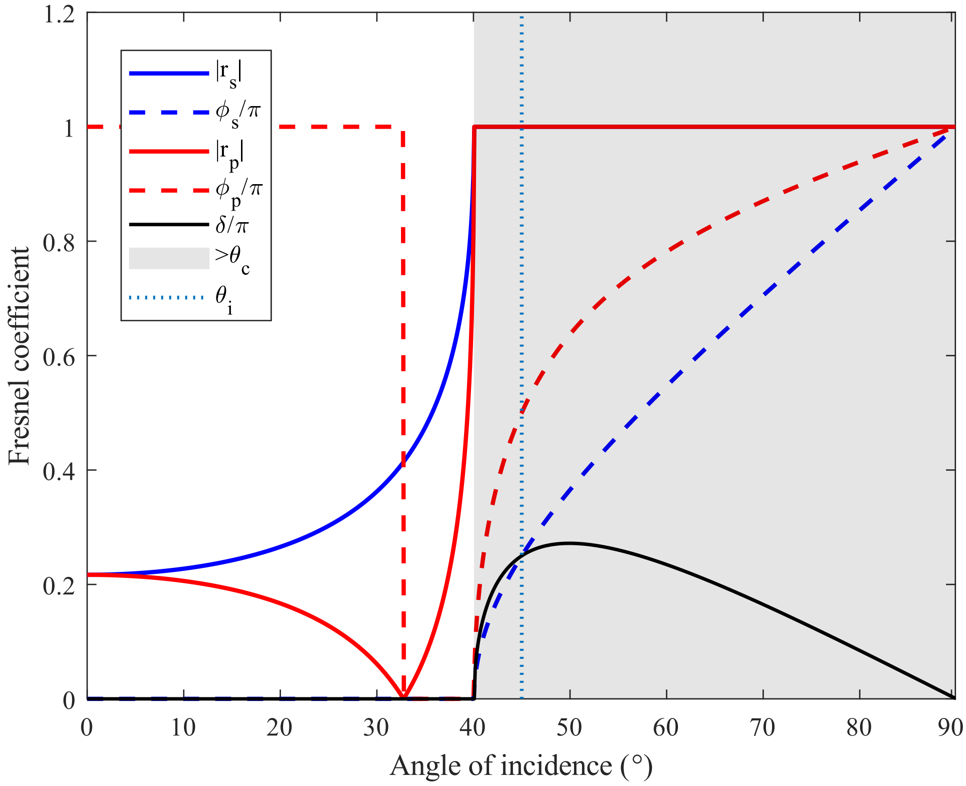

FIGURE 2.7: Fresnel coefficients for angle of incidence at a glass-air boundary.

In glass with $n = 1.51$, a relative phase-shift of $\pi/4$ is achieved for an incidence angle of $\theta_i = 54.6°$. By manufacturing a glass prism with a geometry such that incident light upon a specified front surface undergoes two total internal reflections, each at an angle of $\theta_i = 54.6°$, a component known as a Fresnel rhomb is constructed. A Fresnel rhomb such as this then imposes a $\pi/2$ total phase-shift, akin to the polarisation transformation of a quarter-wave plate. For example, if diagonal linearly polarised light is incident, the final result will be circularly polarised light. As such, the Fresnel rhomb functions similarly to a birefringent quarter-wave plate[12]. Importantly however, the refractive index and thus imparted phase-shift is relatively stable across a broad wavelength range (see Figure 3.4 in subsection 3.3.1) for the Fresnel rhomb and allows achromatic operation. Note also that double Fresnel rhombs are commonly used, which contain four reflections imparting a total π phase-shift (acting as achromatic half-wave plates). On occasion in my work it has been necessary to experiment with polarisation and broadband white light (from

---

[12] I note here for experimental considerations that there is an associated beam-shift/translation of the beam for the output beam with respect to the beam incident to a single Fresnel rhomb (this is not the case with a double-Fresnel rhomb.

an LED source), and as such, I have often used Fresnel rhombs in place of birefringent waveplates (it will be noted where this has been the case in the relevant experimental setup diagrams).

2.5 Propagation and focussing of optical fields

The spatial profile of a light beam evolves upon propagation, so it is useful to be able to calculate this for arbitrary propagation distances. I will detail in this section the key pieces of theory used in the simulations shown for the propagation of optical fields in chapter 3 and the focussing of vector beams in chapter 4.

2.5.1 Angular spectrum representation

The first tool we need for the calculations of beam propagation and focussing by a lens, is the so-called angular spectrum representation. This is a mathematical technique where an electromagnetic field at a particular plane is considered as a decomposition of an infinite sum of plane waves - each with their own amplitudes and directions of propagation. The plane wave decomposition of an electromagnetic field $\mathbf{E}(\mathbf{r})$ is equivalent to the two-dimensional Fourier spectrum at position $\mathbf{r} = (x, y, z)$. As the Fourier spectrum of a beam in a particular image plane ($z =$ constant) is uniquely defined by knowledge of the Fourier spectrum at an object plane ($z = 0$), this consideration allows one to calculate the resulting spatial profile of a light beam for an arbitrary propagation distance using Fourier transforms.

For a chosen z-axis (optical axis), Novotny shows in [48] that the Fourier spectrum $\hat{\mathbf{E}}(k_x, k_y; z)$ of the electric field $\mathbf{E}(x, y, z)$, evolves in the z-direction according to

$$\hat{\mathbf{E}}(k_x, k_y; z) = \hat{\mathbf{E}}(k_x, k_y; 0)\ \mathrm{e}^{\pm i k_z z}, \tag{2.63}$$

where

$$k_z = \sqrt{k^2 - (k_x^2 + k_y^2)}, \tag{2.64}$$

and $|k| = 2\pi/\lambda$. The exponential factor in Equation 2.63 is known as the propagator in reciprocal space [48], and can be used to calculate the Fourier spectrum $\hat{\mathbf{E}}$ at an arbitrary z plane as long as the field is known for the plane at $z = 0$. Thus, the steps to calculate the propagation of a field are as follows:

- Apply a 2D Fourier transform operation to the complex amplitudes,
- Multiply the result of this by the optical propagator in reciprocal space,
- Apply an inverse Fourier transform operation to the result to acquire the propagated field.

This plane wave decomposition method can be summarised in the following equation

$$\mathbf{E}(x,y,z) = \iint_{-\infty}^{\infty} \hat{\mathbf{E}}(k_x,k_y;0)\ \mathrm{e}^{i[k_x x + k_y y \pm k_z z]}\, dk_x dk_y, \tag{2.65}$$

or, with Fourier transforms -

$$\mathbf{E}(x,y,z) = \mathcal{F}^{-1}\left\{\mathcal{F}\left\{\mathbf{E}(x,y,0)\right\}\ \mathrm{e}^{i[k_x x + k_y y \pm k_z z]}\right\}. \tag{2.66}$$

Here, the ± sign allows computation of propagation in either the positive or negative z-direction. When considering polarised light, each polarisation component can be propagated separately, followed by a vector sum of the resulting fields.

In many real-world optical situations, light fields propagate along a chosen direction (usually chosen to be the z-axis) and do not diverge much in the x- and y-directions. When this is the case, geometric optics can be used where ray tracing is applied to approximate the propagation of light through an optical system, by using approximate solutions to Maxwell's equations. More specifically, the square-root of Equation 2.64 from the previous section can be Taylor series expanded as

$$k_z = \sqrt{k^2 - (k_x^2 + k_y^2)} \approx k - \frac{k_x^2 + k_y^2}{2k}, \tag{2.67}$$

where by removing the square root the problem is computationally greatly simplified. This approximation (known as the paraxial approximation) however does not take into account diffraction and interference effects, and relies on the ability to apply the small-angle approximation which is only valid for light propagating at small angles to the optical axis.

2.5.2 Far field approximation

In the near field, optical wavefronts are considered spherical while in the far field wavefronts are considered planar, and so the far field can be an approximation of the optical field far from a focus. Novotny [48] shows that by considering the propagation of a field to a far away point ($\mathbf{r} = \mathbf{r}_\infty$, an infinite distance from the source), the angular spectrum representation of Equation 2.65 becomes

$$\mathbf{E}(x, y, z) = \frac{ir\ \mathrm{e}^{-ikr}}{2\pi} \iint_{(k_x^2+k_y^2)\leq k^2} \mathbf{E}_\infty\left(\frac{k_x}{k}, \frac{k_y}{k}\right)\ \mathrm{e}^{i[k_x x + k_y y \pm k_z z]} \frac{1}{k_z} dk_x dk_y, \tag{2.68}$$

where $r = \sqrt{x^2 + y^2 + z^2}$. While $k_z \approx k$, the result is equivalent to Fourier optics, though this is the limit of Fourier optics, beyond which simple Fourier transforms will not provide the correct result. This far field approximation is useful as the near field region of an optical field would require complicated calculations, however, the result here links the more common far field representation of an optical field with the near field in a Fourier transform pair.

2.5.3 Propagation through a lens

From the last section we find that to calculate the optical field at a focus, we need to know the far field distribution of the electric field. For a strongly focussing lens the paraxial approximation is not valid and focussing of vector beams is most often numerically calculated using the vector diffraction theory of Richards and Wolf [47, 72], more recently summarised in [25, 73] and described in detail in [48]. I will describe the theory below closely following the summaries by Novotny [48] and Zhan [25]. The general idea is a mapping of the incident field in cylindrical into spherical coordinates at a discrete spherical surface in space, with the focal point at the centre. Given that light propagates as Gaussian waves rather than rays, this approach works surprisingly well. An incident electric field $\mathbf{E}_{\text{inc}}$ upon an aplanatic lens must obey two rules - the Abbe sine condition (see Figure 2.8) and the intensity law (see Figure 2.9).

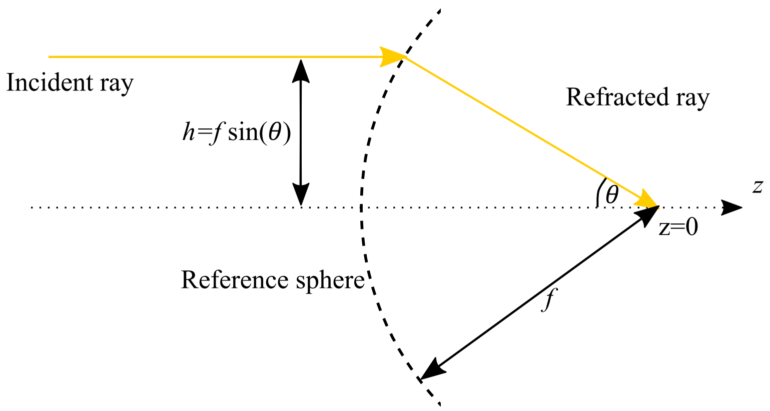

FIGURE 2.8: Diagram showing the sine condition - an ideal aplanatic lens refracts light rays through a reference sphere with radius r. Note that the reference sphere represents refraction due to a change in refractive index. Image adapted from [48]

.

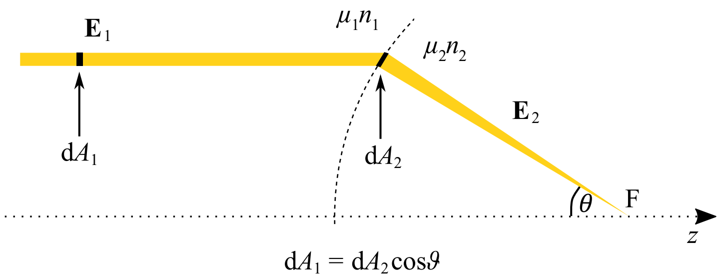

FIGURE 2.9: Diagram of the intensity law, where due to energy conservation the energy carried by a ray must remain constant. Image adapted from [48]

.

The sine condition states that each ray that converges to a focus of an aplanatic lens should intersect with a ray that propagates parallel to the optic axis at a reference sphere of radius f - the focal length of the lens. The distance between the parallel ray and the optic axis is given by

$$h = f \sin(\theta), \tag{2.69}$$

as shown previously in Figure 2.8. Combining the sine condition and the conservation of energy law (the energy transported by a ray must remain constant) results in an intensity law for determining the magnitude of the field just after the lens. This requirement makes sure the energy incident on the lens is the same at the exit pupil. Assuming a magnetic permeability of $\mu = 1$ (a reasonable assumption for most media), the electric fields before the lens and after ($\mathbf{E}_\infty$) should satisfy the following equation,

$$|\mathbf{E}_\infty| = |\mathbf{E}_{\text{inc}}|\sqrt{\frac{n_1}{n_2}}\cos{(\theta)}^{1/2}. \tag{2.70}$$

The incident field $\mathbf{E}_{\text{inc}}$ is a generalised vector beam that may have any allowed spatial distribution of amplitude and polarisation and is assumed to have a planar phase front at the back-aperture or entrance pupil of the objective lens. Vector diffraction theory uses multiple coordinate systems. The table below shows the conventions used in the proceeding theory.

Cylindrical coordinates	
(ρ, ϕ, z)	Arbitrary transverse plane
Cartesian coordinates	
(x, y, z)	Arbitrary point near focus
$(x_\infty, y_\infty, z_\infty)$	Arbitrary point on reference sphere surface
Spherical coordinates	
(r, ϑ, φ)	Arbitrary point near focus
(f, θ, ϕ)	Arbitrary point on reference sphere surface

To calculate refraction by the lens, the problem is simplified by considering the reference sphere as a conversion of $\mathbf{E}_{\text{inc}}$ in a cylindrical coordinate frame to $\mathbf{E}_\infty$ in a spherical coordinate frame, as shown in Figure 2.10. Here I introduce unit vectors $\mathbf{e}_\rho$, $\mathbf{e}_\phi$ and $\mathbf{e}_\theta$, where $\mathbf{e}_\rho$ and $\mathbf{e}_\phi$ are unit vectors of a cylindrical system and $\mathbf{e}_\theta$ and $\mathbf{e}_\phi$ are of a spherical system [48]. The incident electric field at the reference sphere can be decomposed into an s and p component, where, using cylindrical unit vectors these are

$$\mathbf{E}^s_{\text{inc}} = \left[\mathbf{E}_{\text{inc}} \cdot \mathbf{e}_\phi\right]\mathbf{e}_\phi, \tag{2.71}$$

and

$$\mathbf{E}^p_{\text{inc}} = \left[\mathbf{E}_{\text{inc}} \cdot \mathbf{e}_\rho\right]\mathbf{e}_\rho. \tag{2.72}$$

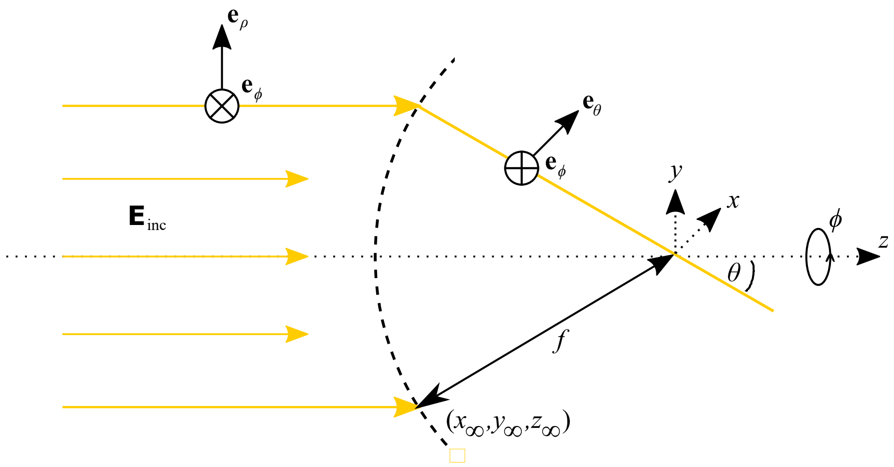

FIGURE 2.10: Definition of coordinates and unit vectors for conversion from cylindrical frame to spherical frame at reference sphere. Image adapted from [48].

It can be seen in Figure 2.10 that upon refraction at the reference sphere, the unit vector $\mathbf{e}_\phi$ is unaffected, while $\mathbf{e}_\rho$ is mapped to $\mathbf{e}_\theta$ in the spherical system. Taking into account the sine condition and intensity law shown previously for the aplanatic system, the field after refraction is then,

$$\mathbf{E}_\infty = \left[\left[\mathbf{E}_{\text{inc}} \cdot \mathbf{e}_\phi \right] \mathbf{e}_\phi + \left[\mathbf{E}_{\text{inc}} \cdot \mathbf{e}_\rho \right] \mathbf{e}_\theta \right] \sqrt{\frac{n_1}{n_2}} \cos\left(\theta\right)^{1/2}. \tag{2.73}$$

If s and p Fresnel transmission coefficients are needed, these can easily be included. The following transformations allow the expression of $\mathbf{e}_\rho$, $\mathbf{e}_\phi$ and $\mathbf{e}_\theta$ in Cartesian unit vectors using spherical coordinates θ and ϕ:

$$\mathbf{e}_\rho = \cos\left(\phi\right)\mathbf{e}_x + \sin\left(\phi\right)\mathbf{e}_y \tag{2.74}$$

$$\mathbf{e}_\phi = -\sin\left(\phi\right)\mathbf{e}_x + \cos\left(\phi\right)\mathbf{e}_y \tag{2.75}$$

$$\mathbf{e}_\theta = \cos\left(\theta\right)\cos\left(\phi\right)\mathbf{e}_x + \cos\left(\theta\right)\sin\left(\phi\right)\mathbf{e}_y - \sin\left(\theta\right)\mathbf{e}_z. \tag{2.76}$$

Inserting these into Equation 2.73 provides the field at the reference sphere in Cartesian unit vectors, as

$$\begin{aligned}\mathbf{E}_{\infty}(\theta,\phi) = &\left(\mathbf{E}_{\text{inc}}(\theta,\phi)\cdot\begin{bmatrix}-\sin{(\phi)}\\ \cos{(\phi)}\\ 0\end{bmatrix}\right)\begin{bmatrix}-\sin{(\phi)}\\ \cos{(\phi)}\\ 0\end{bmatrix}\sqrt{\frac{n_1}{n_2}}(\cos{(\theta)})^{1/2}\\ &+\left(\mathbf{E}_{\text{inc}}(\theta,\phi)\cdot\begin{bmatrix}\cos{(\phi)}\\ \sin{(\phi)}\\ 0\end{bmatrix}\right)\begin{bmatrix}\cos{(\phi)}\cos{(\theta)}\\ \sin{(\phi)}\cos{(\theta)}\\ -\sin{(\theta)}\end{bmatrix}\sqrt{\frac{n_1}{n_2}}(\cos{(\theta)})^{1/2}\end{aligned} \tag{2.77}$$

It can be beneficial to re-state the far field angular spectrum representation of Equation 2.68 in spherical coordinates rather than in terms of k_x and k_y due to the symmetry of the system in a spherical frame. In order to carry out the diffraction integral over a solid angle in θ and ϕ instead of the planar integration over k_x and k_y in Equation 2.68, Richards and Wolf [47] show the following conversion can be used for the differentials,

$$\frac{1}{k_z}dk_x dk_y = k\sin{(\theta)}d\theta d\phi. \tag{2.78}$$

Finally, by replacing r with the focal length of the lens f, and limiting the integration to the maximum focussing angle of the lens θ_{max}, given by the numerical aperture of the lens, $\text{NA} = n\sin{(\theta_{\text{max}})}$, the focal field can be evaluated using

$$\mathbf{E}(\rho,\phi,z) = -\frac{ikf\ \mathrm{e}^{-ikf}}{2\pi}\int_0^{\theta_{\text{max}}}\int_0^{2\pi}\mathbf{E}_{\infty}(\theta,\phi)\ \mathrm{e}^{ik_z\cos{(\theta)}}\ \mathrm{e}^{ik\rho\sin{(\theta)}\cos{(\phi-\varphi)}}\sin{(\theta)}\,d\phi d\theta. \tag{2.79}$$

With Equation 2.77, this allows the evaluation of the focal field $\mathbf{E}(\rho,\phi,z)$ for any incident field $\mathbf{E}_{\text{inc}}$, using the far field approximation $\mathbf{E}_{\infty}(\theta,\phi)$ at the reference sphere of an aplanatic lens.

Chapter 3

Polarisation structuring with a Fresnel cone

3.1 Introduction

The polarisation property of light has been known about for hundreds of years, however, only relatively recently has polarisation been used in technology, with the use of spatially dependent states being a current popular subject [25]. In chapter 1 some applications benefiting from spatially structured vector light were given - for a review of complex vector light field applications see [74]. During my master's project, I contributed to work where we showed that light's polarisation (and phase) can be structured through back-reflection from a solid glass cone [46]. My research has continued this work, expanding and improving upon, and investigating where Fresnel cone beams can be applied practically. In chapter 4 I will show how beams generated using a Fresnel cone reveal interesting results when tightly focussed. Conversely, in chapter 5 I show how a Fresnel cone can not only be used to generate useful polarisation states, but also to measure the unknown polarisation of an incident light beam. In this chapter I will highlight some known methods for polarisation structuring from the literature, before detailing the theory and experimental techniques of the Fresnel cone polarisation structuring. I will also describe a new coupling device developed for use with the Fresnel cone for generating high efficiency annular vector vortex beams.

My contributions to this work included setting up and performing experiments to enhance cone beam fidelity, to collaboratively test an axicon-coupling technique, to simulate Fresnel cone Poincaré beam generation, and co-writing the manuscript-in-preparation titled ‘High-efficiency high-NA vector beams from a Fresnel cone’.

3.2 Polarisation structuring in the literature

There have been numerous techniques developed to generate beams of light with structured polarisation. These are sometimes categorised as being either an active or passive method, where active techniques convert the polarisation state inside the laser cavity, while in passive techniques the polarisation conversion is done outside of the cavity (here laser output is usually linearly or circularly polarised). This categorisation of the various methods was reviewed in detail by Q. Zhan [25]. More relevant to my work is the distinction between a static generation component and one which allows dynamic control - here I will review cases of both, before providing a full description of structured polarisation generation using a Fresnel cone.

3.2.1 Static generation methods

As discussed in subsection 2.4.2, the most common optical components for manipulating the polarisation state of a light beam use birefringent materials. Many of the early designs for polarisation structuring are focussed on the generation of radially polarised light, since this showed potential for application in the mid-2000s (as explained in chapter 1). A common approach was to use a ‘radial analyser’ - a system using birefringent components with the resulting polarisation transmission axis aligned in the radial direction [75]. The required input for this system is circularly polarised light, which can be expressed in terms of unit vectors in a polar coordinate frame as

$$\begin{aligned}\mathbf{E}_{\mathrm{in}} = \mathbf{e}_{\mathrm{x}} + i\mathbf{e}_{\mathrm{y}} &= (\cos(\theta)\mathbf{e}_{\mathrm{r}} - \sin(\theta)\mathbf{e}_{\theta}) + i(\cos(\theta)\mathbf{e}_{\mathrm{r}} + \sin(\theta)\mathbf{e}_{\theta}) \\ &= \mathrm{e}^{\mathrm{i}\theta}(\mathbf{e}_{\mathrm{r}} + \mathrm{i}\mathbf{e}_{\theta}),\end{aligned} \tag{3.1}$$

where $\mathbf{e}_{\mathrm{x}}$ and $\mathbf{e}_{\mathrm{y}}$ are unit vectors in a Cartesian coordinate frame and $\mathbf{e}_{\mathrm{r}}$ and $\mathbf{e}_{\theta}$ are unit vectors in a polar coordinate frame (θ being azimuthal angle). Upon transmission through a radial analyser, $\mathbf{E}_{\mathrm{out}} = \mathrm{e}^{\mathrm{i}\theta}\mathbf{e}_{\mathrm{r}}$, where the unit vector is in the radial direction only, however, the output beam has gained a spiral phase factor (this is a geometric phase, or Pancharatnam-Berry phase [43]). In chapter 4 I show that the global phase is crucial to the focussing properties of a beam, and so this additional spiral phase may not be desirable for the generated radially polarised beam. This phase could be compensated for using a variety of methods, but all add additional components or limitations to the setup.

Given instead a linearly polarised input, to convert this to a radially polarised beam the polarisation at each point in the transverse plane must be rotated by azimuthally varying amounts. By taking four waveplate segments, each rotated differently to give varying fast-axis orientations, Quabis et al. was able to generate a radially polarised beam [76], and later an eight-segmented waveplate was constructed by Machavariani et al. to produce a more continuous radially polarised beam [77] (both cases diagramatically shown below in Figure 3.1). Perhaps obvious however, these segmented waveplates produce only approximate radially polarised beams due to the finite number of the individual segments, and the discontinuity between the segments.

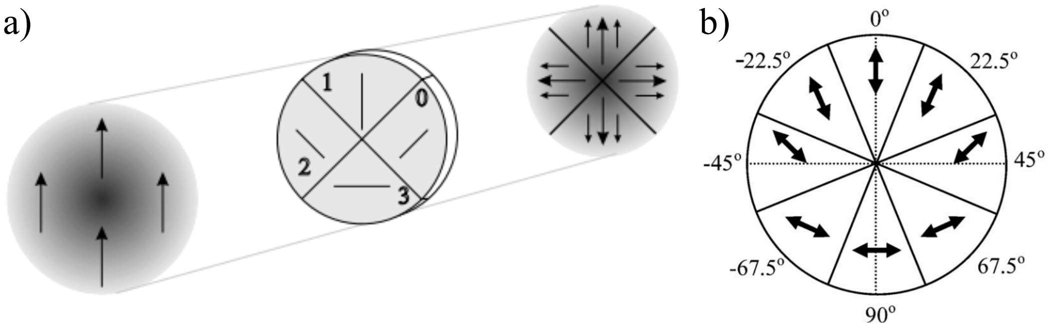

Figure 3.1: a) Four-segment and b) eight-segment waveplates for generating radially polarised light by Quabis et al. and Machavariani et al., respectively. Images adapted from [76] and [77].

Progressing forward a decade from the work of the previous paragraph, and active generation of a variety of vector beams with [78] and without [79] optical vortices is demonstrated using devices called q-plates (though these were first introduced circa 2006 - for a recent review of q-plate development see [80]). These are constructed using dynamic photo-lithography techniques to photo-align a layer of ‘rice-shaped’ birefringent liquid crystals on a substrate (oriented in the x-y plane at predefined angles), providing the potential for an assortment of passive components that allow a variety of vector beams generation.

Most recently, it was shown that a variety of interesting vector beams can be generated using graded index (GRIN) lenses in 'cascade' setups [81]. These lenses have been previously used in on-chip waveguide coupling [82] as well as in microendoscopy [83] due to their small compact size. During fabrication of the rod-shaped lens, an azimuthally symmetric refractive index profile is created. Additionally during fabrication, a (normally) undesirable birefringence profile is created that has a radially increasing retardance that is fixed at a given radius, and azimuthally orientated fast-axis. The result for polarisation manipulation is that a GRIN lens can be thought of as an array of tiny waveplates, with spatially dependent retardance and fast-axis orientation. For example, Figure 3.2 below shows the output polarisation state for a circularly polarised input to a single GRIN lens - demonstrated by He et al. [81].

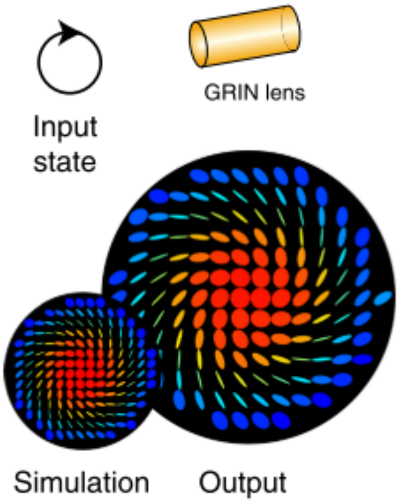

FIGURE 3.2: Polarisation profile for operation of a single GRIN lens on a circularly polarised input. Image from [81].

As GRIN lenses are already used in certain medical imaging applications there is potential for development of GRIN lens Stokes and Mueller matrix polarimetry, to aid in diagnosis. Polarimetry as mentioned earlier will be the subject of chapter 5.

There are obvious benefits to using static components for vector beam generation, whatever the application may be, due to the inherent robustness and stability. The above discussed components however, each rely on birefringent material - limiting operation to monochromatic light.

3.2.2 Dynamic generation methods

The previous section showed examples of the generation of vector beams using simple static components, however, dynamic polarisation state generation may be more desirable. With the increased availability of spatial light modulators (SLMs) in recent years, various methods have been developed for the complete arbitrary control of a light beam's amplitude, phase and polarisation. The most common SLMs used are liquid crystal based, consisting of an array of individual 'rice-shaped' liquid crystals. These liquid crystals are birefringent, and are usually oriented horizontally (parallel to the laboratory optical table). Their alignment can be controlled by passing an electric field through them changing their inclination angle to the propagation direction. This essentially changes the path length and the resulting polarisation dependent phase-shift magnitude.

Using additional polarisation optics, arbitrary control has been demonstrated using two phase-only SLMs [84]. Here a cascade of two SLMs is used in a $2f$ setup, where the first SLM displays a hologram projecting the desired amplitude in the plane of the second SLM, which subsequently is used to modulate the phase. Alternatively, amplitude can be controlled by changing the blazing height of a spatially resolved blazed grating displayed on an SLM, changing the diffraction efficiency in the first order [85]. More complex setups have managed arbitrary control using only a single SLM [86, 87]. Generally, vector beam generation using SLMs involves shaping the horizontal and vertical polarisation components separately and then superimposing [88, 89] - for a review of SLM beam generation techniques see [28].

Recently, another type of SLM has gained popularity for generating complex vector light fields, known as a digital micro-mirror device (DMD) [90, 91]. While liquid crystal SLMs require specific linearly polarised inputs, DMDs have been shown to be polarisation insensitive [31, 92]. Complex vector light beam generation with a single DMD is possible by first spatially separating an incident beam into two orthogonal polarisation components. These individual beams are directed to the DMD plane, at which point two multiplexed holograms are displayed (each independently controllable). For vector beam generation, each hologram encodes the desired amplitude and phase of a Laguerre-Gauss mode (in Rosales-Guzman et al. system [31] - other mode pairs can be used such as the Hermite-Gauss modes [93]), which are then spatially overlapped in the first diffraction order resulting in the final beam. Though this system is not restricted to linearly polarised light, it is however highly inefficient as the first diffraction order contains $\sim 10\%$ of the total input power, and broadband operation remains an issue.

3.3 Fresnel cone theoretical description

In the last section I highlighted both static and dynamic methods for polarisation structuring, however, these are for the most part restricted to monochromatic light or involve complex setups. In this section I will detail the operation of the central component investigated throughout this thesis - the so-called Fresnel cone [46] (see photograph below).

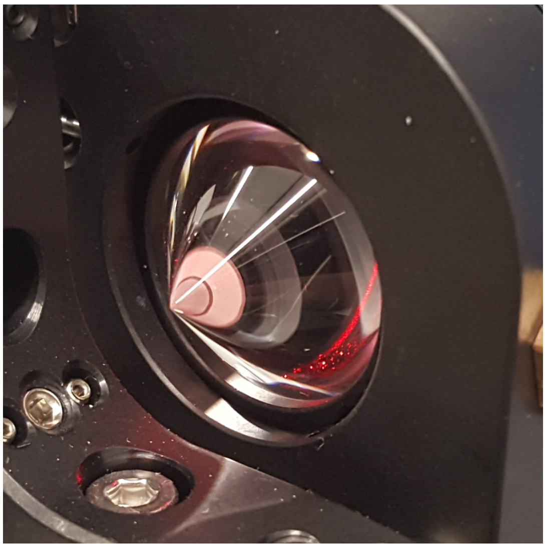

Figure 3.3: Photograph showing the rear side of a mounted Fresnel cone with a 90° apex.

When light is incident at the front surface of a solid glass cone with a 90° apex angle, the angle of incidence at the rear surface is above that required for total internal reflection to occur. This means that the beam is completely reflected and exits the cone in the opposite direction it entered. As shown in subsection 2.4.3, when light undergoes total internal reflection at a boundary such as this, between glass and air, Fresnel's equations predict a phase-shift between the orthogonal s and p polarisation components. Given the conical geometry the decomposition of the initial polarisation state into s and p components varies azimuthally around the cone tip, resulting in an azimuthally varying polarisation state in the output beam. As stated in [46], in addition to the phase induced upon TIR there is also a spin redirection phase that occurs during Fresnel cone back reflection. This will be discussed in more detail shortly, but the result is a conversion of spin angular momentum to orbital angular momentum[1]. I note here that Bouchard et al. reported a related approach to vector vortex beam generation using TIR, using two glued hollow axicons [95]. An advantage of using a single Fresnel cone is that it does not require any spatial splitting of the incident beam and recombination. Similar methods for generating vector beams without OAM have also been previously reported [96, 97].

To determine the polarisation effects of the Fresnel cone, I will next show how the Jones calculus approach described in chapter 2 can be used. Using the Fresnel reflection coefficients described in subsection 2.4.3, r_s and r_p, from [46] in an *s*-*p* eigensystem the Jones matrix for two TIR reflections is then

$$\mathbf{M}_\mathrm{wedge} = \begin{bmatrix} r_\mathrm{p}^2 & 0 \\ 0 & r_\mathrm{s}^2 \end{bmatrix} = r_\mathrm{p}^2 \begin{bmatrix} 1 & 0 \\ 0 & \mathrm{e}^{\mathrm{i}2\delta} \end{bmatrix}, \tag{3.2}$$

where δ is given in subsection 2.4.3. During my research I have used three generations of Fresnel cones. The first generation are aluminium-coated N-BK7 glass cones from Edmund Optics (the aluminium was first etched away to reveal the glass-air boundary). The second and third generation cones are both H-BaK6 glass from G&H and Laser Components, respectively. This glass was chosen specifically for the second and third generation cones as it provides an *s*-*p* phase-shift of 0.25π (to 2 s.f.) at each reflection, compared to the first generation cones for which $\delta = 0.22\pi$ (to 2 s.f.), when used at a wavelength of 850 nm. The choice to manufacture cones for use at 850 nm is due to common applications operating at this wavelength - discussed in chapter 4. See Table 3.1 below for specifications.

Generation	∅	**Material**	n (633/850 nm)	δ (633/850 nm)
First	10 mm	N-BK7	1.52/1.51	0.22/0.22 π
Second	15 mm	H-BaK6	1.56/1.56	0.26/0.25 π
Third	25 mm	H-BaK6	1.56/1.56	0.26/0.25 π

TABLE 3.1: Table showing specifications for the three generations of Fresnel cones used throughout my research. n and δ are to 2 significant figures.

---

[1] This is true for both solid glass cones as well as reflection in metallic cones [94].

By using rotation matrices (given in chapter 2), the input polarisation state in an x-y coordinate system can be rotated into the s-p eigensystem of the Fresnel cone, then operated on by the two TIRs given in the form of $\mathbf{M}_{\text{wedge}}$ above, before using a second rotation matrix to rotate back into the x-y coordinate frame as follows,

$$\mathbf{M}_{\text{cone}} = \mathbf{R}(-\phi)\mathbf{M}_{\text{wedge}}\mathbf{R}(-\phi). \tag{3.3}$$

Here I note that due to the change of sense of rotation by the conical back-reflection, the rotation matrices must be in the same direction in order to rotate back into the original x-y coordinate frame.

Due to the cylindrical symmetry of the Fresnel cone, it is advantageous to use a circular polarisation basis (σ_+,σ_-) to describe the action of the device [46]. This results in a simplification of the Jones matrix, and it is shown that when for example right-handed circularly polarised light is input into the cone,

$$\sigma_+ \rightarrow -i\mathrm{e}^{(\Phi_s+\Phi_p)}\left[\mathrm{e}^{i2(\phi+\pi/4)}\cos{(\delta)}\sigma_+ + \sin{(\delta)}\sigma_-\right]. \tag{3.4}$$

In this case, $2\hbar$ units of OAM have been acquired by the right-handed circular polarisation components and none in the left. Assuming a Fresnel cone with the exact refractive index to provide $\delta = \pi/4$ this simplifies to

$$\sigma_+ \rightarrow -\frac{i}{\sqrt{2}}\mathrm{e}^{(\Phi_s+\Phi_p)}\left[\mathrm{e}^{i2(\phi+\pi/4)}\sigma_+ + \sigma_-\right]. \tag{3.5}$$

Here, the amounts of left and right handed circular polarisation are equal, with a phase shift varying azimuthally around the cone tip. The polarisation profile is thus linear everywhere but with azimuthally varying orientation. When considering an ideal phase-shift of $\delta = \pi/4$ at each reflection, the result of linearly polarised light at each transverse point makes sense, as a total phase-shift of $2\delta = \pi/2$ is the same a quarter-wave plate - often used for converting linear to circularly polarised light and vice-versa. I will show both simulated and experimental results for varying input states to a Fresnel cone in section 3.4, in the form of spatially resolved polarisation plots using the ellipticity visualisation previously shown in Figure 2.4. I note here to demonstrate the potential flexibility of Fresnel cone use, that by manufacturing different cones with different refractive indices, a range of δ values can be achieved, as shown in Figure 3.4 below.

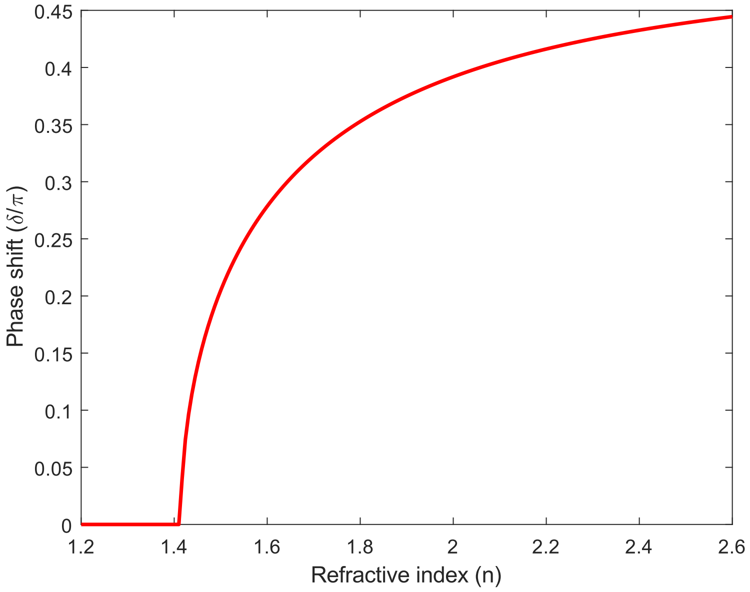

FIGURE 3.4: The theoretical phase-shift acquired between s and p polarisation components upon TIR for increasing refractive index (for an angle of incidence of 45°), calculated using the complex amplitude Fresnel equations for reflection coefficients.

3.3.1 Broadband nature

Unlike many optical components used for modulating light's polarisation property, the Fresnel cone does not rely on birefringence. Instead as mentioned, the phase-shifts that occur between orthogonal polarisation components are reliant upon the refractive index of the cone material, and importantly the geometry of the cone, which determines the s and p decomposition at the boundary where TIR occurs. In glass, refractive index varies only slowly with wavelength for large wavelength ranges, and so can be considered essentially constant for the purposes of the Fresnel cone. Cauchy's equation[2] is well known and describes the dispersion relationship between refractive index and wavelength, which I use to examine this relationship for different types of glass below. Cauchy's equation is

$$n(\lambda) = A + \frac{B}{\lambda^2} + \frac{C}{\lambda^4} + ..., \tag{3.6}$$

where n is the refractive index, λ is the wavelength and A, B, C and so on are constants that can be determined by fitting the equation at known wavelengths to measured refractive indicesI note that Cauchy's equation is only valid for dispersion

---

[2] Defined in 1836 and named after Augustin-Louis Cauchy.

in the visible region and the Sellmeier equation must be used when considering the ultraviolet or infrared regions.. For most cases it is adequate to employ just the two-term equation

$$n(\lambda) = A + \frac{B}{\lambda^2}, \tag{3.7}$$

since higher terms become negligibly small. The constants A and B are well known for common types of glass and are shown in Table 3.2 below (from [78]).

Material	$\boldsymbol{A}$	$\boldsymbol{B}(\mu\mathrm{m}^2)$
Fused silica	1.4580	0.00354
Borosilicate glass BK7	1.5046	0.00420
Hard crown glass K5	1.5220	0.00459
Barium crown glass BaK4	1.5690	0.00531
Barium flint glass BaF10	1.6700	0.00743
Dense flint glass SF10	1.7280	0.01342

Table 3.2: Table showing values for A and B constants for Cauchy's equation for common types of glass.

Using these known constants and Equation 3.7 I show the relationship between refractive index and wavelength below in Figure 3.5.

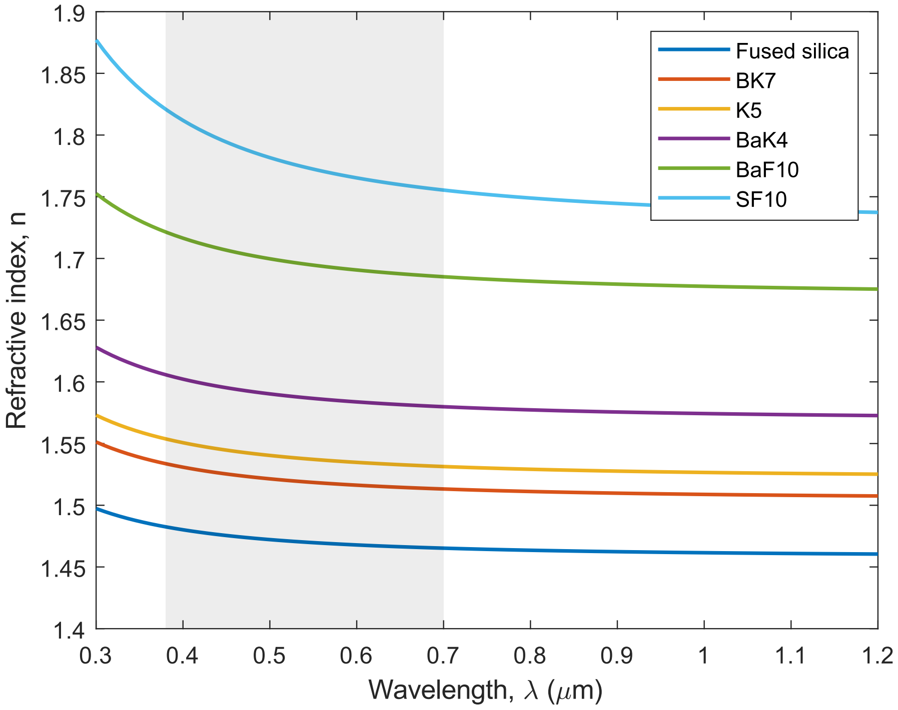

FIGURE 3.5: Refractive index versus wavelength for some common glass types. The visible region is highlighted in the grey box.

This enables the optimum selection of glass material for the Fresnel cone depending on the wavelength in use, optimising for δ in Equation 2.62. As was earlier stated, for the second and third generation cones obtained, H-BaK6 glass was selected as the cone material due to providing a close to ideal phase-shift value of $\delta = \pi/4$ at a wavelength of 850 nm. This is a typical operating wavelength of scanning microscopes and will be discussed more in the next chapter.

3.4 Fresnel cone experimental technique

In this section I will describe the typical experimental setup for coupling light into a Fresnel cone and subsequently measuring its polarisation profile. In order to plot spatially resolved polarisation ellipses for visualisation of the generated beam's transverse polarisation profile, measurement of the Stokes vector described in subsection 2.3.2 must be carried out. This involves taking six images of the beam's intensity profile on a camera after projection into the six polarisation basis states, namely horizontal (H), vertical (V), diagonal (D), anti-diagonal (A), right-circular

(R) and left-circular (L). The setup for Fresnel cone beam generation and Stokes measurement is shown below in Figure 3.6.

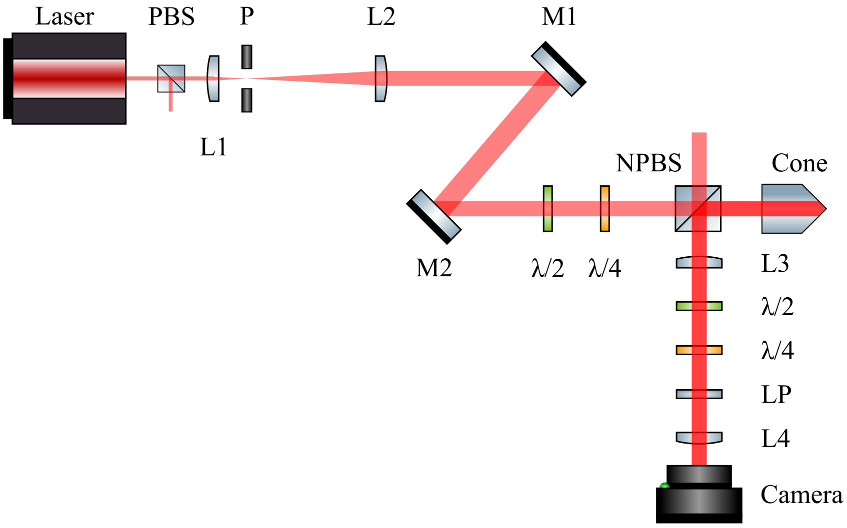

FIGURE 3.6: Experimental setup used to generate Fresnel cone beams and perform Stokes measurement. PBS is a polarising beam-splitter. NPBS is a 50:50 non-polarising beam-splitter. L1-4 are lenses f=50, 200, 175, 25 mm respectively. P is a 10 μm pinhole. M1-2 are mirrors (angle not to scale). $\lambda/2$ and $\lambda/4$ are half- and quarter-wave plates respectively, and LP is a linear polariser.

In the above setup, the light source used is a 633 nm Helium Neon laser. The polarising beam-splitter (PBS) is used to provide an initial horizontally polarised state. Lens (L1, $f = 50$ mm) and 2 (L2, $f = 200$ mm) are positioned at the sum of their focal lengths apart, forming a $2f$ telescope system. This, combined with the 10 μm pinhole (P) perform two tasks: (1) the pinhole spatially filters the beam, removing noise and leaving a clean Gaussian intensity profile and (2) the telescope expands the diameter of the beam to fill the aperture of the Fresnel cone. Mirrors 1 and 2 (M1 and M2) are used for beam steering to aid in alignment into the cone. The initial half- and quarter-wave plate ($\lambda/2$ and $\lambda/4$) are used to operate on the horizontally polarised beam to generate any desired uniformly polarised state. The non-polarising beam-splitter (NPBS) is a 50:50 transmission:reflection ratio beam-splitter, used to couple light in and out of a Fresnel cone. I note here that the result of this coupling method is a maximum 25% efficiency, due to the two passes through the beam-splitter. Lenses 3 (L3, $f = 175$ mm) and 4 (L4, $f = 25$ mm) are used to image the cone surface plane to the camera, as well as to de-magnify the beam diameter to fit onto the camera sensor. In the measurement arm, the half-wave plate ($\lambda/2$) is used to rotate the generated state (this will be discussed later in this section), and the final quarter-wave plate ($\lambda/4$) and linear polariser (LP) is used to project the beam into the six polarisation basis states. Examples of the six data images taken when an azimuthally polarised beam is generated, are shown below in Figure 3.7.

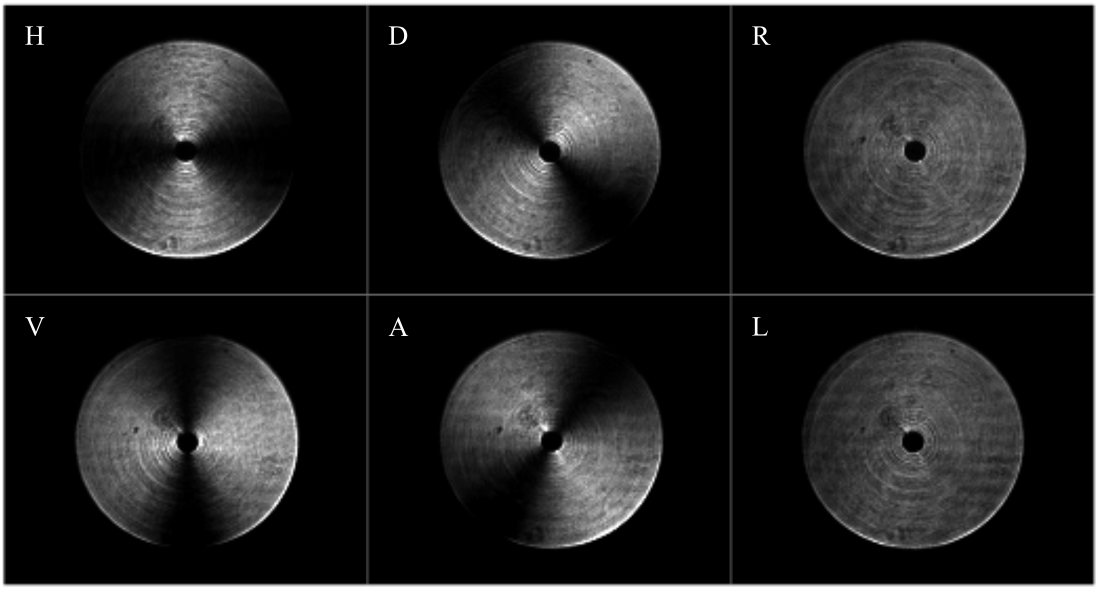

FIGURE 3.7: Six data images taken when generating azimuthally polarised light, labelled with the basis state the beam is measured in.

The above data shows that there is maximal intensity for the linear polarisation orientations (H, V, D and A) in the correct regions when considering an azimuthally polarised input, and similarly minimal intensity in the orthogonal linear orientation (in this case being the orthogonal radial direction). For example, azimuthally polarised light has horizontal polarisation along the vertical axis (maximum intensity in H image above) and vertical polarisation on the horizontal axis (maximum intensity in V image above). Also correctly for an azimuthally polarised input, there is an even intensity distribution observed in each of the circular polarisation bases (R and L) - as noted in subsection 2.2.2 linearly polarised light contains equal contributions of both right and left circular components. From these six images, spatially resolved Stokes vectors can be calculated and polarisation ellipses plotted using the definition detailed in subsection 2.3.5. Examples of the spatially dependent polarisation profiles generated by a Fresnel cone for three different input states are shown below in Figure 3.8, from both simulation and experiment. I note here that throughout this thesis I have chosen to calculate polarisation ellipses for a resolution of 21x21 super-pixels, where the ellipse plotted is an average Stokes vector for that super-pixel, following the colour mapping shown in Figure 2.4. The simulation was performed using the Jones calculus approach described in subsection 2.3.1.

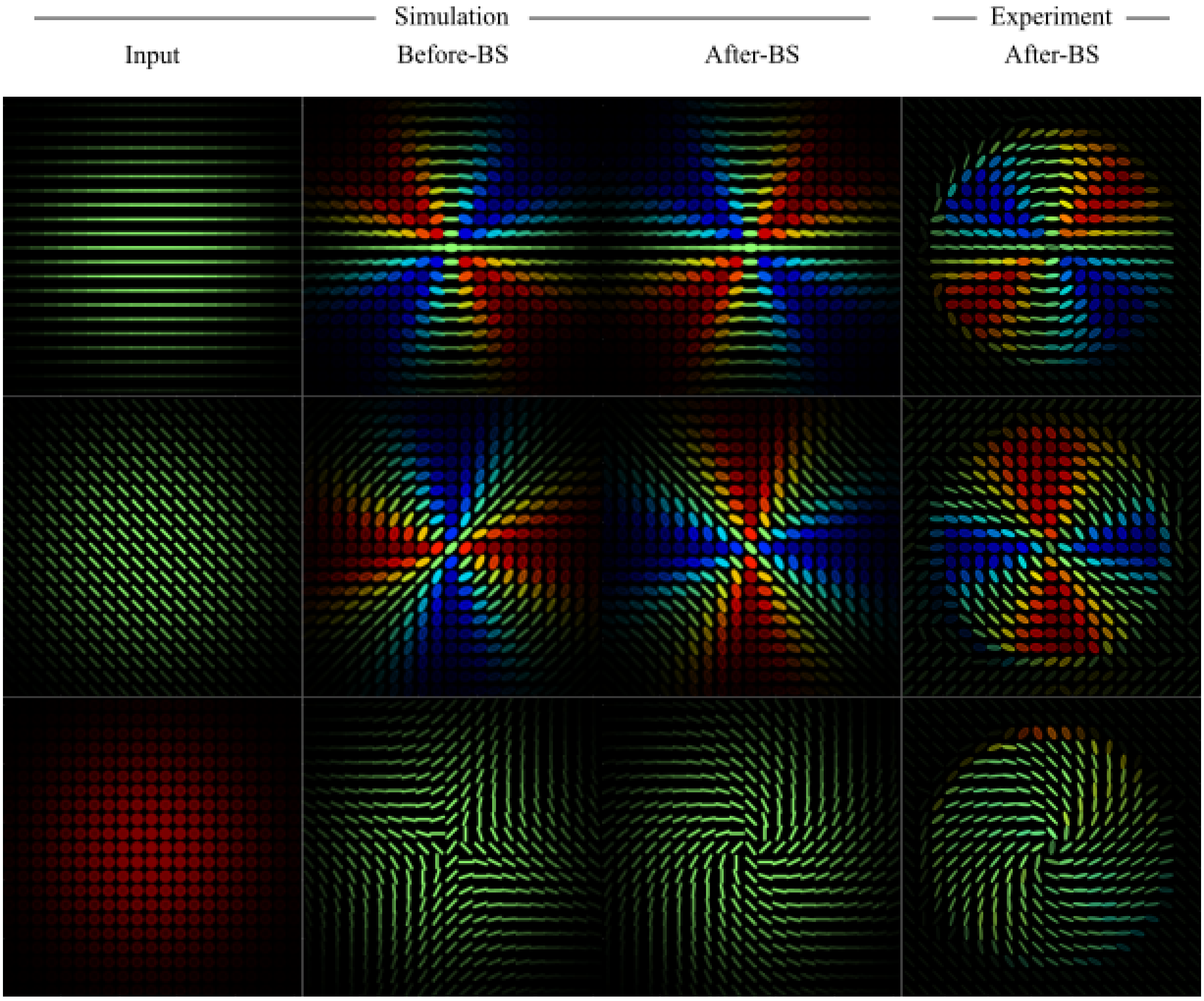

FIGURE 3.8: Example data from simulation and experiment showing 2D transverse polarisation profiles for three different input states into a Fresnel cone. First row shows horizontally polarised input, second row diagonal and third row right-hand circular. The results are shown for the polarisation profile before and after the experimental beam-splitter (BS) reflection, as in reality this must be accounted for as the state prior to it can not be measured with the current setup.

Above in Figure 3.8 it is seen that the experimentally measured polarisation profile of the generated cone beams closely matches theoryI note that in the experiment the Fresnel cone was overfilled, and so the experimental data does not display the same Gaussian intensity profile as the simulation.. Interestingly, starting from the horizontal position, the polarisation detected in the azimuthal direction is the same polarisation state that would be generated by a quarter-wave plate at that orientation angle, for that given input. This means that the Fresnel cone provides a spatial mapping of the temporal rotation of a quarter-wave plate - something that will become useful for polarimetry in chapter 5. As shown in the previous section, for a circularly polarised input state the result is everywhere linearly polarised light (equal amounts of right and left circular polarisation), but with varying orientation angle. The key to this varying orientation angle is in the OAM generated in one of the circular components, providing an azimuthally varying phase-shift between the two circular components, and thus an azimuthally varying orientation of linearly polarised light. Upon operation of a half-wave plate on the linearly polarised output structure from a circular input beam, the linear polarisation orientation can be everywhere rotated. This allows conversion from the generated beam to either radial or azimuthally polarised light by rotation of the half-wave plate by ±22.5° from a horizontally positioned fast-axis[3]. Results for simulated and experimentally measured radial and azimuthal polarisation is shown below in Figure 3.9.

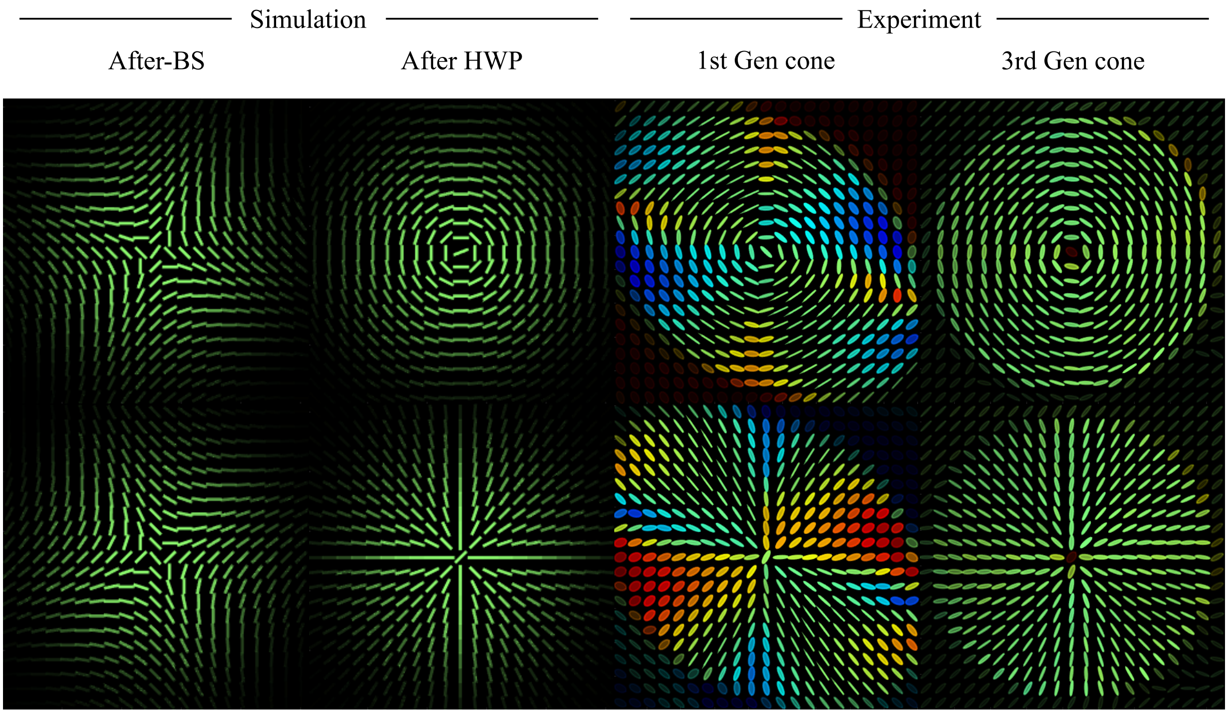

Figure 3.9: Simulated and experimental spatially resolved polarisation plots showing azimuthal (top row) and radial (bottom row) polarisation states generated from right and left circular input to a Fresnel cone. Experimental results are shown for both the 1st generation cones as was used in [46] and with 3rd generation cones. BS is a non-polarising beam-splitter and HWP is a half-wave plate at ±22.5°.

---

[3] More generally, all super-positions of radial and azimuthal polarisation can be created through transformation with a half-wave plate.

Above, I have recreated the results of [46] for the first generation Fresnel cone for comparison with the enhanced fidelity[4] of the generated states with the higher quality third generation cone. This improvement is largely due to acquisition of newly manufactured cones with a refractive index that provides a δ value closer to $\pi/4$ ($\pi/2$ total for both reflections), resulting in equal contributions of both right and left circular polarisation in the generated beam (see Equation 3.4). The significance of these beams will be discussed more in the following chapters, where applications are shown.

3.4.1 High efficiency coupling using an axicon

In the last section, describing the experimental technique to generate vector beams using a Fresnel cone, it was shown that the most simple method for coupling light in and out of the cone is to use a 50:50 non-polarisation beam-splitter. This method is relatively straight-forward as far as beam-alignment goes, however, it allows maximally a 25% efficiency. Certain potential applications for broadband vector beam generation use high-power lasers, where efficiency is critical. For this reason, alternate coupling methods were investigated for the Fresnel cone beam generation. In chapter 4 I will detail a coupling technique based on a 'dual cone-based polariser' design, which was developed as part of an industry-led collaborative project forming a major component. This method uses complex beam-splitter geometries and two Fresnel cones to provide high efficiency coupling. In the remainder of this section I will show an alternate method for coupling light into a Fresnel cone using a holed-mirror and axicon. This technique allows broadband operation and close to 100% efficiency is demonstrated. In addition to this, the intensity profile of an incident Gaussian beam is inverted to an annular beam. This may be beneficial for some applications, such as high numerical aperture microscopy.

An axicon can be thought of as a rotationally symmetric prism, and is often used for Bessel beam generation [98, 99]. Containing one flat surface and one conical surface it is similar to a Fresnel cone, but with much smaller apex angle. This smaller angle does not allow TIR to occur as in the Fresnel cone, and the action is in some ways similar to that of a lens (see Figure 3.10). Axicons are usually manufactured to have a physical angle (θ_1 in Figure 3.10) of $0.5 - 40°$ - for comparison this angle

---

[4] Fidelity can be determined by averaging the absolute error of the Stokes parameters from the ideal case.

in a Fresnel cone is 45°. Using Snell's law the deflection angle of an axicon can be found:

$$n \sin(\theta_1) = \sin(\theta_1 + \theta_2), \tag{3.8}$$

where n is the refractive index of the axicon, θ_1 is the physical angle of the axicon and θ_2 is the angle of deflection of the light to the optic axis.

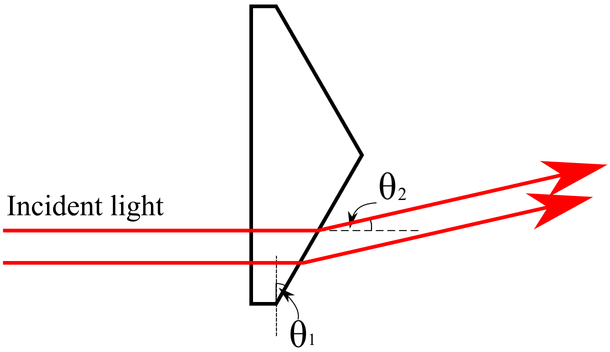

FIGURE 3.10: Diagram showing an axicon (angles not to scale). θ_1 is the physical angle of the axicon and θ_2 is the deflection angle of the beam to the optic axis.

Below in Figure 3.11 I show a sketch-diagram to outline the basic idea behind the holed-mirror and axicon coupling scheme into a Fresnel cone.

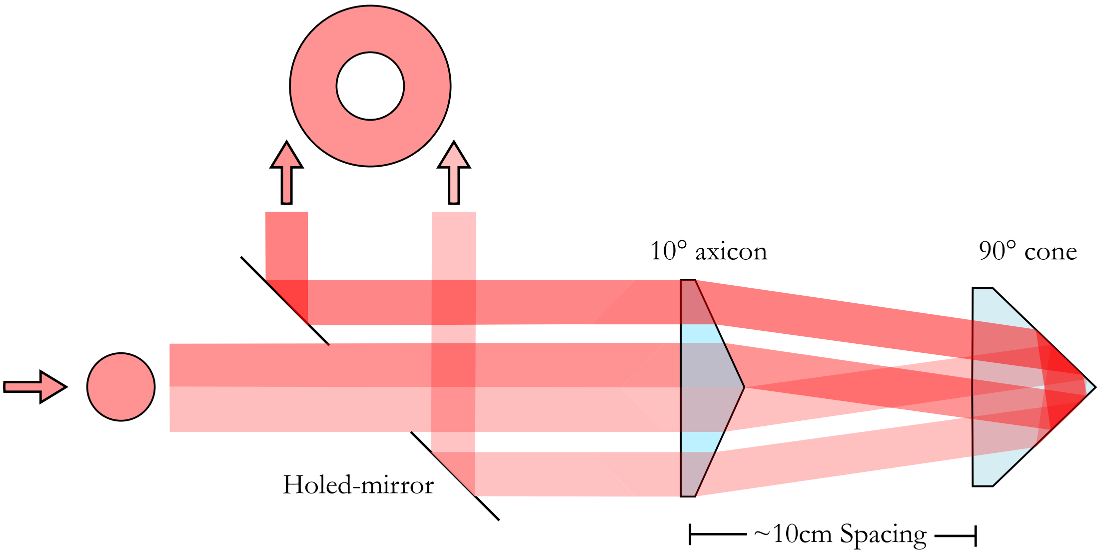

FIGURE 3.11: Sketch-diagram showing the idea of the holed-mirror and axicon coupling technique. Note that the angles are not drawn to scale.

Light is incident at the rear side of a mirror angled at 45°, through a central hole. Upon deflection by an axicon, the incident Gaussian beam becomes a diverging annulus with the peak intensity on the outside edge. This light is incident to a Fresnel cone, where although the angle of incidence is not the usual 45°, it is still above the critical angle for total internal reflection to occur. This difference in incidence angle at the Fresnel cone rear surface is small enough to result in a negligible phase-shift difference between s and p components. The distance between the axicon and cone is chosen such that the reflected beam passes in the opposite direction through the initial axicon before it has diverged to a radius greater than the physical axicon ($\sim$ 12.5 mm) and is deflected to propagate parallel to the optic axis (which turns out to be $\sim$ 10 cm for a 10° axicon). The annular beam is now at a diameter large enough to be reflected by the 45° mirror, avoiding the hole at the centre. In theory this should provide Fresnel cone coupling with 100% efficiency. The experimental setup for the axicon coupling and vector beam generation is shown below in Figure 3.12.

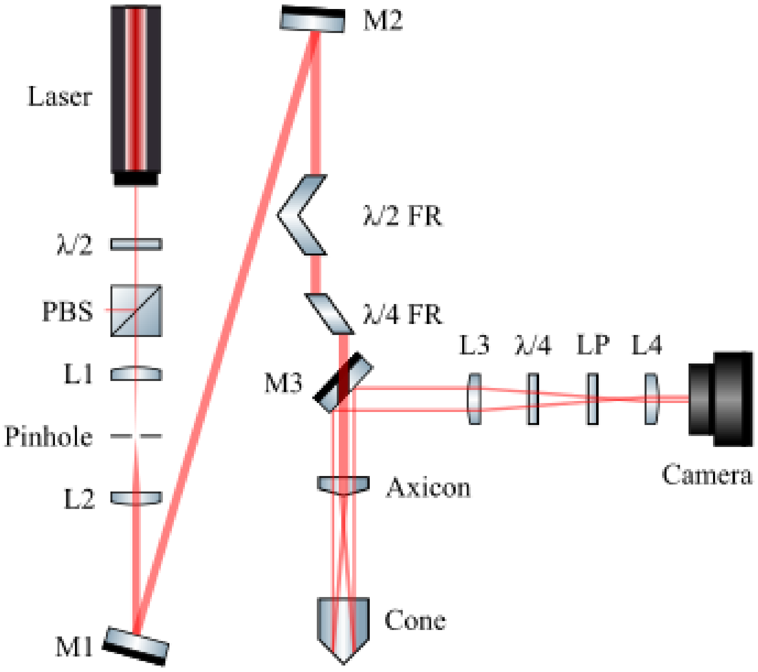

FIGURE 3.12: Diagram showing the experimental setup for the axicon-coupling experiment. The laser used was a helium-neon laser with a wavelength of 633 nm. $\lambda/4$ and $\lambda/2$ are quarter- and half-wave plates respectively, while $\lambda/4$ FR and $\lambda/2$ FR are quarter- and half-wave Fresnel rhombs, respectively. M1, M2 and M3 are mirrors, where M3 has a central hole for the beam to pass through. The pinhole used is a 50μm pinhole which was aligned using a 3-axis mount. PBS is a polarising beam-splitter. L1, L2, L3, L4 are lenses with focal lengths 50, 150, 175 and 50 mm, respectively.

In the experimental setup shown above, the light source is a 633 nm Helium-neon laser. the initial half-wave plate ($\lambda/2$) and polarising beam-splitter (PBS) are used to control the incident power and provide a horizontally polarised input. The two lenses (L1, $f = 50$ mm, and L2, $f = 150$ mm) and pinhole are used to both expand the beam and spatially filter any noise, allowing transmission of a clean Gaussian beam. Mirrors M1 and M2 are used to steer the beam for alignment. The following double and single Fresnel rhombs ($\lambda/2$ FR and $\lambda/4$ FR) are used to generate uniformly polarised input states to the Fresnel cone system. M3 is a mirror at 45° with a central hole. The axicon (10°) and Fresnel cone (3rd generation, H-BaK6) are positioned at a distance such that the output beam after the second pass through the axicon is aligned with the optical axis, as described previously. Lenses L3 ($f = 175$ mm) and L4 ($f = 50$ mm) are used to image the plane of the Fresnel cone surface to the camera (Thorlabs, DCC1645C). The quarter-wave plate ($\lambda/4$) and linear polariser (LP) are used to perform Stokes analysis for spatially resolved polarisation measurement with the camera, as described earlier in the chapter. An image of a prototype design for a compact version of the Fresnel cone-axicon coupling device is shown below in Figure 3.13.

FIGURE 3.13: Prototype compact version of the axicon coupling device.

To first test the efficiency of the technique, a mirror was placed at the position of the Fresnel cone for simplification of alignment during power measurement, and the power was recorded using a photodiode power sensor (Thorlabs, S121C) and power meter (Thorlabs, PM100D). The power was recorded at incremental positions in the axicon system in an attempt to locate potential losses - see Table 3.3 below.

Position	Power (mW)
Background	0.014
Prior to axicon	33.51
After axicon pass 1	32.76
After mirror (cone position)	32.06
After axicon pass 2	31.37
After M3 reflection	27.88

TABLE 3.3: Table showing power measurements at incremental positions through the axicon coupling scheme.

Considering the final and initial power readings, the experimental efficiency of the axicon coupling technique was found to be $\sim 83.2\%$. These losses can be attributed to the typical 4% losses at incidence upon the un-coated axicon and reflection by the non-ideal M3 mirror (lenses and waveplates in the system are for characterisation and not part of the coupling device). In addition to this, a non-ideal axicon tip (rounded) can cause undesirable diffraction losses - Brzobohaty et al. showed that spatial filtering in a Fourier plane could perhaps help to avoid this [100]. By using an axicon with anti-reflection coating and ideal mirrors for the wavelength range in use, this could also assist in achieving an efficiency closer to the theoretical 100%.

To investigate the intensity distribution of the annular beam generated by the axicon coupling, an intensity image was recorded on the camera and analysed (see below).

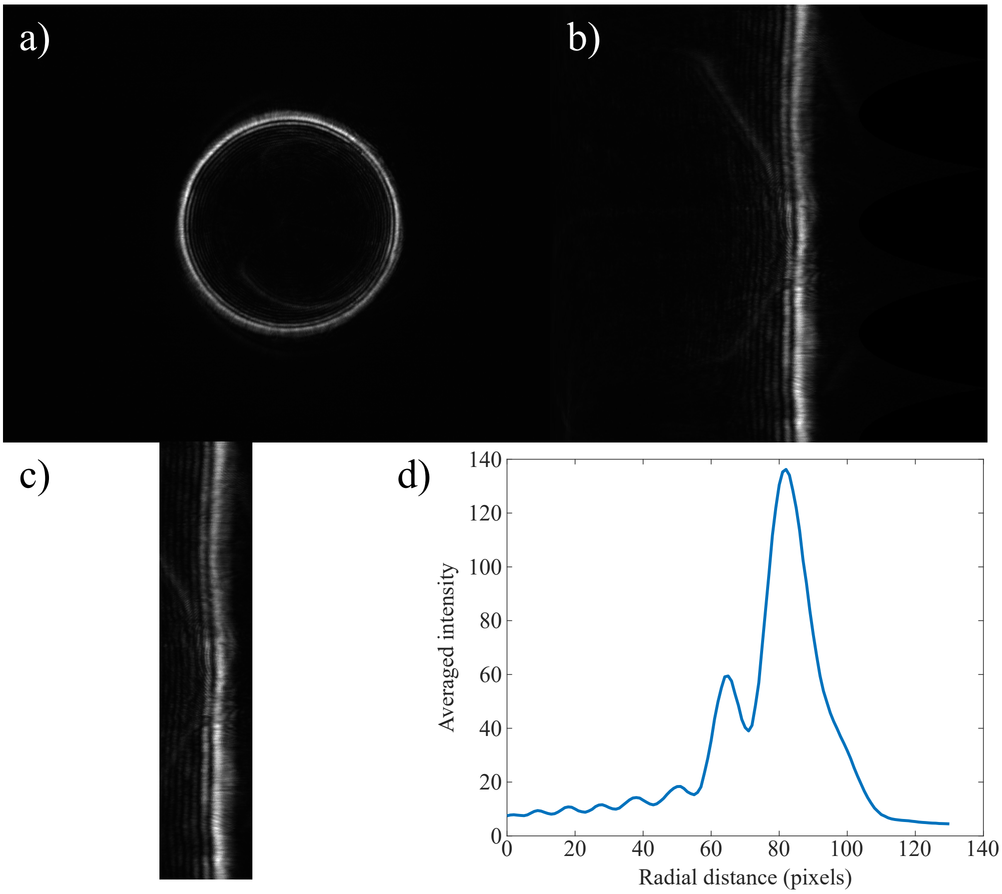

FIGURE 3.14: Investigation of intensity profile of generated annular beam by axicon device. a) camera image, b) coordinate transform from x-y to r-θ, c) region of interest selected and d) azimuthally averaged intensity line profile in radial direction.

Figure 3.14 a) shows the captured intensity image of the generated annular beam. Figure 3.14 b) shows this image after a coordinate transformation from a Cartesian x-y frame to a polar coordinate frame in r and θ. Figure 3.14 c) shows a region of interest selected, which is then averaged in the azimuthal direction (as the intensity should remain the same azimuthally, for a fixed radius), to provide an intensity line-profile in Figure 3.14 d). The peak intensity is towards the outer edge of the annular beam, as the incident Gaussian intensity profile has been inverted through deflection by the axicon. The inner rings observed can be attributed to the diverging rings of the generated Bessel beam [101], which have not yet propagated far enough to become negligible.

After investigating the efficiency of the coupling technique and the intensity distribution of the generated beams, the spatially resolved polarisation profile was measured - results are shown below in Figure 3.15 for generated azimuthal and radial polarisation.

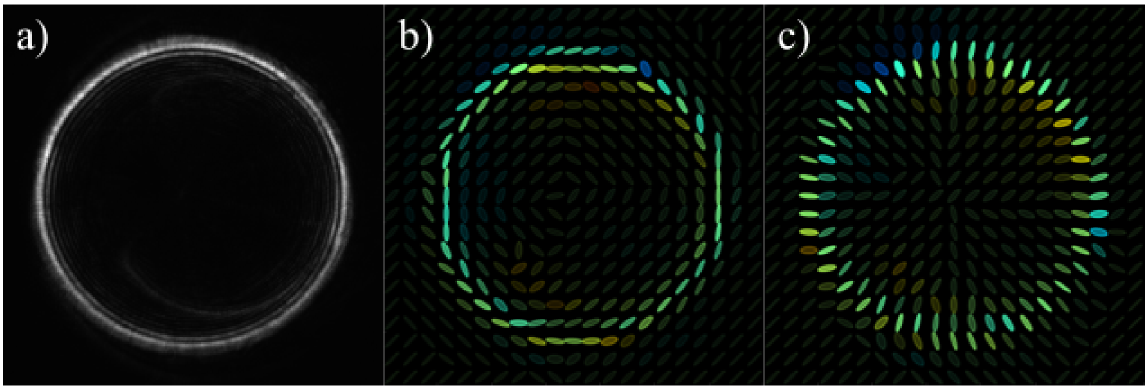

FIGURE 3.15: a) intensity image at camera plane, and spatially resolved Stokes measurement for b) azimuthal and c) radial polarisation.

To generate the desired vector beams, circularly polarised light is input to the system for back-reflection from a Fresnel cone, with the output afterwards operated on by a half-wave plate oriented at ±22.5° to generate either radial or azimuthally polarised light. Figure 3.15 a) shows the intensity profile at the camera plane for comparison, Figure 3.15 b) and c) show the spatially resolved Stokes measurements for azimuthal and radial polarisation, respectively. Unlike previous vector beams generated using the Fresnel cone, this coupling method results in an annular beam, which may be beneficial for applications where these beams are focussed using a high numerical aperture (NA) lens. This is because as will be explained in the next chapter, interesting effects are found upon high NA focussing[5], and the peak intensity of the annular beam is positioned to benefit more from the high NA focussing than a typical Gaussian intensity profile.

3.5 Conclusions

In this chapter I have discussed popular methods for vector beam generation. I have shown that a simple setup using a solid glass cone can allow broadband generation of interesting vector vortex beams, such as radial and azimuthal polarisation. This is largely possible due to the ability to manufacture glass cones with the required refractive index to provide a total phase-shift of $\pi/2$ upon two total internal reflections.

---

[5] Here I consider a high NA to be an NA above ~ 0.7.

The second part of this chapter contains results I have obtained during my PhD, based on Fresnel cones. Upon obtaining higher quality Fresnel cones, I have shown higher fidelity results for the vector beams generated using the Fresnel cone than was previously achieved (see Figure 3.9). I have also shown the development of a new coupling technique into a Fresnel cone, based on the use of a holed-mirror and axicon subsection 3.4.1. I have shown that this technique allows theoretically 100% and experimentally $\sim$ 83% efficiency. A manuscript is currently in preparation for submission detailing the results of this coupling technique. As discussed, due to the annular beam generated from this technique benefits may be found in high numerical aperture focussing of vector beams.

Chapter 4

Strong focussing and practical considerations

4.1 Introduction

So far, I have shown that there is an increased interest in the structuring of not only the scalar properties of light (intensity and phase), but more recently of its vectorial polarisation property. Applications are suggested in a range of fields, for example, from laser machining [53, 102] to precision particle sensing [103]. For a review of this area see ref. [25]. In this chapter, the application of polarisation-structured beams in a strong focussing system is the subject of interest, where polarisation structuring allows focal spots smaller than those formed by conventional beams (uniformly polarised beams) [49–51]. This has the potential to enhance imaging resolution in scanning microscopy techniques.

The development of the optical microscope began in the 17th century when Antoni van Leeuwenhoek first described biological observations using the single-lens microscope [104]. Since then, there have been continual technological advancements in the design of optical microscopes to reduce aberrations, increase magnification and improve the quality of images. An arbitrary high magnification however, does not necessarily result in the ability to see fine detail and even with modern advanced manufacturing techniques, optical resolution is fundamentally limited by the diffractive nature of light. This diffraction limit generally prevents the optical imaging system to discriminate between two point objects positioned less than around half the wavelength of the illumination light used [6].

It is necessary for discussion throughout this chapter to introduce the light collecting power for a microscope objective, known as the numerical aperture (NA), which can be defined as

$$\mathrm{NA} = n\ \sin(\theta), \tag{4.1}$$

where n is the refractive index of the imaging medium and θ is the collection half-angle of the cone of light entering the lens. To obtain a higher NA, a stronger lens and thus larger focussing angle, or a higher refractive index imaging medium can be used, such as certain oils ($n \sim 1.5$) in an oil-immersion lens rather than air ($n \sim 1.0$). Additionally it will be useful to state here the common criterion for the conventional diffraction limit, proposed by Ernst Abbe in 1873[1] and expressed as

$$d = \frac{\lambda}{2\ \mathrm{NA}}, \tag{4.2}$$

where d is the radius of the spot that the light in an optical system converges to and λ is the wavelength of illumination light used. From Equation 4.2, in addition to increasing the NA to see smaller details we can also use shorter wavelength light, however, shorter wavelengths may damage certain biological samples. Considering light of ~ 600 nm and a high numerical aperture of ~ 1.5, we find that the Abbe diffraction limit is ~ 200 nm in the lateral direction. Systems limited by diffraction are therefore not able to resolve sub-cellular structures, such as organelles, on the scale of tens of nanometers [105].

Over the last two decades so-called super-resolution techniques have emerged, which essentially bypass the conventional diffraction limit to obtain higher resolution. The various super-resolution techniques can be generally be placed in two groups: deterministic techniques including stimulated emission-depletion (StED) [40, 106, 107] and ground state depletion (GSD) [108–110], and stochastic techniques including photo-activated localisation microscopy (PALM) [111] and stochastic optical reconstruction microscopy (STORM) [112]. These techniques are able to achieve imaging resolution on the scale of tens of nanometers.

Super-resolution techniques are clearly impressive and exhibit clever ways to bypass Abbe's diffraction limit, rather than overcome it. This conventional diffraction limit however, assumes homogeneously polarised light and does not take into account the possibility of vector beams. As mentioned in chapter 1, it has been shown that polarisation has a significant effect in a strong focussing regime, where uniformly

---

[1] His famous equation is actually carved into his gravestone, in Jena, Germany.

polarised beams focus to elliptical spot shapes [49, 113], and structured beams are found to focus below what Equation 4.2 predicts for a conventional beam [50–52]. This is important as in a scanning microscope system, the imaging resolution is restricted by the size of the spot to which the light is focussed.

In this chapter, I will show that the polarisation structures produced by back-reflection from a Fresnel cone exhibit interesting effects when tightly focussed. Not only are these effects interesting, but for one particular case - that of the azimuthally polarised Fresnel cone beam - allows focal spots which are even more tightly confined than those of the conventional radially polarised beam [50–52]. I will show simulated results for the strong focussing of different Fresnel cone beams, based on the vector diffraction theory outlined in section 2.5, as well as experimental attempts to measure these. I will also discuss work done as part of an industry-led collaborative project to develop a prototype microscope module to provide broadband polarisation structuring. Theoretically I show that Fresnel cone beams can be beneficial for resolution enhancement in microscopy, however, experimental issues arose due to phase coherence proving detrimental for the practical realisation. I will discuss the practical implications encountered and describe the resulting experiments and analysis performed to characterise the surface quality of the Fresnel cones, using interferometry and Fourier analysis techniques. Though immediate practical use for resolution enhancement was not possible, this resulted in a thorough study of the practical effects of various parameter deviations.

My contributions to this work included expanding on an inherited strong-focussing simulation program to investigate focussing effects on Fresnel cone beams, building and testing the prototype microscope bolt-on module as part of an industry collaboration, setting up and performing the experiments, writing a Fourier analysis program for cone surface flatness measurements, analysing the data and co-writing a manuscript for publication [62], presented at Photonics Europe 2020.

4.2 Radially and azimuthally polarised light

Interest in beams of light with cylindrically-symmetric polarisation profiles rapidly increased upon discovery of the tight focal spots produced by a strongly focussed radially polarised beam [50–52]. It was shown theoretically [50, 51] and demonstrated experimentally [52] that a focal spot size of $\sim 0.16\lambda^2$ is achieved with a radially polarised beam, compared to $\sim 0.26\lambda^2$ for a homogeneously linearly polarised beam (close to the theoretical Abbe prediction for a homogeneously polarised beam discussed in section 4.1 of $(0.5\lambda)^2 = 0.25\lambda^2$). A qualitative understanding of why a radially polarised beam produces a smaller focal spot is discussed by Zhan [25] and considers a radiating dipole aligned along the optic axis at the focus of a lens. The oscillating dipole radiates outwards in the well known toroidal pattern which is captured by the lens in one direction. Intuitively, at the lens plane the polarisation pattern is radial and beyond the lens the light is collimated. If a second lens is positioned in a 4π setup (as depicted below in Figure 4.1), recovery of all the propagating light is possible.

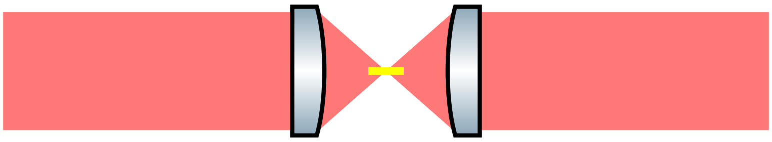

FIGURE 4.1: Simple diagram showing two high NA lenses in a 4π setup. The orientation of the discussed dipole analogy is also depicted in yellow.

Another intuitive consideration of the focussing effects of a high NA lens on a radially polarised beam are depicted by Wang et al. [114] and shown below in Figure 4.2.

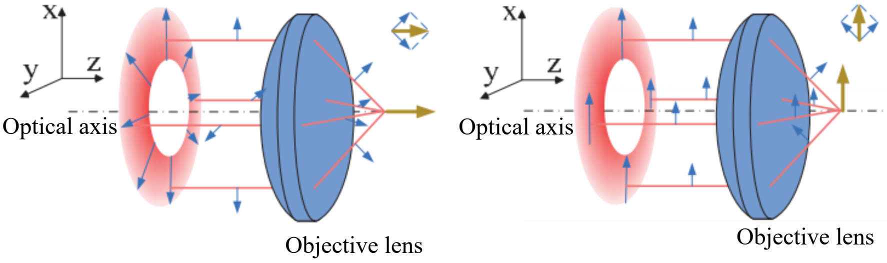

FIGURE 4.2: Diagram showing focusing properties of a radial polarisation (left) compared with a linearly polarised beam (right) (image adapted from [114]).

The left diagram in Figure 4.2 depicts that for the case of the radial polarised beam, as the k-vectors change direction upon strong focussing, the interference effects in the focal region result in a strong longitudinal (axial) electric field component at the focus. For the linearly polarised beam shown on the right of Figure 4.2, the resulting electric field at the focal point is asymmetric.

There almost always exists a small longitudinal component in the focal region of a high NA lens (except in the case for an azimuthally polarised input), however, for the radially polarised input the resulting longitudinal field component is stronger than the transverse component [53]. More generally, the radial component of the incident light contributes to both the radial and longitudinal field components, while an azimuthal component of the incident light contributes only to the azimuthal field component at the focus [25]. Furthermore, the magnitude of the longitudinal electric field component for a focussed radially polarised beam depends on the NA of the objective lens used - by fine tuning the NA it is possible to produce flat-top focal fields with a radially polarised input [115]. A simple way to achieve this could be to spatially restrict the diameter of the input beam to a high NA lens, resulting in a lower effective NA.

Given that the azimuthal polarisation component of the input beam contributes only to the azimuthal component in the focal region, when focussing an azimuthally polarised beam the resulting electric field is purely transverse at the focus (there is zero longitudinal component). Youngworth et al. [51] noted in 2000 that the intensity distribution of a strongly focussed azimuthally polarised beam is that of a ring. Ten years after this, Hao et al. [57] showed that an azimuthally polarised beam which also carries one unit of OAM actually focusses to a spot, rather than a ring, and that this spot is even smaller than that of the focussed conventional radially polarised beam. I note here that this finding is very interesting for work related to Fresnel cone beams, as this particular beam structure can be passively generated using the back-reflection from a Fresnel cone (as was discussed in chapter 3). More recently, there has been a considerable amount of research into the use of azimuthally polarised light for uses in StED microscopy [116–118]. For a short review of how these types of beams can be generated, please see section 3.2.

4.3 Tight focussing of Fresnel cone beams

To summarise some key points of the previous section - in the mid 2000s there was interest in radially polarised light as it was found to focus to a smaller spot than a uniformly circularly polarised beam (for a high NA). More recently, Hao et al. [57] found that an azimuthally polarised beam possessing OAM focusses even smaller still. In chapter 3 I showed that through back reflection from a Fresnel cone both azimuthally and radially polarised beams can be generated. In contrast to what I have called 'conventional' radially and azimuthally polarised beams, the Fresnel cone beams have a net OAM of $1\hbar$. In this section I will show and discuss simulated results for the focussing of Fresnel cone beams and the results of various aperturing of the incident beams at the pupil plane. The potential use of a Fresnel cone for broadband polarisation structuring, with benefits for microscopy resolution enhancement, resulted in the establishing of an industry-led collaboration project to develop a bolt-on microscopy module - this will also be detailed in this section.

4.3.1 Simulated strong focussing of vector beams

To investigate the resulting focal fields of strongly focussed Fresnel cone beams, a program was written using a combination of LabVIEW and MATLAB code, using the vector diffraction theory of Richards and Wolf [47] (this strong focussing theory is detailed in section 2.5). For the following simulated results, a wavelength of 850 nm was used as this is a typical wavelength used in two-photon microscopy techniques. For the right-handed circularly polarised beam, a purely right-handed polarised plane wave input is used. For the conventional radially polarised beam, a horizontally polarised plane wave is operated on by a Q-plate with a Q number of $Q = 0.5$. Finally, for the azimuthally polarised Fresnel cone beam, a right-handed circularly polarised plane wave is operated on by a Fresnel cone which imparts a total phase-shift between s and p components upon TIR of $\pi/4$, an ideal 45° mirror-reflection representing the reflection in the necessary non-polarising beam-splitter used for coupling to the Fresnel cone, and finally the action of a half-wave plate with fast-axis rotated by 22.5° from the horizontal position. See section 3.3 for a reminder on the generation of particular Fresnel cone beams such as this. For each case, the beam-width and objective lens diameter is 20 mm, and the initial beam has a Gaussian intensity profile.

Focal spot sizes for differently polarised input beams were investigated using the strong focussing simulation. Focal spot sizes for the three input beams described in the previous paragraph are shown in Figure 4.3 for increasing focussing angle (NA), confirming the previous findings of [50–52] that for a high NA objective lens, a radially polarised beam focusses to a spot size below that of a conventionally (circularly) polarised beam. I note here that for lower NAs, the radially polarised beam does not focus to a smaller spot - below a focussing angle of $\sim 67°$. Figure 4.3 also shows that an azimuthally polarised beam generated by a Fresnel cone (where the right-circular component of the beam possesses two units of OAM and the left-circular component has zero OAM) focusses to a spot size below that of both the conventional circular and radially polarised beams. Importantly, the azimuthally polarised beam does not require the high NA focussing lens to achieve a smaller spot than radial polarisation. This agrees with the findings of Hao et al. for an azimuthally polarised beam with different OAM components [57]. It can also be seen in Figure 4.3 that as the focussing angle increases, eventually the focal spot size for a radially polarised beam approaches that of the Fresnel cone azimuthally polarised beam.

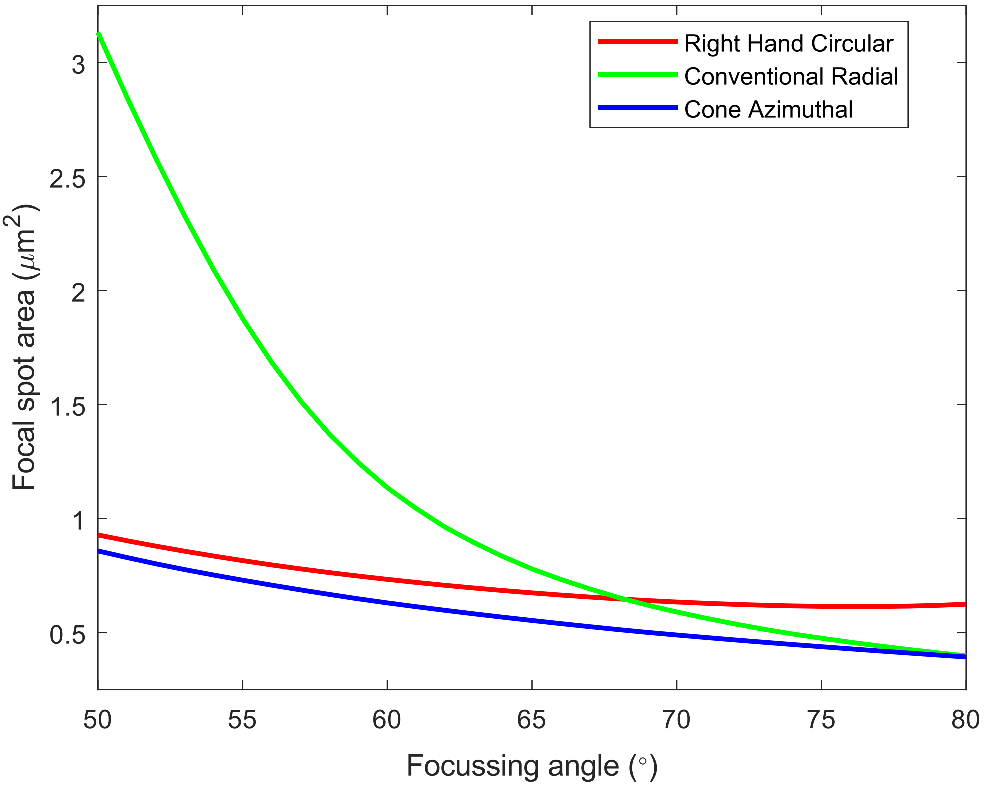

FIGURE 4.3: Simulated results showing a comparison of focal spot size for conventional circular and radially polarised beams and an azimuthally polarised Fresnel cone beam, for increasing focussing angle (where NA= $n \cdot \sin\theta$).

Figure 4.4 shows the 2D (transverse plane) normalised intensity profiles at the focal plane for the focussing of a right-handed circular, conventional radial and Fresnel cone azimuthally polarised beam, for a focussing angle of 75° (NA∼1). By summing the irradiance of the E_x and E_y fields, $|E_x|^2 + |E_y|^2$, the total transverse intensity is shown, as well as the total longitudinal intensity $|E_z|^2$. The total intensity is the sum of all three field components, $|E_x|^2 + |E_y|^2 + |E_z|^2$.

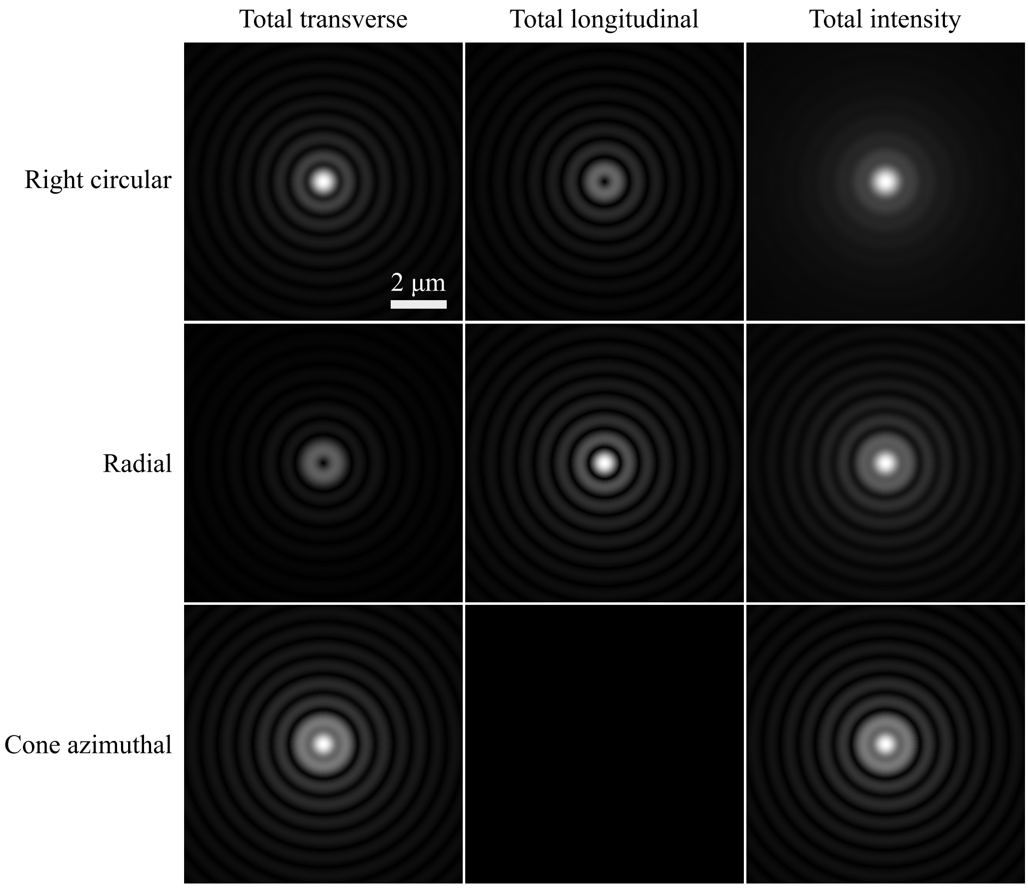

Figure 4.4: Normalised intensity profiles in the focal plane for three differently polarised input fields (Right-circular, radial and Fresnel cone azimuthal). The transverse, longitudinal and total intensity is shown.

As discussed, the results for the right-hand circular input light show only a small longitudinal field at the focus, the radially polarised beam shows a strong on-axis longitudinal field, while the focal intensity of the azimuthally polarised beam is purely transverse. As each of these focal spots are symmetric in shape, a line profile in any direction is sufficient to further investigate the intensity distribution. To compare the focal spot size, Figure 4.5 below shows line profiles of each case in both the x- and y-direction (as a check for symmetry), for a focussing angle of 75°. The full-width at half maximum (FWHM) is also shown, as quantification of the focal spot sizes.

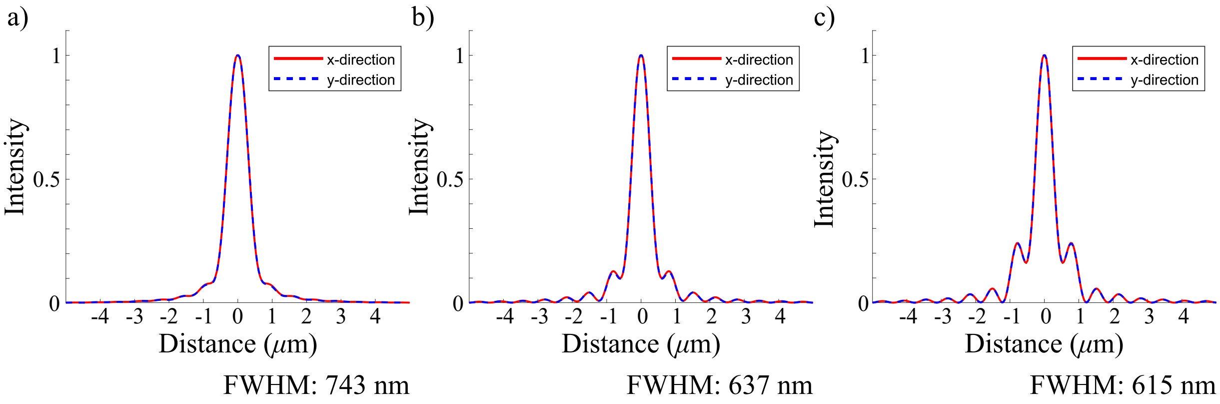

Figure 4.5: Overlapped line profiles of the normalised focal spot intensity profile at the focal plane in both the x- (solid red) and y-directions (dashed blue), for a) circularly polarised, b) radially polarised and c) cone-azimuthally polarised input beams.

Figure 4.5 supports the suggestion that the focal spots are symmetric in shape, and further analysis will assume this is the case for radial, azimuthal and circularly polarised input beams. It is also noted that the focal spot resulting from the cone-azimuthally polarised beam exhibits slightly more pronounced sidelobes when compared to the other cases.

To further investigate the behaviour of the focal spot size, which clearly has a dependence on the NA of the focussing lens, the focal spot size was simulated with an increasing centre stop in the lens pupil plane. This means that for an increasing centre stop size, the contribution of the input beam from the lower NA region of the focussing lens (closer to the centre) is increasingly reduced. Figure 4.6 below shows the focal spot size for the same three input beams investigated in this section, for a centre stop increasing in radius from 0 to 8 mm (as before the objective lens diameter is 20 mm), for a focussing angle of 75°.

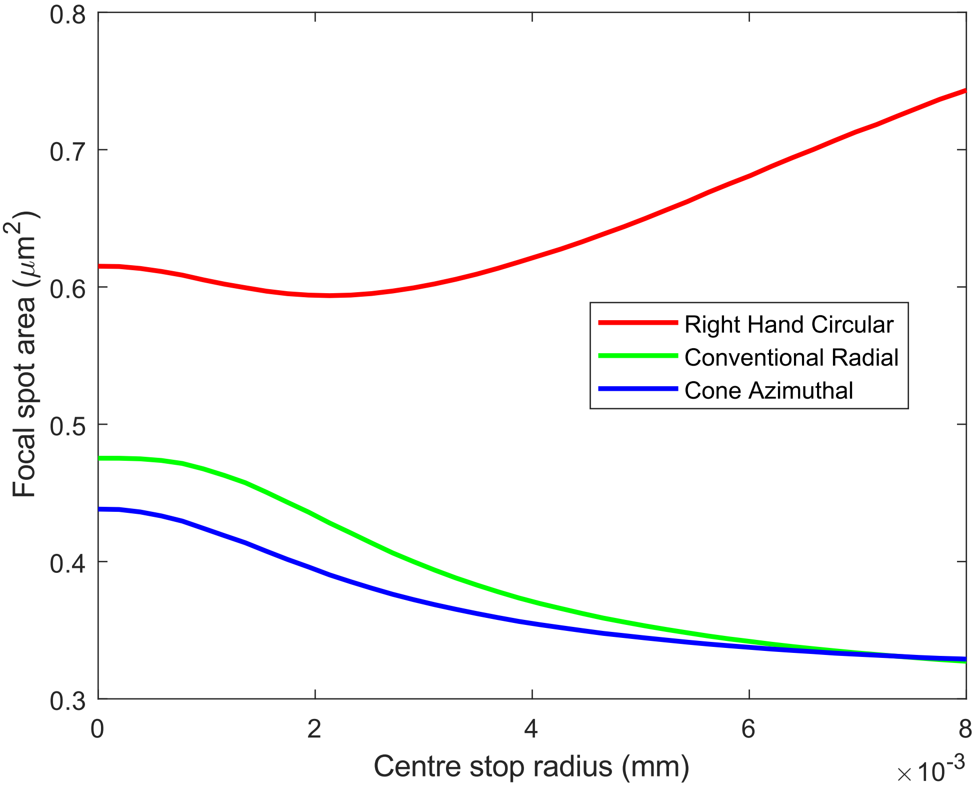

Figure 4.6: Simulated results showing a comparison of focal spot size for conventional circular and radially polarised beams and an azimuthally polarised Fresnel cone beam, for increasing centre stop radius. This is for a focussing angle of 75° (an NA of ~ 1).

The results shown in Figure 4.6 show that similarly to the case for increasing focussing angle (NA) on the focal spot, the focal spot size for the radially polarised input beam gradually approaches that of the Fresnel cone azimuthally polarised input, for increasing centre stop size. The results in Figure 4.6 also show that when considering only the azimuthally polarised input, a centre stop still offers an enhancement to the focal spot size and is not only a mechanism by which the radially polarised input produces a spot size increasingly close in size to that produced by the azimuthal case.

So far the radially polarised beam produced by the Fresnel cone has not been discussed. This beam was initially disregarded for further investigation as the strong focussing of this beam actually results in a larger focal spot size than the conventional circularly polarised beams, however, a brief study was carried out. Interestingly for this beam a relatively strong donut-shaped longitudinal field component is generated in the focal region of a high-NA lens[2] (as shown below in Figure 4.7). Furthermore, it was noticed that the phase of this field in the longitudinal direction intriguingly varies azimuthally twice from 0-2π, in some ways akin to an OAM, with a topological charge of two[3], as can be seen in Figure 4.7d). This will be investigated further in the context of geometric phase in future work at the University of Glasgow.

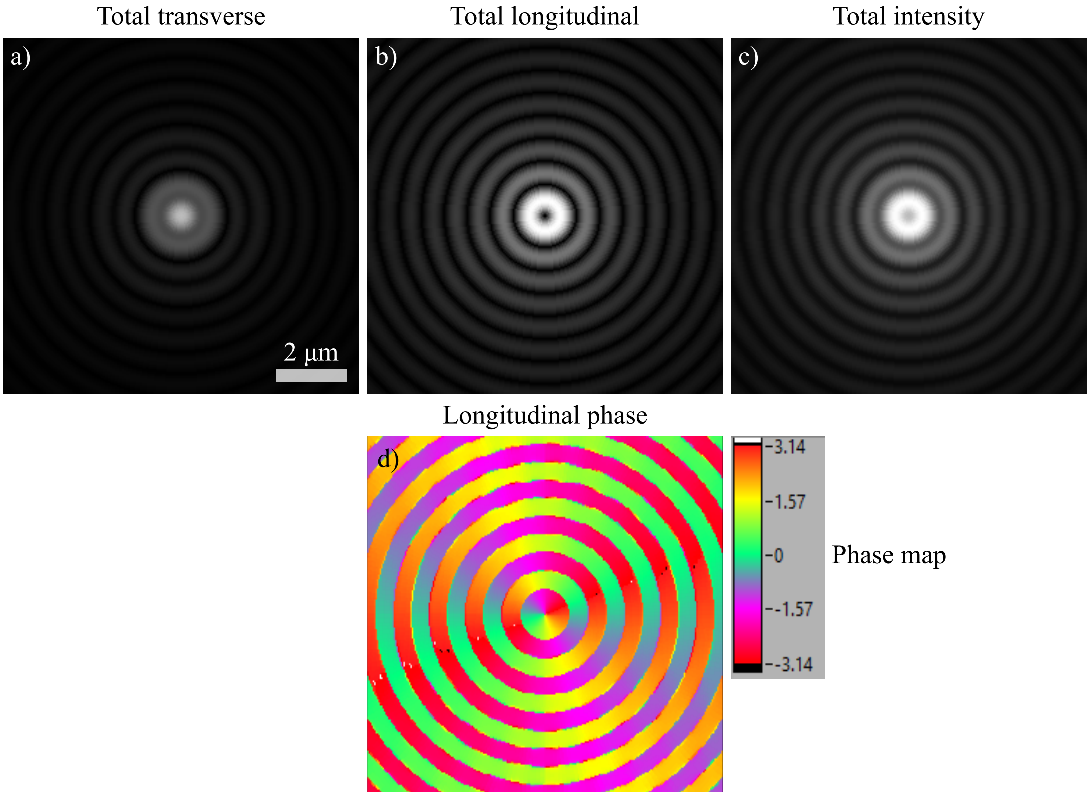

FIGURE 4.7: Simulated results showing the normalised focal spot intensities for the a) transverse, b) longitudinal and c) total planes, and d) shows a phase map for the longitudinal electric field component.

4.3.2 Industry collaboration - add-on microscope module

In an effort to exploit the findings of the Fresnel cone beam tight focussing simulation, an industry-led collaboration was formed, with an aim of developing a low-cost add-on microscope module to provide broadband polarisation structuring for existing microscopes. The collaboration was between the University of Glasgow, the Beatson Institute for Cancer Research, and companies Elliot Scientific and G&H. I

---

[2] NA~ 1.

[3] This comparison is purely a statement of similarity and not a claim that it also necessarily possesses the physical properties of OAM.

was tasked with constructing the prototype and initial testing at the University of Glasgow, G&H would provide the glass optics with Elliot scientific delivering assistance on the optomechanics, and final testing would be carried out at the Beatson Institute.

In the previous section it was mentioned that even non-polarising beam-splitters introduce unwanted phase-shifts to light that is either transmitted or reflected by them. More broadly, many optical components can introduce these unwanted shifts to the incident polarisation state. This is detrimental in any application employing polarisation, for example, in a polarimeter it becomes more difficult to calibrate the system and accuracy is reduced. Another perhaps more common application where this occurs is in optical microscopy. In a commercial microscope system there are usually several passes and reflections through beam-splitters and mirrors of various types, each altering the polarisation state of the light. The phase-shifts introduced by the elements in a microscope system vary in size, however, the largest is usually caused by dichroic elements (often used in fluorescence microscopy). If attempting to use polarisation in a microscopy application, for example, to control the size and/or shape of the resulting focal spot, understanding and being able to compensate for these unwanted polarisation shifts is of great importance. Therefore, the first task in this project was to determine whether the desired azimuthal polarisation state can be directed to the back-aperture of a microscope's objective lens, after generation prior to entering the microscope body.

The polarisation shifts caused by a number of optical elements in a microscope system can be summarised by a single Mueller matrix representing the entire system. It was conjectured that by experimentally determining this Mueller matrix, it would then possible to pre-compensate for this by adjusting the state of the input light accordingly. The instructions for determining a system's Mueller matrix were given in subsection 2.3.4. Through knowledge of a system's Mueller matrix, the two angles of rotation for a quarter- and half-wave plate can be calculated in order to pre-compensate the incident polarisation state. This way, the previously detrimental polarisation shifts caused in the microscope system actually correct the polarisation to the desired state at the microscope objective's back aperture, similarly to what was achieved by Chou et al. for uniformly polarised light [119]. The setup used to each generate, pre-compensate and measure the spatially resolved polarisation structures from a Fresnel cone, through a microscope system is shown in Figure 4.8.

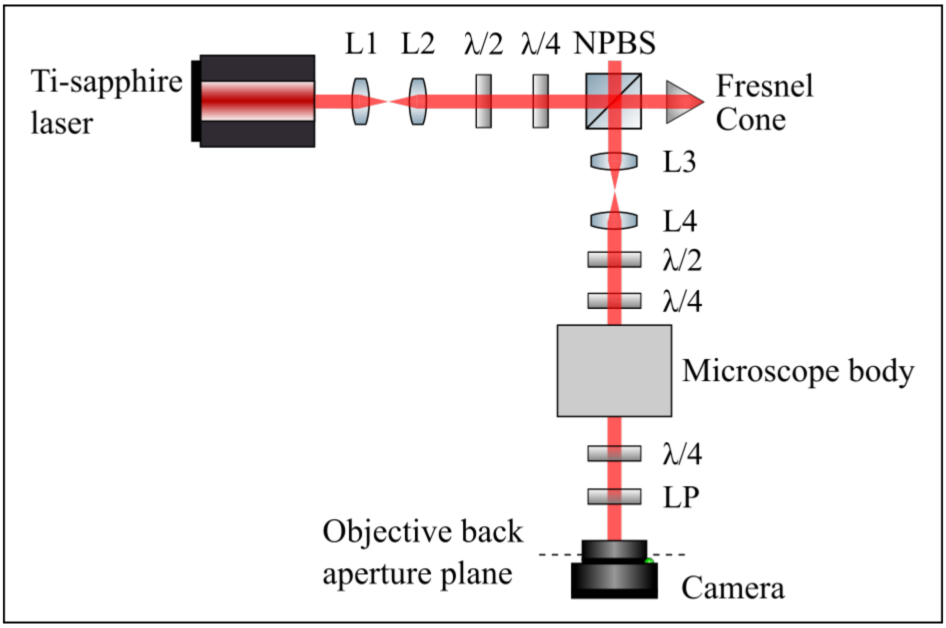

FIGURE 4.8: The experimental setup for generating, pre-compensating and measuring structured polarisation beams from a Fresnel cone, through a microscope system. L1, L2, L3, L4 are lenses, $\lambda/2$ and $\lambda/4$ are half- and quarter-wave plates respectively (for use at 850 nm). NPBS is a 50:50 non-polarising beam-splitter and LP is a linear polariser. The microscope body consists of mirrors, lenses and dichroic beam-splitters.

A single Mueller matrix was measured, representing the microscope system as a whole. An ideal theoretical Mueller matrix for the effects of the microscope system would be the identity matrix, having no overall effect on the incident polarisation state, however, the measured Mueller matrix for the system was found to be

$$\begin{bmatrix} 1 & 0 & 0 & 0 \\ 0.0026 & 0.93 & 0.16 & 0.16 \\ 0.024 & -0.063 & -0.85 & 0.35 \\ 0.033 & 0.087 & 0.31 & 0.73 \end{bmatrix}. \tag{4.3}$$

The minus sign of the third diagonal components essentially flips diagonal and anti-diagonal polarisation states. Using the pre-compensation method described above (and presented in [62]), azimuthally polarised light was detected using spatially resolved Stokes measurement at the plane in the microscope where the back aperture of the objective lens would be positioned. The resulting azimuthal polarisation state is shown below in Figure 4.9. In this case the beam over-fills the camera due to the beam-expanding telescope inside the microscope body, included to ensure the back-aperture of the objective lens is filled.

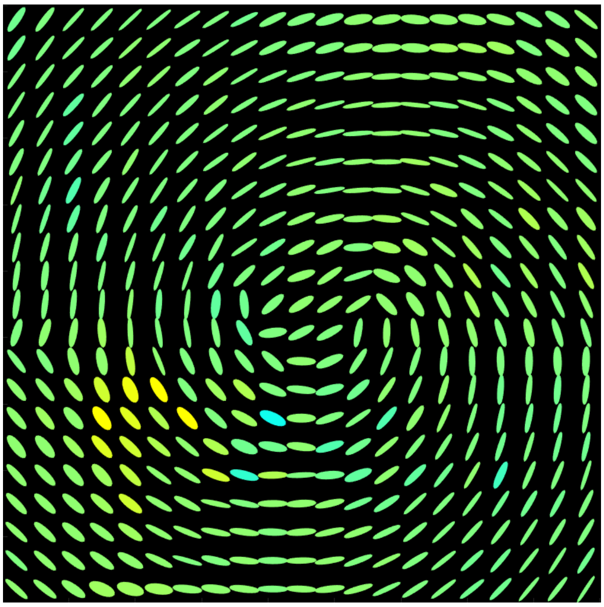

FIGURE 4.9: Spatially resolved Stokes measurement of beam at the plane of the objective lens' back aperture, after pre-compensation using rotations of a half- and quarter-wave plate on the incident light.

Once it was deemed that the required polarisation state could be measured at the back-aperture of the microscope's objective lens, the next task was to enhance the efficiency of the coupling into the Fresnel cone. As discussed in section 3.4, the most straightforward setup for coupling light into a Fresnel cone involves a 50:50 non-polarising beam-splitter, however, one result of this is that the maximum efficiency is limited to 25% (as there are two passes through the beam-splitter before detection). A frequency-based coupling method could also be used instead of a 50:50 beam-splitter, where for example, the incident beam into the cone is wavelength converted before incidence on the Fresnel cone, which is then coupled out using a dichroic mirror. In reality however, wavelength conversion is largely inefficient.

For high-efficiency coupling, complex geometry beam-splitters offer the most reasonable approach. In subsection 3.4.1 I showed an alternate method for coupling light into a Fresnel cone, using an axicon and mirror. We demonstrated an efficiency of $\sim 90\%$ and the successful generation of radial and azimuthally polarised light, however, the resulting intensity profile is in the form of a ring (for a Gaussian input beam) - this may not always be desirable. Alternately, another complex geometry beam-splitter approach has been previously suggested, using an arrangement of prisms with two Fresnel cones (see [46] supplementary material). A modification of this approach was chosen for use in the microscope bolt-on module device, where the original schematic is shown in Figure 4.10 ([46] supplementary material).

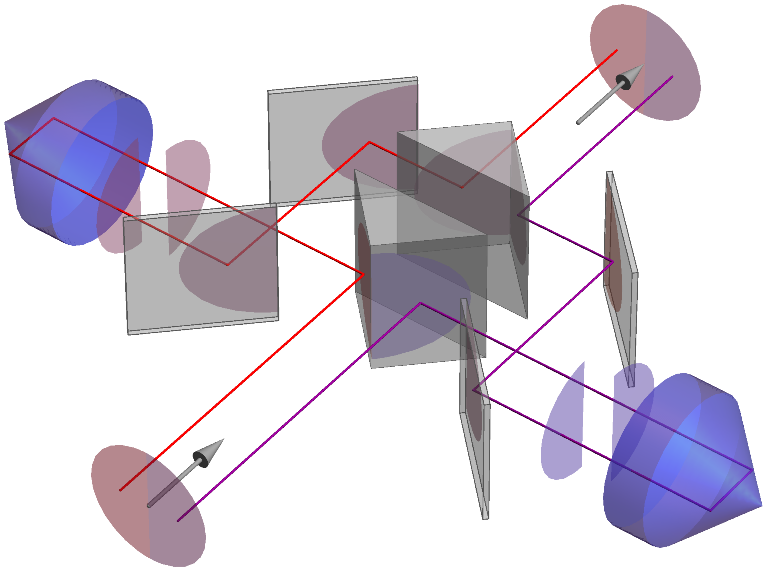

Figure 4.10: Complex geometry beam-splitter design for high-efficiency Fresnel cone beam generation.

Figure 4.10 shows the incident beam is split into two halves, which each independently reflects from co-aligned Fresnel cones, before being recombined using further reflections. This theoretically allows 100% efficiency, as well as broadband operation due to the achromatic nature of the system (as the reflections are TIR using prisms). After further development, a patent was secured for the dual cone beam-splitter device [120] and a prototype was build using a 3D printed housing to secure the prisms in place, adding further stability. Using an additional prism in the form of a single Fresnel rhomb at the input side, the device can be constructed so that the output beam is co-linear with the input - an added benefit of this is that only diagonally polarised incident light is required as the initial Fresnel rhomb generates the required circularly polarised light for azimuthal polarisation generation by the Fresnel cone. A photograph of the prototype is shown below in Figure 4.11.

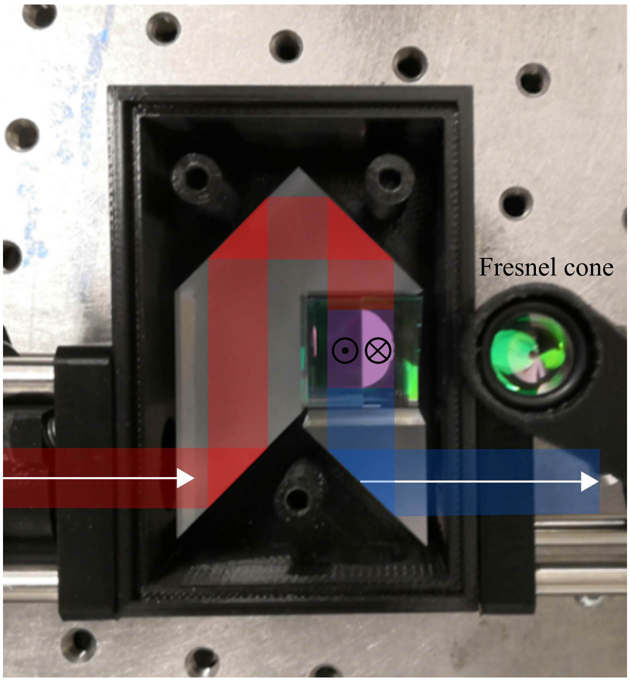

FIGURE 4.11: Prototype coupling device showing bonded prisms housed in 3D printed unit (the device is patented and so a detailed description could not be included with this thesis). Red path indicates input light, which is split in two in the purple region where one beam is directed upwards to one Fresnel cone and the other half is directed downwards to a second Fresnel cone. The blue path is shows the output beam.

In Figure 4.11 the red path represents the input beam, which first undergoes two total internal reflections at the angle required to obtain a total $\pi/2$ phase-shift between s and p polarisation components - thus producing circularly polarised light from diagonally polarised incident light. The combination of the two following reflections firstly results in no overall change to the circular polarisation state, and secondly, splits the beam into two halves (purple path region), each of which is directed to co-aligned Fresnel cones positioned above and below the device. These two beam halves are then recombined and leave the device through a final reflection, shown by the blue path. This final reflection acts similarly to the reflection encountered when using a the standard 50:50 beam-splitter coupling method, and forms part of the generation of azimuthal (or radial) polarisation. A further double Fresnel rhomb (not pictured) is used to rotate the polarisation by the required amount to produce the azimuthal state, as discussed in section 3.4.

It was anticipated that difficulties with this device may arise when attempting to recombine the two beam-halves, due to diffraction of the individual halves and the mechanical precision of available mounts. Figure 4.12 below shows the spatially resolved polarisation measurement for states generated using the dual cone-based polariser device, demonstrating both radial and azimuthal polarisation generation. Though there are visible issues with the polarisation state at the centre of the beam, these spatially resolved Stokes measurements are comparable with those generated using the standard 50:50 beam-splitter coupling method (see section 3.4).

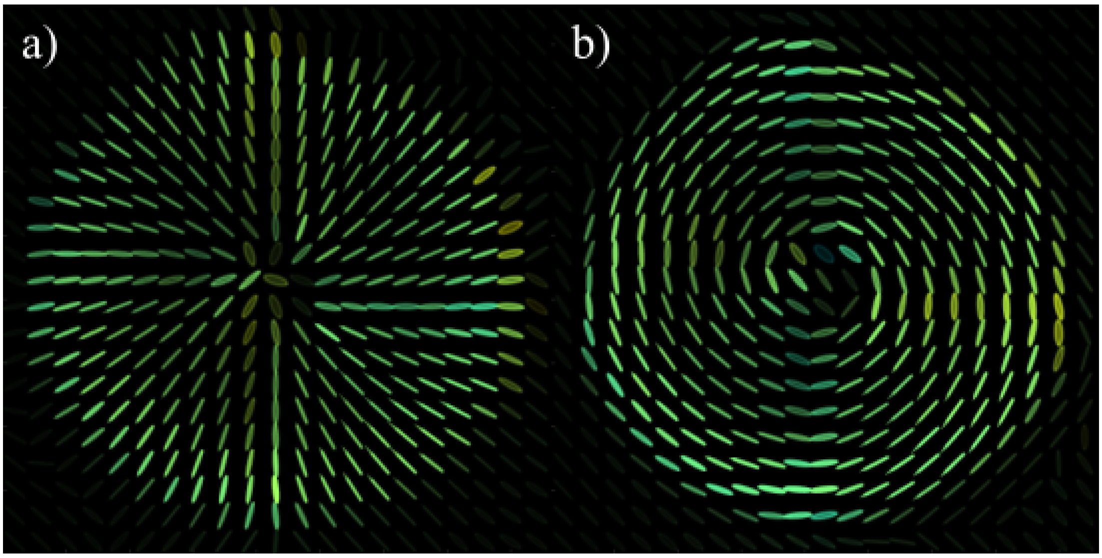

Figure 4.12: Spatially resolved polarisation measurement showing both a) radial and b) azimuthal polarisation states generated using the dual cone-based polariser device.

Although azimuthally polarised light was measured in the correct plane of the microscope, the recombination of two beam halves was later found to result in detrimental phase coherence effects and focussing issues. As the consequences of the strong focussing of the Fresnel cone beam relies on not only the polarisation state, but also the net-one unit of OAM, it was postulated that the precise positioning of the two Fresnel cones in the dual cone-based polariser device was critical to obtain the correct global phase of the final beam. Simulations were performed to obtain focal spot results given varying degrees of phase misalignment of the two beam halves, imitating misalignment of the Fresnel cones, with results shown below in Figure 4.13.

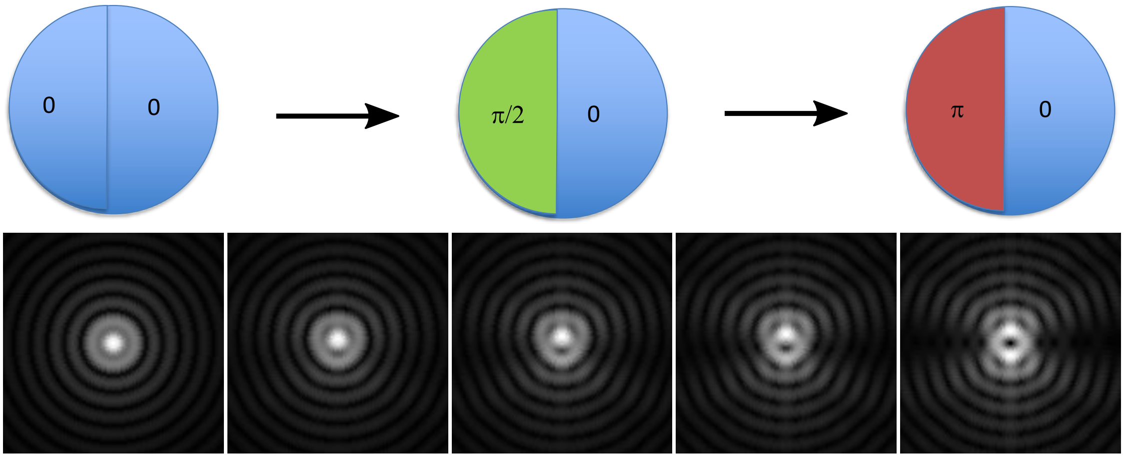

FIGURE 4.13: From left to right, simulated increase in global phase-shift for half of the beam diameter to imitate misalignment of the dual cone-based device described in the text, and resulting focal spot for a focussing angle of ∼ 75°. Phase shift increases from zero to π for one semicircle.

As can be seen in Figure 4.13, a slight misalignment between the two Fresnel cones in the dual cone-based polariser device will likely result in a non-ideal focal spot shape - detrimental for any imaging capability of the intended microscope system. Using the 3D printed cone mounts in the prototype device, alignment of the two Fresnel cones with wavelength-scale precision is not currently possible.

4.4 Focal spots and imperfect cones

In an optical microscope, if the wavefront of a propagating beam is deformed (perhaps by less than ideal optical components) the resulting focal spot can deviate from the ideal theoretical spot. Considering ray optics, a ray that is not propagating parallel to the optic axis is not focussed to the focal point of a lens, and so a beam with a distorted phase-front may focus to a non-uniform distribution in the focal region. For example, a convergent/divergent ray will focus before/after the focal point of a lens (or sometimes continue diverging for large divergence angles). In extreme cases where optical components have significant surface roughness and are not simply slightly misshaped, the phase is essentially randomised, resulting in a speckle phase that cannot be focussed to a spot at all.

In this section, I show that unfortunately, even weakly focussed beams from the current Fresnel cones resulted in distorted focal spots. I then show results from an experiment performed to look into the surface form of a Fresnel cone by interferometrically investigating the phase of the cone beams, accompanied by simulations to imitate effects of the surface roughness and non-uniform cone shape on the focussing properties.

4.4.1 Low NA focussing result

As an initial test of the Fresnel cone beam focussing, a simple experiment was set up to view the resulting focal spot of a relatively weakly focussed beam. The experimental setup is shown below in Figure 4.14. For these initial tests, 2nd generation cones were selected as 1st generation were already assumed to have too poor surface quality from previous visual inspections, and the 3rd generation cones had not yet been manufactured.

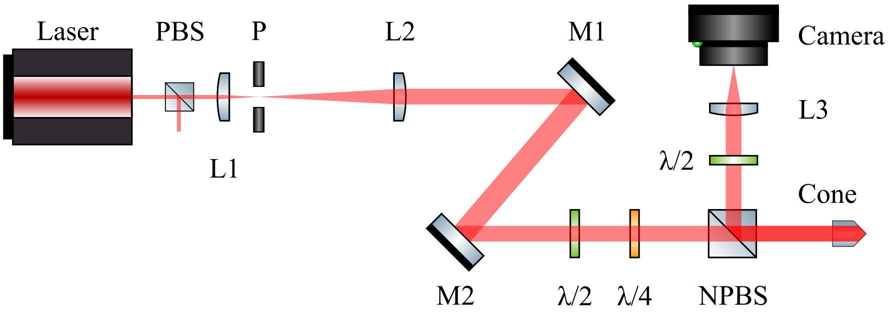

FIGURE 4.14: Experimental setup diagram for weak focussing measurement. PBS is a polarising beam-splitter, L1, L2, L3 are lenses 50 mm, 200 mm and 175 mm focal lengths respectively, M1 and M2 are mirrors, $\lambda/2$ and $\lambda/4$ are half- and quarter-wave plates respectively, NPBS is a 50:50 non-polarising beam-splitter and P is a 10 μm pinhole.

A 633 nm Helium-Neon laser was used as the light source. In the diagram above the initial PBS is used to provide initially horizontally polarised light. The following telescope and pinhole function as both a beam expander and spatial filter to ensure a ‘clean’ Gaussian beam, of a diameter sufficient for filling the front cone aperture. Mirrors M1 and M2 are used to steer the beam assisting alignment. The two waveplates (chosen for use at 633 nm) allow control of the incident polarisation state to the Fresnel cone, for generating radial and azimuthal polarisation states (using the second half-wave plate in the setup to rotate between the two states). The non-polarising beam-splitter (NPBS) is used to couple the light in and out of the Fresnel cone, as described in section 3.4. L3 is a 175 mm focal length lens, used to focus the beam onto a camera sensor for visualising the focal spot shape. The camera is a Thorlabs CMOS DCC1545M with 1280 × 1024 pixels and a pixel size of 3.6 μm^2. The resulting image of the focal spot is shown below in Figure 4.15 for azimuthally polarised light.

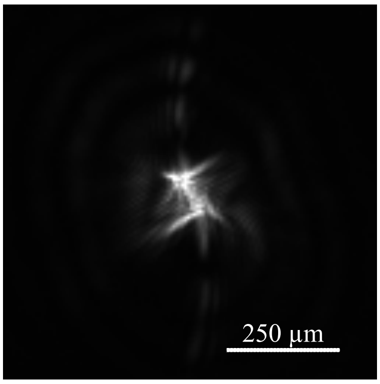

FIGURE 4.15: Camera image of the focal spot intensity profile from Fresnel cone beam for low NA focussing.

The non-uniform intensity distribution in the focal plane shown above for the weak focussing of a Fresnel cone beam suggests that there are issues with the quality of the Fresnel cone used. It was postulated that this was likely due to either non-uniform conical shape, non-90° cone apex angle, surface roughness or a combination of these issues. The spatial profile of the HeNe light source was not considered to be the reason as this was spatially filtered with a pinhole in the optical setup. To begin the investigation into this, simulations were performed to visualise the resulting focal spot for different distortions of the global phase, imitating surface roughness and non-uniform cone shape on the generated beam. For these simulations it is assumed any change to the polarisation is negligible and the angle of incidence at the rear surface is always above that needed for TIR to occur (and so amplitude is unaffected).

To investigate varying degrees of surface roughness, a randomised phase offset is added to the simulated beam prior to focussing (NA$\sim$ 1). Results are shown below in Figure 4.16 for randomised phase offsets of $\pm\lambda/8$, $\pm\lambda/4$ and $\pm\lambda/2$ with resulting focal intensity profiles.

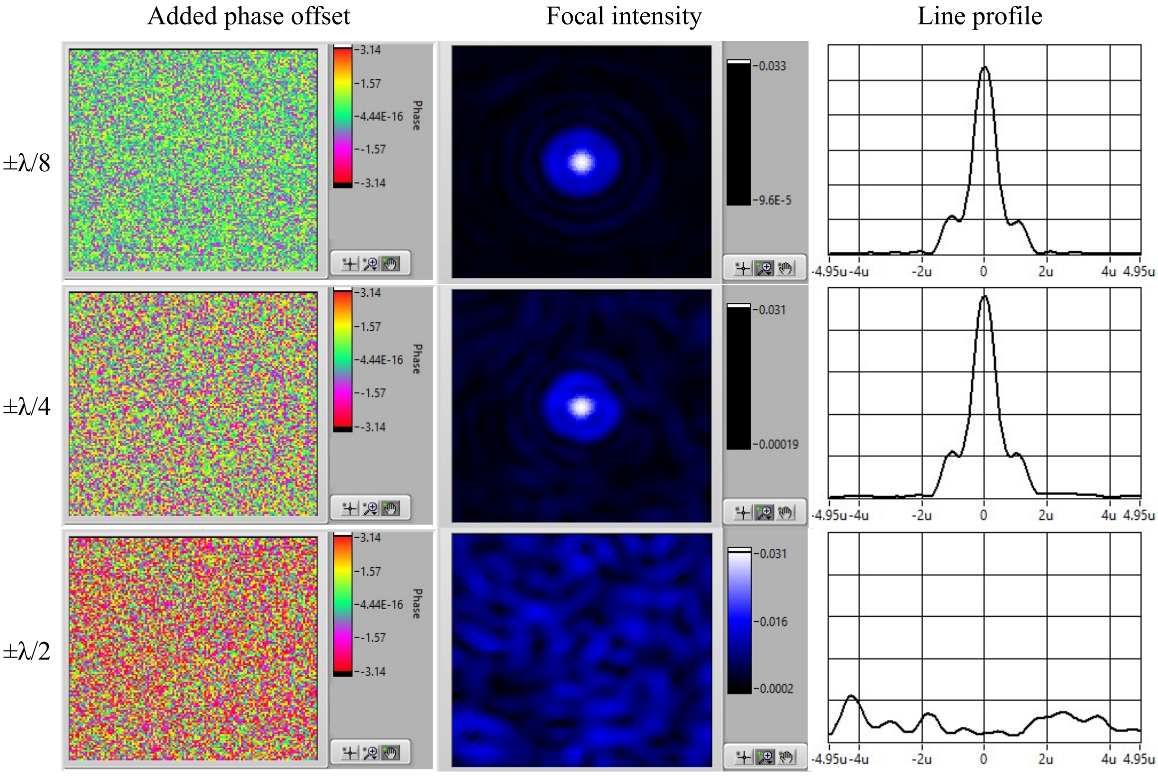

FIGURE 4.16: Simulation showing the effects on focal intensity for increased phase offset, imitating surface roughness.

The figure above shows the focal intensity distribution when three different maximum amounts of randomised phase offset are added to the global phase of a strongly focussed cone beam. For the first two rows, the focal spot remains arguably robust to the simulated surface roughness, while the third row shows the complete loss of focal spot. In the final case with a randomised phase of $\pm\lambda/2$ the phase is completely randomised as speckle. This simulation was carried out for continuously increasing phase offset, for each the circularly polarised beam, conventional radially polarised and azimuthal Fresnel cone beam, to compare robustness of the spot size (FWHM) to simulated surface roughness (shown below).

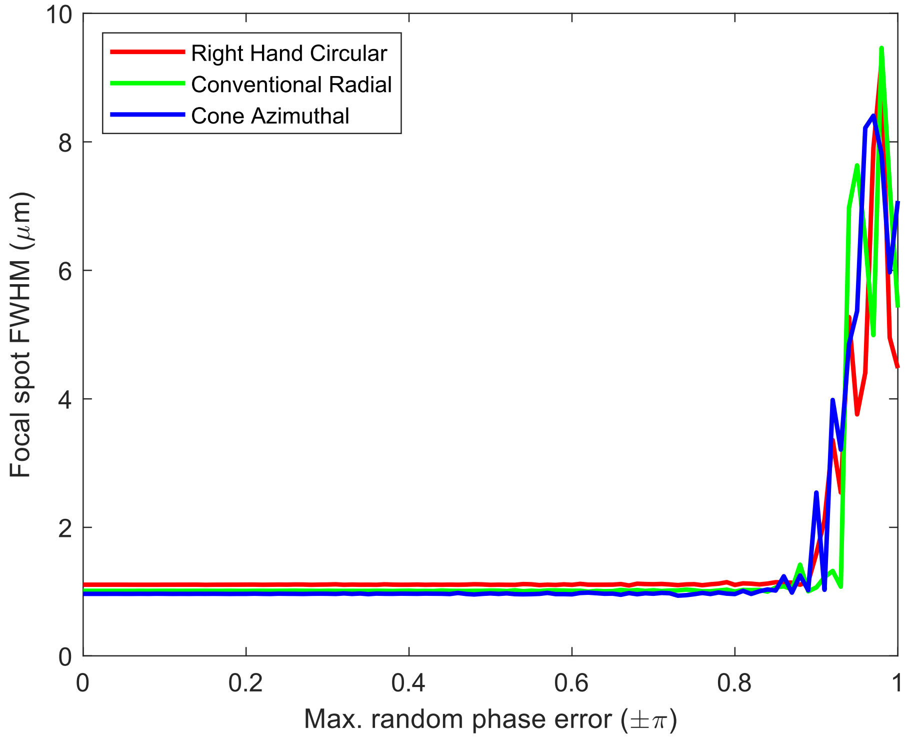

Figure 4.17: Focal spot FWHM for strongly focussed circular (red), radial (green) and Fresnel cone azimuthal (blue) polarisation, for increasing randomised phase offset to simulate surface roughness. Note this is an average of three randomised phase realisations.

The results above in Figure 4.17 show that the FWHM of the focal spot for the three focussed beams is fairly equally robust to simulated surface roughness, until an offset of $\sim \pm 0.9\lambda/2$, at which point there is an abrupt loss of focal spot. Arguably the radial beam produces a spot that remains given slightly more surface roughness than the other cases, but further simulation is required to confirm this.

Given that the focal spot shape is fairly robust to simulated surface roughness until a certain amount of roughness is encountered (at which point the light no longer focusses to a spot at all), it is likely not the main cause of the non-uniformity of the measured cone beam focal spot. To further investigate this, the strong focussing program was used to simulate the effects on the focal spot for a symmetrically warped conical form. This was achieved by adding an azimuthally varying sinusoidal phase to the cone beam prior to focussing, with a period of 2 (4) to imitate a cone form warped in 1 (2) directions. The results are shown below in Figure 4.18.

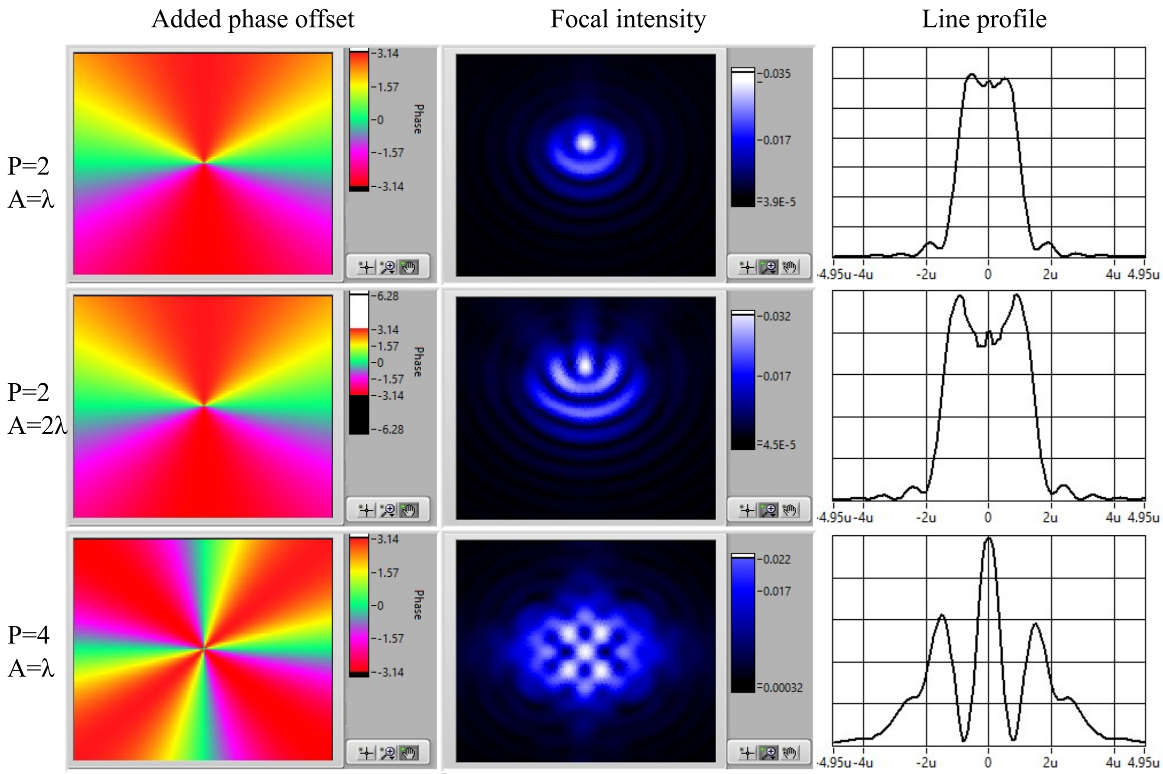

FIGURE 4.18: Simulation showing the effects on focal intensity for simulated non-uniform Fresnel cone form. First row shows an additional azimuthally varying sinusoidal phase with a period of 2 and amplitude of λ, second row shows a period of 2 and amplitude of 2λ, and third row shows a period of 4 and amplitude of λ. Note that the line profile is in the x-direction (horizontal axis), through the centre of the plot.

When adding an azimuthally varying sinusoidal phase to the simulated cone beam prior to focussing, Figure 4.18 shows that if this sinusoidal variation has a period of 2, it acts as though there is a tilting of the Fresnel cone and the focal spot intensity is distorted in a particular direction. Furthermore, if the amplitude of this additional phase is increased, the effect on the focal spot is further exaggerated. Interestingly, given a period of 4 (imitating a physical Fresnel cone that is perhaps 'warped' or 'pinched' across two perpendicular axes), the intensity pattern generated in the focal plane consists of an arrangement of focal spots and shapes. While not as uniformly or symmetrically distorted as the simulated results shown in Figure 4.18, the measured focal spot shown in Figure 4.15 suggests that perhaps the non-ideal focal spot is more due to a non-uniform distortion of the Fresnel cone shape rather than surface roughness.

As a final part of the investigation of the distorted focal spots generated by the Fresnel cone beam, an additional lens (f=25 mm, in order to de-magnify the beam to fit on the camera sensor) was placed in the above setup prior to the camera, in order to image the cone surface to the camera plane for visual inspection. The surface of six separate 2^{nd} generation Fresnel cones was inspected in this way, with camera images shown below in Figure 4.19.

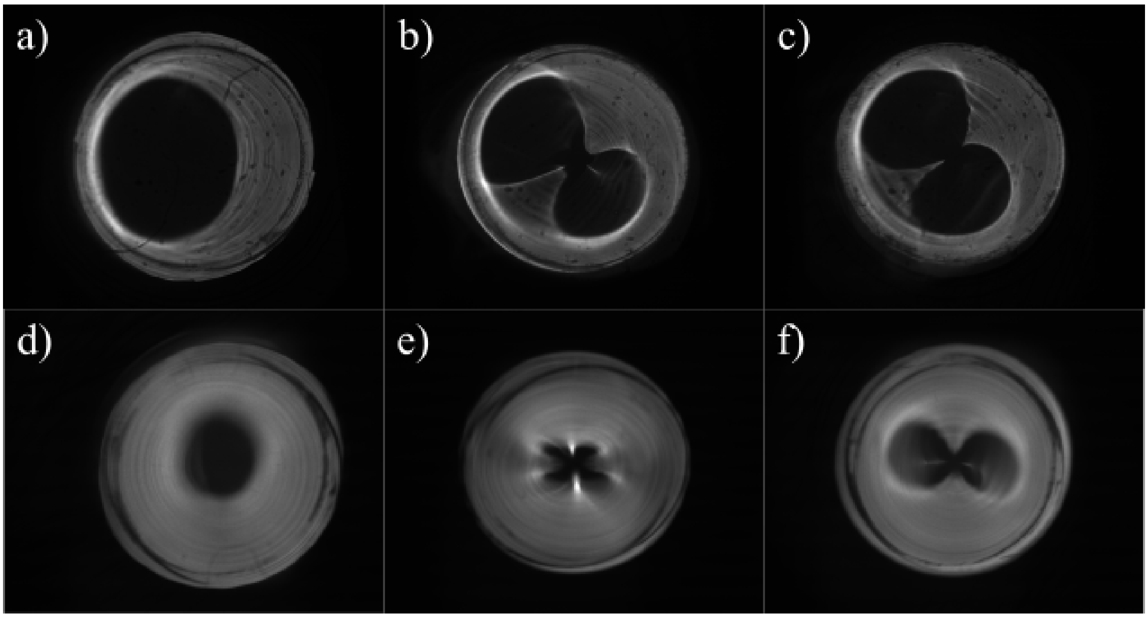

FIGURE 4.19: Camera image of Fresnel cone surfaces for six separate 2^{nd} generation Fresnel cones, as visual inspection of quality.

Figure 4.19 visually reveals an issue in the form of dark areas (or optical voids). In some cases this manifests as a single circular void and in others a two or four lobed shape. As previously explained, given a 90° apex angle, the optical path length at each transverse position into a cone results in the possibility to image the entire surface plane to a camera. These dark regions may therefore be due to in some areas a lower or higher than 90° apex angle. One could argue that it may possibly be of an angle lower than that required for TIR to occur, resulting in light in those transverse positions transmitting through the rear surface of the cone. I note that although these patterns appear to suggest non-uniformity on opposite sides of the cone surface (due to the pattern symmetry), it is equally possible that the defect is encountered only on one side. This is because light entering the cone at any position must undergo two reflections at opposing sides of the rear cone surface, so light impinging either at the transverse position of the defect or the opposite side of the cone would encounter the defected surface at least once. I note that the apparent darkened ring at the outer edge of the cone images is due to the rubber o-ring used to secure the cones in their mount.

The images of the 2^{nd} generation cone surface appear is visibly smooth without the periodic ridges encountered during previous work with the 1^{st} generation cones, however, there are apparent optical voids in the centre. This is likely an imaging problem and suggests that perhaps the apex angle is not uniform in the 2^{nd} generation cones, though surface quality is visibly relatively smooth. In an attempt to rectify the problem, higher quality Fresnel cones were purchased through a bespoke order where we specified a requirements for an apex angle of $90° \pm 30'$ and a maximum surface irregularity of 0.5 fringes. An image of the new 3rd generation cone surface is shown below in Figure 4.20.

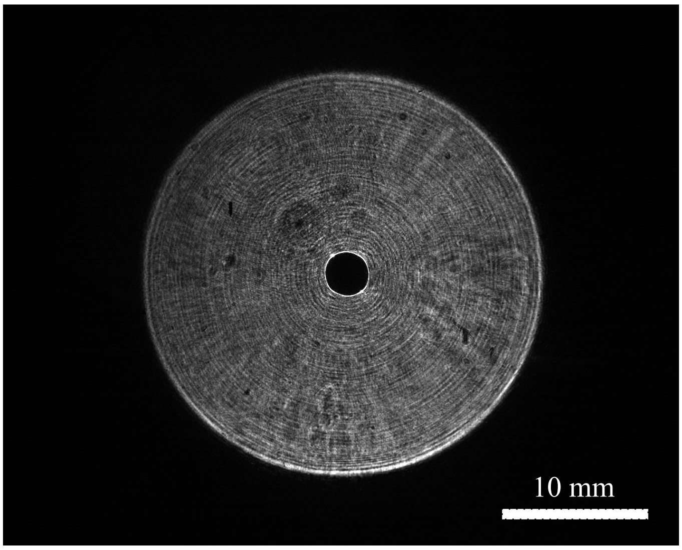

FIGURE 4.20: Camera intensity image of 3rd generation Fresnel cone surface.

Visual inspection of the 3rd generation Fresnel cones showed an apparently enhanced surface smoothness, and although there still appeared an optical void this was limited to the central (cone tip) area. I additionally note there are closely-packed concentric lines visible which may not be insignificant. Unfortunately, upon insertion of the newly acquired Fresnel cones into the low NA focussing experiment, results did not improve and the same distorted focal spots were observed. The next section describes a more in depth analysis of the Fresnel cone surface quality in an effort to understand the focussing problem encountered, and ascertain whether the issue can be rectified.

4.4.2 Surface topography measurement and fringe pattern analysis

In the previous section, a distorted focal spot was observed for an azimuthally polarised Fresnel cone beam, focussed by a low NA lens. Investigations into the possible cause of this consisted of measuring a simulated focal spot for a variety of added phase aberrations to the focussed beam, imitating Fresnel cone surface roughness and non-uniform conical form. The results of these simulations and visual inspection of the cone surface when imaged to a camera, suggest there are issues with the physical shape of the Fresnel cone. To further investigate this, an interferometry experiment was performed to experimentally measure the surface of a Fresnel cone. A technique demonstrated by Takeda et al. [121], often used to determine the surface flatness of components such as mirrors or spatial light modulators, was followed. It was supposed that given the fact that totally internally reflected light from a Fresnel cone experiences the same optical path length at each incident transverse position, the same technique could be similarly applied as if measuring the flatness of a plane reflective mirror.

The surface measurement technique involves analysis of the Fourier spectrum of a non-contour fringe pattern. This is advantageous over other techniques, such as Moire topography [122], as sensitivity in this case is limited to surface elevations above 2π[4]. The experimental setup used to generate the fringe patterns for analysis is shown below in Figure 4.21.

---

[4] Surface elevations below 2π generate no fringes.

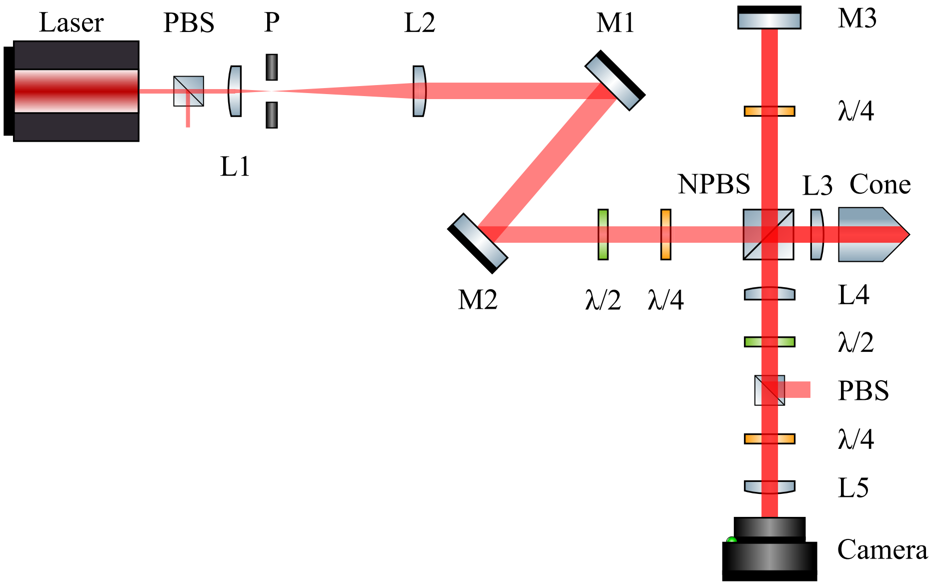

Figure 4.21: Experimental setup used to generate fringe patterns for Fresnel cone surface flatness analysis. PBS is a polarising beam-splitter. NPBS is a 50:50 non-polarising beam-splitter. L1-5 are lenses f=50, 200, 2500, 175, 25 mm respectively. P is a 10 μm pinhole. M1-3 are mirrors. $\lambda/2$ and $\lambda/4$ are half- and quarter-wave plates respectively.

To generate the required fringe pattern, firstly, azimuthually polarised light must be generated using the Fresnel cone technique outlined earlier in this thesis. A 633 nm Helium Neon laser is used as the light source for this experiment. PBS is polarising beam-splitter. L1-5 are lenses f=50, 200, 2500, 175, 25 mm respectively. P is a 10 μm pinhole. M1-3 are mirrors. $\lambda/2$ and $\lambda/4$ are half- and quarter-wave plates respectively. The first telescope and pinhole are used to expand the beam to fill the Fresnel cone aperture, as well as being a spatial filter to provide a 'clean' Gaussian beam. M1 and M2 are used to aid alignment by steering the beam. The first half- and quarter-wave plate are used to generate the required circularly polarised light for incidence on the cone. One arm of the NPBS beam is directed towards a mirror, which reflects the beam to be used as the reference beam. The quarter-wave plate in this arm is to ensure the correct handedness of circular polarisation for interference. In the other beam-splitter arm, L3 is a long focal length lens of f=2500 mm, to provide a very slight focussing of the resulting cone beam. This is required to produce enough concentric tilt of the beam for generating fringes at the camera, with respect to the reference beam. The camera arm of the beam-splitter consists of imaging lenses which image the cone surface plane to the camera, as well as de-magnifying the beam to fit on the camera sensor. A half-wave plate is included to rotate the structured state to azimuthal polarisation, as discussed in section 3.4. A PBS and quarter-wave plate is also included in this arm in order to select only the circular component possessing OAM. The spiraling fringe result for the 1st generation cone was recreated (first achieved in [46]), for comparison in Figure 4.22a). Figure 4.22b) shows the observed spiral fringe pattern for the higher quality 3rd generation cone under investigation.

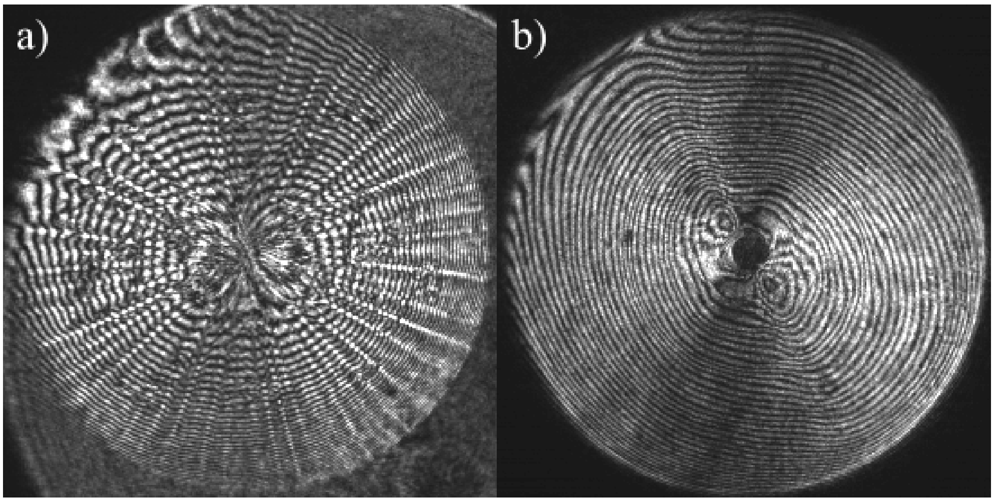

Figure 4.22: Spiral fringe patterns observed in the interferometer experiment described for a) 1st generation Fresnel cone and b) 3rd generation Fresnel cone.

Upon counting the fringe pattern spirals, it is found that the pattern spirals twice over 360°. This is as expected for a circular polarisation component possessing two units of OAM - a feature described earlier of the Fresnel cone beams. Comparing the fringe patterns for the two cones above, the pattern is visibly more 'jagged' for the 1st generation cone than that of the 3rd - suggesting that the surface quality is of a smoother finish. There is clearly issues near the central tip area of the beam in both cases, as well as a certain 'warping' of the fringe pattern.

In order to carry out the proposed Fourier spectrum analysis, I first performed a coordinate transform, unwrapping the x-y image to a polar coordinate frame in radius (r) and azimuth (θ), shown below in Figure 4.23a) and b).

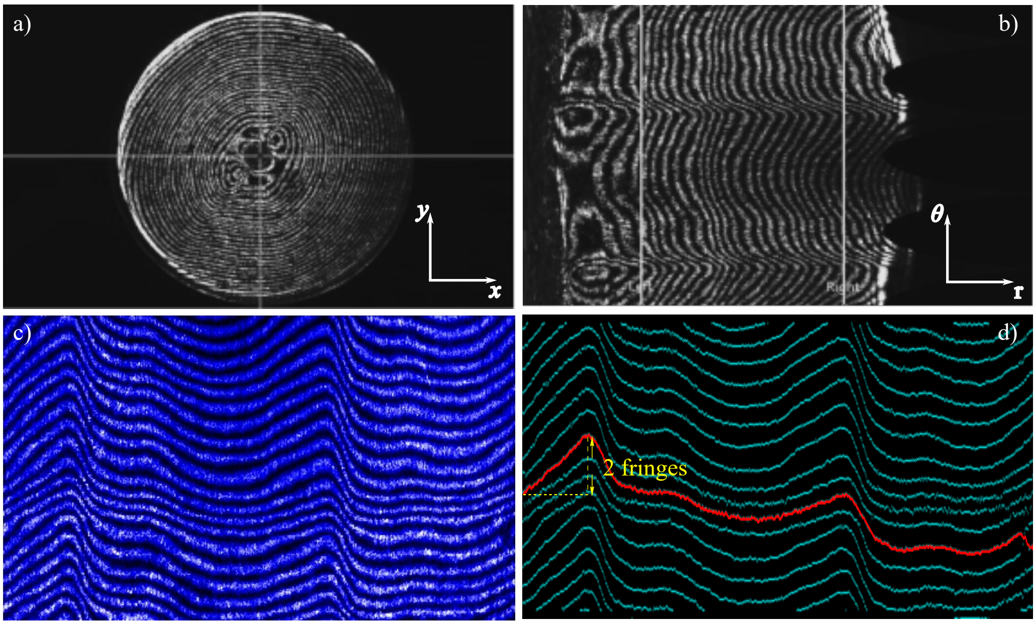

FIGURE 4.23: a) shows the fringe pattern in the x-y frame, b) shows the fringe pattern in the polar r-θ frame, c) shows the selected region of interest avoiding the noisy centre and outer edge and d) shows plotted lines matching the troughs in the fringe pattern using the in-built peak-matching algorithm to LabVIEW.

The crosshairs in Figure 4.23 a) are used to select the centre of the image for coordinate transformation. Figure 4.23 b) shows the fringe pattern in the polar coordinate frame, where two vertical cursors are used to select a region of interest (ROI) for analysis. Selecting an ROI in this way avoids including the distorted tip area and blank outer edges (left over from coordinate transformation) in the analysis. Figure 4.23 c) shows the selected ROI (rotated for aesthetic reasons). Already from this data, visually it appears there are raised ridge-like areas in the fringe pattern. Given the OAM, the unwrapped fringe pattern should theoretically consist of straight fringes with a slight slope. A peak-matching algorithm inbuilt to LabVIEW was utilised to locate the line coordinates of a single fringe (sub VI (LabVIEW Virtual Instrument file) named “NI_AAL_SigProc.lvlib:Peak Detector.vi”). This is in order to measure the fringe height difference of the apparent ridge-like feature. Figure 4.23 d) shows that the measured height difference taken from the emboldened line coordinates is $\sim$ 2 fringes. This is larger than the surface irregularity quoted when purchasing the 3rd generation Fresnel cones of $<$ 0.5 fringes - communication with the company to rectify this is ongoing at this time.

For Fourier spectrum analysis, a 2D Fast Fourier Transform (FFT) is performed on the fringe pattern Figure 4.24a), with the result shown in Figure 4.24b). As described in [121] similarly for analysis of a 1D signal, the two Fourier spectra in the spatial frequency domain are separated by a carrier frequency. One of these spectra is chosen, and shifted by the carrier frequency to the centre. Figure 4.24b) shows the two crosshairs used labelled ‘TL’ and ‘BR’ for top-right and bottom-left, used to select the rectangular area of the Fourier spectrum for shifting. Once shifted, an inverse complex-FFT is performed and the imaginary component is selected to visualise the phase, with the modulo-2π result shown in Figure 4.24c). This modulo-2π result has discontinuities at every phase step of 2π, similarly to what was shown for the 1D case in [121], shown in Figure 4.25a).

In order to correct for the phase discontinuities, an offset phase distribution can be determined, which can be added to the discontinuous distribution. By calculating the phase difference between two adjacent points in a particular direction (x or y), as the variation in phase should change only slowly (increments much less than 2π), any phase differences close to π indicates a discontinuity (as the phase map ranges from $-\pi$ to $+\pi$). I chose to specify that where any absolute phase differences of at least 0.9π occurs, a phase offset is recorded where 2π is added or subtracted depending on the sign of the phase difference detected (starting at 0 for the first point). A phase offset is constructed similarly to as is shown in Figure 4.25b). This can then be added to the calculated phase distribution Figure 4.24c) to remove the discontinuities. This was carried out for discontinuities in the x-direction with result shown in Figure 4.24d). This could also be carried out for discontinuities in the y-direction to produce a more continuous phase distribution.

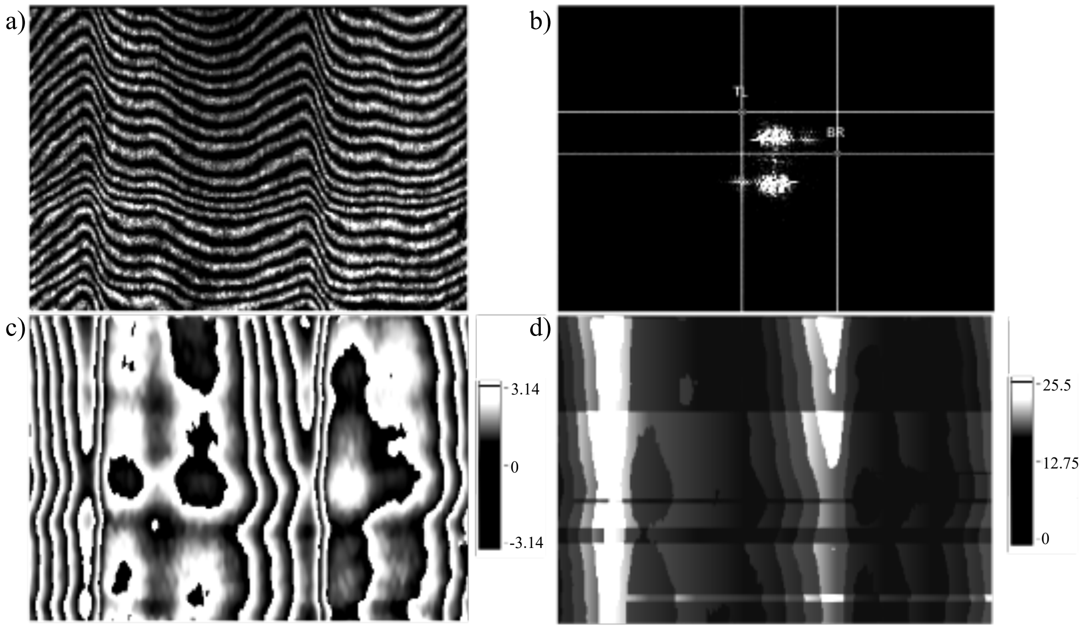

FIGURE 4.24: a) shows ROI fringe pattern for Fourier analysis, b) shows Fourier spectrum after FFT, c) shows modulo-2π phase distribution, d) shows phase distribution corrected for discontinuities in the x-direction.

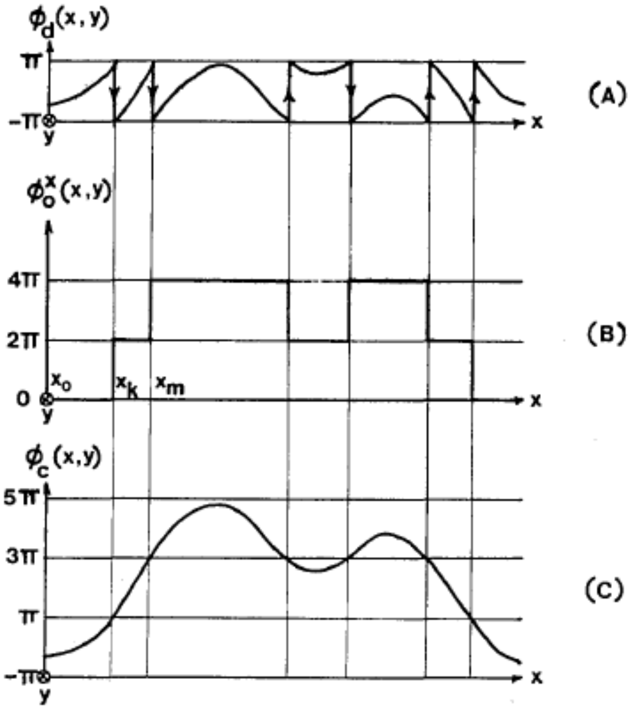

FIGURE 4.25: Image from [121]. a) example of phase discontinuities, b) offset to phase distribution for discontinuity correction and c) corrected continuous phase distribution.

The corrected phase distribution was coordinate transformed back to an x-y coordinate frame from the polar coordinate frame - shown below in Figure 4.26a). The centre of the image and outer edge of the cone surface is missing due to the ROI selection performed during analysis, however, there are clearly two raised ridge-like elevations seen in the reconstructed phase map of the cone surface. The maximum height of the detected elevation from the baseline is $\sim 25.5/2\pi \approx 4.06\lambda$. Given that there are two units of OAM to account for in the spiral fringe pattern (resulting in an overall artificial slope being included in the surface measurement), 4π can be subtracted, leaving an actual elevation of $\sim 12.94/2\pi \approx 2.06\lambda$. This agrees with the earlier observed fringe height of the elevated ridges of ~two fringes. These raised elevations can also be seen in both the original measured fringe pattern as well as the camera intensity image of the cone surface, highlighted in Figure 4.26b) and c).

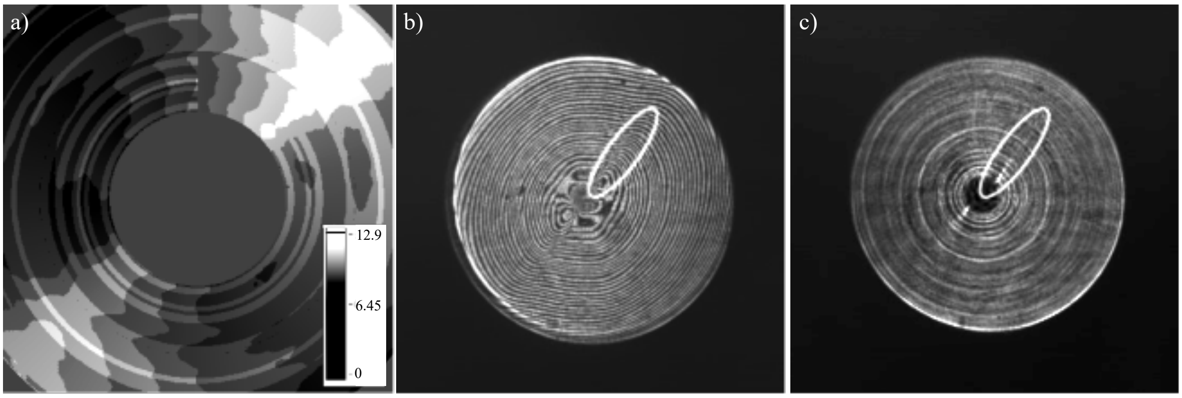

Figure 4.26: a) Reconstructed phase distribution of cone beam, highlighted elevations in b) measured fringe pattern from interferometry experiment and c) camera intensity image of cone surface.

Elevated ridges discovered on the cone surface likely result in a non-uniform aberration to the generated beam, where simulation results showed earlier in this chapter have a detrimental effect on the resulting focal spot.

4.5 Conclusions

In this chapter, I have shown through simulation (based on the Richards and Wolf vector diffraction theory [47]) that azimuthally polarised light generated using the Fresnel cone technique can allow sub-diffraction limited focal spots. Not only this, but these beams produce a smaller focal spot than conventional beams, even for lower NA focussing (unlike the results of conventional radial polarisation). It is noted however, that as NA increases, the radially polarised focal spot size does approach that of the azimuthal beam. Similarly, this is also the case for a fixed high NA but with an increasing centre-stop in the objective lens pupil plane - essentially restricting the focussing also to an increasing NA.

I have shown simulation results for the case of the radially polarised Fresnel cone beam, which do not initially appear interesting for microscopy due to a relatively large focal spot size. From these results however, it was noticed that the phase of the (ring-shaped) longitudinal electric field component varies azimuthally from 0-2π. It is likely that this is a result of orbit-spin conversion in the focussing region, as shown recently by Kotlyar et al. [123], with a resulting transverse spin component [124]. It is expected that this longitudinal field component and azimuthally varying phase will be of interest to the fields of microscopy and particle trapping.

Evidence through simulation that Fresnel cone beams can allow the sub-diffraction limited focal spots demonstrated by Hao et al. [57] and our own unpublished results, prompted the formation of an industry-led collaboration project to develop a bolt-on microscope module for provide high efficiency broadband polarisation structuring. During this project I developed a technique for pre-compensation of vector beams. This technique allowed the desired azimuthally polarised light to reach the pupil plane of an objective lens, following interaction with compulsory optical elements that are often detrimental to the polarisation state. I implemented a patented dual cone-based polariser [120] into a prototype device, for initial testing at the University of Glasgow. I was able to generate high fidelity polarisation structures with this prototype, however, the reliance on two individual cone halves in the dual cone-based polariser revealed a crucial issue with the cone alignment and resulting global phase of the generated beam. Focussing simulation which included this phase misalignment highlighted that with the current cone-mount precision and 3D printed housing, it would not be possible to generate sub-diffraction focal spots.

Knowledge gained through the industry-led collaboration project highlighted the previously unconsidered effects on focussing of non-ideal phase aberration to the generated Fresnel cone beams. A simple low NA focussing experiment was set up as an initial test of the focussing such beams (with the previously used beam-splitter coupling into the cone rather than prototype device), where non-ideal distorted focal spots were observed. This suggested there were possible issues with the surface quality of the Fresnel cones and so higher quality cones were obtained, however, results did not improve. I began an investigation into both the surface roughness and conical form of the newly acquired Fresnel cones, in an attempt to identify the issue. Using an interferometry experiment and Fourier spectrum analysis, previously demonstrated for use to measure the surface of components such as mirrors [121], I was able to use interference of the generated cone beam with a reference beam, to identify elevated ridge-like regions of the cone surface with an approximate height of $\sim 2\lambda \approx 1\ \mu$m. As shown in simulations, where I used phase distortions to imitate a warping of the Fresnel cone surface, these types of phase aberration are extremely damaging to the desired focal spot (while surface roughness is less critical below a certain amount).

It may be possible to correct the phase aberrations gained by the generated cone beams using a liquid crystal spatial light modulator (SLM) - an array of individually tunable birefringent liquid crystals - allowing an ideal focussing situation. Given the time available this possibility was not further explored, as initially where the industry-led collaboration was concerned the stated benefits of the bolt-on device were that it would be low-cost and allow broadband operation. If including a liquid crystal SLM in the setup, this would no longer be the case. Further comments on the findings and future of this work can be found in chapter 6.

Chapter 5

Single-shot polarimetry using a Fresnel cone

5.1 Introduction

In the previous two chapters I have discussed the use of a Fresnel cone for generating beams with interesting polarisation states (chapter 3) and where these beams could be applied (chapter 4). In this chapter I will show how a Fresnel cone can also be used to measure light's polarisation. This can be extremely useful as knowledge of light's polarisation can reveal information about its source, due to light becoming polarised to at least some degree upon reflection or transmission. For example, important uses are found in tissue polarimetry in biomedical research [125] and target detection in radar polarimetry [126]. Conventional cameras are blind to this vector property of light as they are sensitive only to intensity (and colour), not orientation and phase of the electric field, however, devices do exist that can measure polarisation. These are known as polarimeters, where the majority use the relation of the Stokes parameters to intensities of light to perform a polarisation measurement. This establishes a requirement for multiple measurements of the incident light to be able to achieve full-Stokes polarimetry and recovery of the complete polarisation state (in the form of a Stokes vector - described in subsection 2.3.2).

Commercial polarimeters are often based on a "rotating-waveplate" design [127] due to the technique being simple and compact, however, this has drawbacks if the incident polarisation signal is changing on time-scales comparable to (or faster than) the temporal rotation frequency of these devices (for example, if the polarimeter and light source are in motion relative to each other). Devices with moving parts are also inherently unstable and may require regular maintenance or re-calibration, however, this technique is still commercially preferred when compared to more expensive and complex spatially-modulated (or amplitude-splitting) techniques which record multiple measurements simultaneously [128, 129].

Using the polarisation structuring of a Fresnel cone, I performed an experiment to show that it can be used as a single-shot polarimeter that is both compact and relatively low-cost. Not only this, but it has no moving parts and unlike the majority of polarimeters it allows broadband operation, as it is not based on the use of birefringent components. It should be noted however that the Fresnel cone polarimeter does not currently allow imaging polarimetry, as the incident polarisation state must be homogeneous over the front surface of the Fresnel cone (see Figure 5.4 for polarimeter diagram). An imaging capacity could potentially be implemented using a scanning technique[1], though the device would no longer provide results in a 'single-shot'. On a positive note however, the Fresnel cone device may be better suited for polarisation spectroscopy of homogeneous samples, for example, for chirality measurement of liquid samples.

In this chapter I will describe some of the useful applications for polarimetry, highlighting that different applications have different requirements for the polarimeter device. I will discuss the various measurement domains used for polarisation modulation of the incident light, such as the temporal, spatial, and spectral domains. I will go into particular detail describing the common "rotating-waveplate" approach, as the Fresnel cone polarimeter is revealed to be a spatial analogue to this. I will then show the theory, experiment and results of the Fresnel cone polarimeter, before discussing its benefits, recent research into similar devices, and the challenges and future of the field.

My contributions to this work included writing programs to simulate the experiment and analyse data, setting up the experiment, collecting and analysing the data, and co-writing the manuscript for publication [130].

---

[1] Providing it is possible to include the Fresnel cone polarimeter in the beam-path prior to the detector

5.2 Conventional polarimetry

As mentioned, polarimeters can reveal useful information about light's origin and the object's it interacts with by measuring its polarisation state. They are therefore important tools in a wide range of fields such as material characterisation [131–133], astronomy [134–136], medicine [125, 137, 138] and remote observation [126, 139, 140]. In subsection 2.3.2 I showed that the two orthogonal complex electric field components representing a polarisation state (Jones vector) can be expressed as four real numbers in a Stokes vector. As there are four unknown quantities, at least four measurements must be made for complete Stokes vector recovery. These are usually achieved by modulating the polarisation of the incident light in either a spatial, spectral or temporal manner. It may be useful to note that these different approaches can be labelled differently depending on the community in question. In the field of astronomy for example, the polarisation measurement domain is called a 'modulation', such as spatial, spectral or temporal modulation. Alternatively, in the field of remote observation and target detection, these measurement domains are labelled as a 'division of amplitude', 'division of time' and so on. Each approach to polarimetry may have benefits and drawbacks, but polarimeters can be designed to be optimal for the required application. For example, a low-cost birefringent rotating wave-plate design may be compact and suitable for general laboratory use, while a passive broadband polarimeter that has no moving parts is more suitable for applications in space or remote observation where the source is in motion relative to the detector, or remote observation where spectro-polarimetry may be required.

5.2.1 Applications

Polarimeters can clearly be useful in a wide range of application areas, where information is sought that normal cameras are not able to reveal. While the intensity and wavelength of light are affected by the material of the object the light interacts with, the resulting polarisation state depends on an objects parameters such as orientation and surface roughness, and so provides complimentary information to the conventionally measured intensity and colour. Since light's polarisation is affected by the surface features of objects in a scene, it is a very useful tool in the field of target detection as man-made objects tend to differ in these regards when compared with objects in nature. By applying imaging polarimetry to a scene where a Stokes vector is measured for each camera pixel, the image contrast can be enhanced to reveal objects that would usually be hidden to visible and thermal cameras, for example, exposing a camouflaged tank in thermal equilibrium with its surroundings. Polarimeters are also useful for detecting marine oil spills [141, 142], where previously infrared imaging was used to try and detect these spills, however, at times the contrast between oil and surrounding water can be minimal when thermal equilibrium sets in. Since oil and water have different optical properties, by illuminating a scene with polarised light and then observing the polarisation properties of the reflected light, devices can be made to provide high contrast for detecting these spills (see Figure 5.1). Using a polarimeter in this way has the benefit that it does not solely rely on temperature difference, and functions even if a target oil spill is in thermal equilibrium with the surrounding water [143]. As large areas often need to be measured, polarimeters for target detection must allow fast operation as they would ideally function in real time.

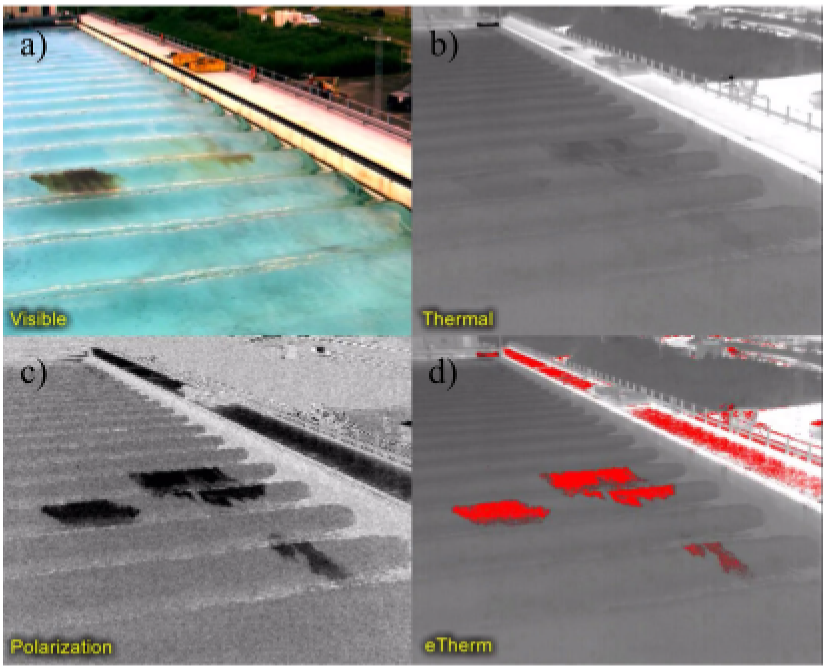

Figure 5.1: Here work by a company called Polaris Sensor Technologies shows a) oil spill scene captured using visible light, b) an infrared thermal image c) an image of the degree of linear polarisation and d) a fused image of the thermal and polarisation data. It is also possible to see that the man-made objects around the pool clearly polarise the light. Image adapted from reference [143].

Polarimeters have also long been a tool in the field of remote sensing, where they are primarily used to characterise aerosol particles in the atmosphere. Climate modelling is an obvious research area where atmospheric aerosol data is essential, however, this data is also required to be able to remotely monitor atmospheric particles such as hazardous pollution and ash particles from volcanic eruptions. Polarimeters used for remote sensing are often housed on orbiting satellites, where the most well-known satellite polarimeter is the POLDER instrument [144, 145]. This device employs a filter wheel at three different wavelengths (440, 670 and 885 nm) for recording spectral data, where each filter is also polarisation filtered with a linear polariser at three different angles (0°, 60° and 120°). As the POLDER polarimeter device records time sequential polarisation images however, there is an inherent error due to the scene changing between measurements due to the relative motion between scene and detector. The result is that the accuracy of the POLDER polarimeter is limited to $\sim 2\%$ [146].

For applications in astronomy, there are two commonly used types of polarimetry. Spectro-polarimetry is used to study the atmospheres of exoplanets (where polarisation is measured as a function of wavelength), while imaging polarimetry can be used to study stellar atmospheres and the surrounding region. Recently, a spectro-polarimeter device was developed with the aim of using it to aid in the detection of life on exoplanets [147]. The device is based on the technique devised by Sparks et al. [148], which uses a patterned quarter-wave plate with varying fast axis followed by a linear polariser and a slit to produce a modulated spectrum (See Figure 5.2).

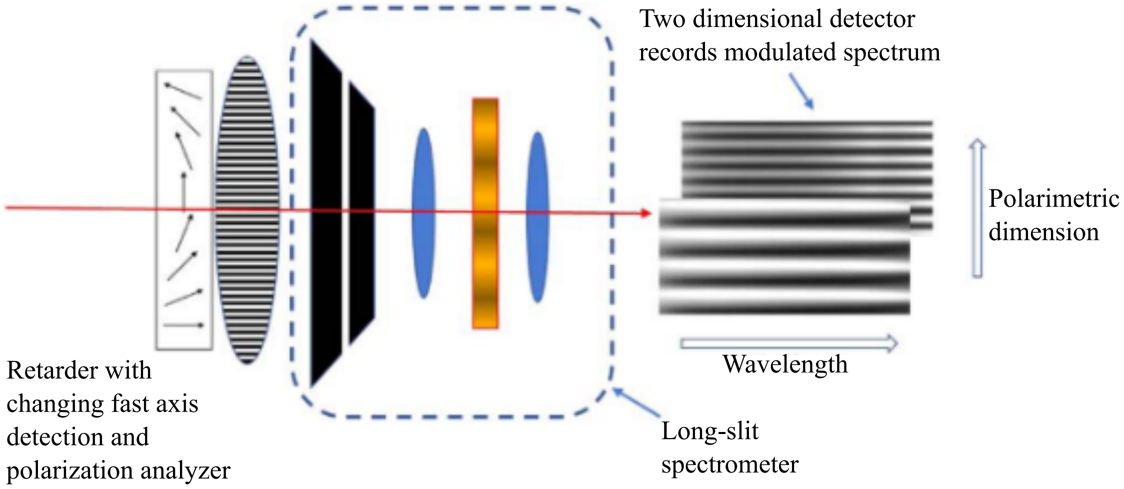

Figure 5.2: A diagram showing the polarimeter design by Sparks et al. [148]. Light is incident on a patterned quarter-wave plate followed by a linear polariser and long slit spectrometer. The intensity patterns to the right are simulations of what is expected for linear and circularly polarised light. Image from [148].

The spectrum resulting from the setup shown above is recorded by a camera for Fourier analysis to reveal the incident polarisation state. This is similar to the Fourier analysis approach I show for the Fresnel cone polarimeter I describe in subsection 5.3.3. Importantly, the design by Sparks et al. allows high accuracy for measuring the circular polarisation component without cross-talk with the linear polarisation components. This facet is essential to be able to use polarimetry to search for signs of life as the main molecules required for constructing life are chiral. Chirality[2] results in light becoming partially circularly polarised upon interaction - hence is suggested as a possible biomarker in the search for extraterrestrial life [149]. It is further advantageous that the device design is solid-state, i.e. it has no moving parts and hence is suitable for use in space. In addition, a polarimeter for this application needs to be both highly accurate and sensitive, as the contrast between polarised reflected light from exoplanets and the unpolarised light from its host star can be as low as 10^{-7} to 10^{-10} [146].

Simple polarisation microscopy techniques have been developed for use in biomedical diagnosis, usually involving imaging some form of birefringent sample between two crossed polarisers [150, 151] or investigating chiral samples [152]. These simple methods however only qualitatively enhance contrast and are usually used as a complimentary second or third back-up technique to assist in sample identification. Quantitative polarimetry methods are also being developed for tissue imaging where these devices additionally use a dynamically controllable input polarisation state (polarisation state generator), allowing full Mueller matrix polarimetry [81, 153] and more in depth analysis. A straightforward method for experimentally measuring a Mueller matrix was given in section subsection 2.3.4. A sample's Mueller matrix can be decomposed to give depolarisation, retardance and polarisance, assisting in identifying potential tumours [153, 154].

From these applications it is clear that the requirements and desires of the polarimeter design depend on its purpose, for example, an application in space requires that the device is especially robust and has no moving parts, applications in target detection often require real-time polarimetry and so the technique must have fast operation, remote observation requires high sensitive and biomedical applications often use in addition to the polarimeter a polarisation state generator to allow dynamic control of the incident state and Mueller matrix measurement. For many

---

[2] Actually they essentially have homochirality, as 19 of the 20 molecules required for constructing life are left-handed, with the remaining one is right-handed.

applications it would be very useful to be able to perform the polarimetry spectrally, or that the device itself allowed broadband operation, however, many polarisation optics rely on birefringence which is inherently wavelength dependent.

5.2.2 Modulation domains

In this section I will discuss the different modulations of the incident polarisation signal that may be addressed with a polarimeter device. The **spatial modulation** approach to full-Stokes polarimetry involves taking the incident light beam and dividing it into several sub-beams, where each sub-beam is individually analysed by its own set of analysing optics. This can be achieved straightforwardly with multiple beam-splitters, polarisation optics and detectors in a "division of amplitude" approach such as the experiment devised by Campain and Drevillon [155]. Here an uncoated beam-splitter is first used to split the incident light into two sub-beams, which are subsequently divided again by two Wollaston prisms, before incidence on four individual detectors. An advantage of this technique is that it does not rely on birefringence and was demonstrated to operate in a broad wavelength range of 0.4 to 2 μm [155]. More recent approaches for achieving simultaneous Stokes measurement use a "division of focal plane" design where instead the detector itself is divided, using components made by advanced manufacturing techniques. One example of this is the elliptical-polariser array system demonstrated by Hsu et al. [156]. Designing a polarimeter based on spatial splitting has the advantage that the measurements are acquired simultaneously (crucial for some applications) and some devices allow spatial resolution, however, these devices can be complex and expensive.

An alternate measurement technique is to modulate the incident light spectrally - sometimes known as 'channeled spectro-polarimetry', or the **spectral modulation** approach. This technique usually assumes that the incident light is broadband in nature. The main idea in this technique is to create an analyser system that is a function of wavelength, for example, achieved by using two multi-order waveplates at 45° to each other before an analyser polariser. These multi-order waveplates retard the phase chromatically, introducing side-bands in interferogram space which are subsequently measured using a diffractive spectrometer [146]. These polarimeters offer many benefits associated with space and remote sensing applications, such as single-shot, compact, passive and accurate, however, a potential major drawback arises when there is absorption at certain frequencies (such as in atmospheric absorption), causing false measurements in the intensity spectrum [157].

The third and perhaps most popular method for polarimetry is the **temporal modulation** approach, where incident light is modulated in a time-sequential manner. The most basic temporal modulation design uses a rotating quarter-wave plate, though there are numerous techniques reported investigating photo-elastic modulators [158, 159] and liquid crystal variable retarders [160, 161] for temporally modulated polarimetry. From a commercial point of view a device is preferentially simple, low-cost and compact, and although the spatial measurement domain offers simultaneous Stokes measurements a temporally modulated design satisfies these criteria. The basic setup for the typical commercial rotating wave-plate device is a motorised spinning quarter-wave plate followed by a linear polariser and an intensity measurement on a detector. Using the Stokes formalism detailed in chapter 2 this can be summarised as

$$\mathbf{S'} = \mathbf{M}_{\text{pol}}\mathbf{R}(-\theta)\mathbf{M}_{\text{qwp}}\mathbf{R}(\theta)\mathbf{S}, \tag{5.1}$$

where $\mathbf{S} = [S_0, S_1, S_2, S_3]^T$ and $\mathbf{S'} = [S_0', S_1', S_2', S_3']^T$ are the initial and final Stokes vectors respectively, the $\mathbf{M}$ matrices are Mueller matrices corresponding to a horizontally aligned linear polariser ($\mathbf{M}_{\text{pol}}$), a quarter-wave plate with horizontal fast-axis ($\mathbf{M}_{\text{qwp}}$), and $\mathbf{R}(\theta)$ is the Mueller rotation matrix for a rotation of θ. Here I note that $\theta = \omega t$ for the rotating wave-plate. The matrices for the terms $\mathbf{R}(-\theta)\mathbf{M}_{\text{qwp}}\mathbf{R}(\theta)$ represent a quarter-wave plate rotated from the horizontal by the angle θ. The Mueller matrices used in Equation 5.1 are

$$\mathbf{R}(\theta) = \begin{bmatrix} 1 & 0 & 0 & 0 \\ 0 & \cos(2\theta) & \sin(2\theta) & 0 \\ 0 & -\sin(2\theta) & \cos(2\theta) & 0 \\ 0 & 0 & 0 & 1 \end{bmatrix}, \tag{5.2}$$

$$\mathbf{M}_{\text{qwp}} = \begin{bmatrix} 1 & 0 & 0 & 0 \\ 0 & 1 & 0 & 0 \\ 0 & 0 & 0 & 1 \\ 0 & 0 & -1 & 0 \end{bmatrix}, \tag{5.3}$$

and

$$\mathbf{M}_{\mathrm{pol}} = \frac{1}{2}\begin{bmatrix} 1 & 1 & 0 & 0 \\ 1 & 1 & 0 & 0 \\ 0 & 0 & 0 & 0 \\ 0 & 0 & 0 & 0 \end{bmatrix}. \tag{5.4}$$

As mentioned in subsection 2.3.6, it is important to define the coordinate system by stating whether a right or left-handed Cartesian coordinate system is used, whether light propagates in the ±z-direction and whether the observer is looking from or towards the light's source. Here I am discussing a right-handed Cartesian coordinate system, with light propagating in the $+z$-direction and the observer is looking towards the light's source. Upon inserting the known matrices into Equation 5.1 I obtain

$$\mathbf{S'} = \frac{1}{2}\begin{bmatrix} 1 & 1 & 0 & 0 \\ 1 & 1 & 0 & 0 \\ 0 & 0 & 0 & 0 \\ 0 & 0 & 0 & 0 \end{bmatrix} \cdot \begin{bmatrix} 1 & 0 & 0 & 0 \\ 0 & \cos(2\theta) & -\sin(2\theta) & 0 \\ 0 & \sin(2\theta) & \cos(2\theta) & 0 \\ 0 & 0 & 0 & 1 \end{bmatrix} \cdot \begin{bmatrix} 1 & 0 & 0 & 0 \\ 0 & 1 & 0 & 0 \\ 0 & 0 & 0 & 1 \\ 0 & 0 & -1 & 0 \end{bmatrix}$$
$$\cdot \begin{bmatrix} 1 & 0 & 0 & 0 \\ 0 & \cos(2\theta) & \sin(2\theta) & 0 \\ 0 & -\sin(2\theta) & \cos(2\theta) & 0 \\ 0 & 0 & 0 & 1 \end{bmatrix} \cdot \begin{bmatrix} S_0 \\ S_1 \\ S_2 \\ S_3 \end{bmatrix}. \tag{5.5}$$

Upon matrix multiplication, this becomes

$$\mathbf{S'} = \begin{bmatrix} S'_0 \\ S'_1 \\ S'_2 \\ S'_3 \end{bmatrix} = \frac{1}{2}\begin{bmatrix} S_0 + \frac{1}{2}S_1(1+\cos(4\theta)) - S_3(\sin(2\theta)) + \frac{1}{2}S_2(\sin(4\theta)) \\ S_0 + \frac{1}{2}S_1(1+\cos(4\theta)) - S_3(\sin(2\theta)) + \frac{1}{2}S_2(\sin(4\theta)) \\ 0 \\ 0 \end{bmatrix}. \tag{5.6}$$

The first element of the final Stokes vector (S'_0 in Equation 5.6) is by definition the total intensity on the detector,

$$S'_0 = I(\theta) = \frac{1}{2}\left[S_0 + \frac{1}{2}S_1(1+\cos(4\theta)) - S_3(\sin(2\theta)) + \frac{1}{2}S_2(\sin(4\theta))\right]. \tag{5.7}$$

By rotating the quarter-wave plate, intensity measurements are taken for a range of θ angles and recorded as a function of time. As long as the frequency of the rotation is known, each temporal measurement can be mapped to an angle of rotation. By converting Equation 5.7 to a truncated Fourier series in θ, the Fourier coefficients can be expressed in terms of the initial Stokes vector components as shown in subsection 5.3.3. These Fourier coefficients can be experimentally measured, and by performing a matrix inversion, the initial Stokes vector $\mathbf{S}$ can be recovered [162]. This will be shown in more detail below for the case of the Fresnel cone polarimeter, as the angular position in the conical geometry of a Fresnel cone allows its use as a spatial analogue to the temporally rotating wave-plate component.

5.3 Polarimetry using a Fresnel cone

When investigating the types of beams that can be generated with the back-reflection from a Fresnel cone (as described in chapter 3) we noticed that when imaging the cone onto a camera through a linear polariser filter, for each polarisation state input to the Fresnel cone a different intensity pattern was observed as shown in Figure 5.3. The question was then asked - is it possible from a particular observed intensity pattern (such as the example shown in the rightmost intensity pattern in Figure 5.3) to reveal what the polarisation state is for an arbitrary unknown input? After reading through the literature there were two approaches found that would allow the initial Stokes vector to be recovered from a single intensity image such as the example shown. A numerical approach as shown in [162] and a more analytical approach which I will describe below in subsection 5.3.1 for the Fresnel cone polarimeter.

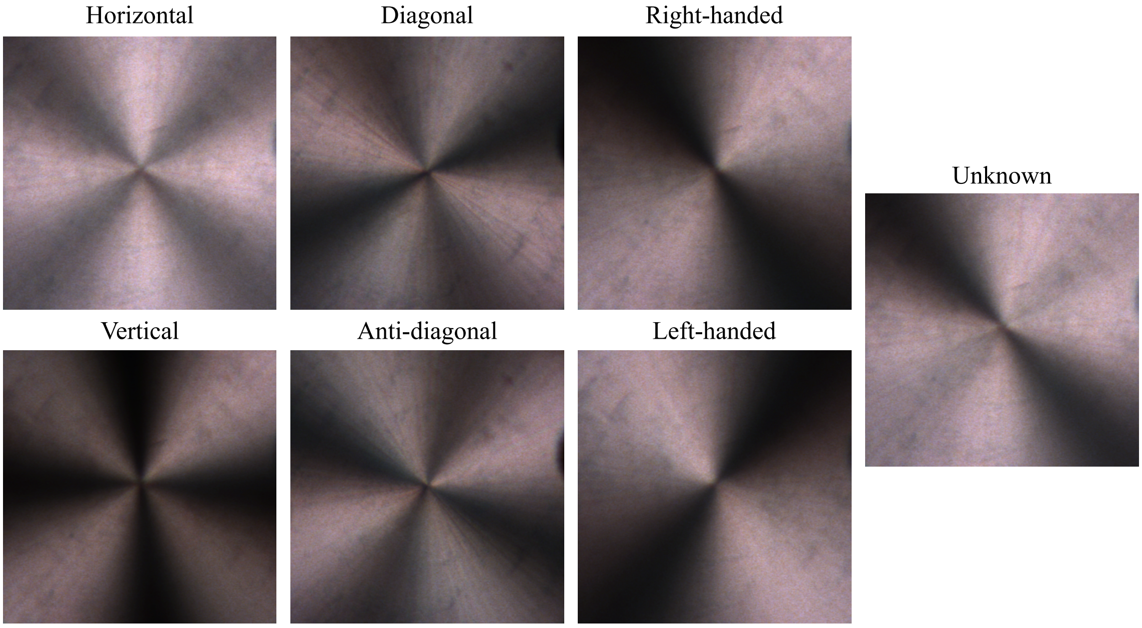

Figure 5.3: Experimental data. Intensity images of the Fresnel cone surface through a linear polariser for the labelled input states to the cone. It can be seen that linearly polarised inputs result in a four-lobed intensity pattern while circularly polarised inputs result in a two-lobed pattern. Also shown an intensity pattern for an arbitrary unknown input state.

5.3.1 Analogy to the rotating-waveplate polarimeter

The Fresnel cone based polarimeter consists of a Fresnel cone, a non-polarising 50:50 beam-splitter, a linear polariser, and a camera (See the components enclosed by the blue box in Figure 5.4). Similarly to Equation 5.1, the equation representing the Fresnel cone polarimeter using the Stokes and Mueller formalism is

$$\mathbf{S'} = \mathbf{M}_{\mathrm{pol}}\mathbf{R}(-\theta)\mathbf{M}_{\mathrm{wedge}}\mathbf{R}(\theta)\mathbf{S}. \tag{5.8}$$

Here, $\mathbf{R}(-\theta)\mathbf{M}_{\mathrm{wedge}}\mathbf{R}(\theta)$ is a rotated glass wedge (by an angle θ from the horizontal) which constitutes two total internal reflections, representing the function of a Fresnel cone. In order to derive the Mueller matrix for the glass wedge, the Jones matrix (first derived in [46], in which I was involved with during a Master's project) was converted using the method described in subsection 2.3.3. The Jones matrix used for the glass wedge is

$$\mathbf{M}_{\text{wedge}} = \begin{bmatrix} {r_p}^2 & 0 \\ 0 & {r_s}^2 \end{bmatrix} = {r_p}^2 \begin{bmatrix} 1 & 0 \\ 0 & e^{i2\delta}, \end{bmatrix}, \tag{5.9}$$

where

$$\delta = \arg(r_s) - \arg(r_p) = \arg\left(\frac{n^2 + i\sqrt{1-2n^2}}{1-n^2} \right). \tag{5.10}$$

Here, $n = n_{\text{air}}/n_{\text{cone}}$, and r_p and r_s are Fresnel reflection coefficients for the parallel (p) and perpendicular (s) polarisation components respectively. The angle of incidence at the back conical surface is above the critical angle for total internal reflection to occur, and so only the phase is affected at the boundary reflection and not the amplitude. By using a Fresnel cone with the correctly chosen refractive index n (see section 3.3 for theory), the phase-shift at each total internal reflection can be engineered to be $\pi/8$ for a cone with a 90° apex. As there are two reflections the result is that a Fresnel cone with a correctly chosen n acts similarly to a quarter-wave plate, with a fast axis varying azimuthally around the cone tip. Shown for completeness the Mueller matrix for the cone is

$$\mathbf{M}_{\text{cone}} = \begin{bmatrix} 1 & 0 & 0 & 0 \\ 0 & \cos^2(2\theta) & \frac{1}{2}\sin(4\theta) & -2\cos(\theta)\sin(\theta) \\ 0 & -\frac{1}{2}\sin(4\theta) & -\sin^2(2\theta) & -\cos(2\theta) \\ 0 & -2\cos(\theta)\sin(\theta) & \cos(2\theta) & 0 \end{bmatrix}, \tag{5.11}$$

where here θ is the azimuthal angle from the horizontal around the cone tip. The Fresnel cone Mueller matrix derivation was performed using the Jones-to-Mueller conversion method shown in subsection 2.3.3. Performing the matrix multiplications of Equation 5.8 and as before with the motorised rotating quarter-wave plate polarimeter, looking at the first element of the resulting Stokes vector S_0' I find that for the case of the Fresnel cone polarimeter system

$$S_0' = I(\theta) = \frac{1}{2}\left[S_0 + \frac{1}{2}S_1(1+\cos(4\theta)) - S_3(\sin(2\theta)) + \frac{1}{2}S_2(\sin(4\theta)) \right]. \tag{5.12}$$

This is identical to Equation 5.7 except here as stated θ now represents azimuthal angle around the cone tip rather than quarter-wave plate rotation angle at a given time, and so the Fresnel cone polarimeter is revealed to be a spatial analogue to the conventional temporally rotating quarter-wave plate device. This means that the intensity measurements required to determine an unknown incident Stokes vector can be recorded in a single intensity image for the Fresnel cone device, compared with the requirement to take sequential intensity measurements temporally with the conventional rotating wave-plate device.

5.3.2 Experimental setup

The experimental setup used in a proof-of-principle experiment is shown in Figure 5.4. The general principle is to generate visible broadband light that can be arbitrarily polarised and demonstrate that this polarisation state can be recovered in the form of a Stokes vector from Fourier analysis of the spatial intensity pattern of a light beam that has been reflected from a Fresnel cone and passed through a linear polariser. Using this system I am able to demonstrate the operation of the Fresnel cone polarimeter for broadband light. In this case I show operation across the visible spectrum, however, as explained in section 3.3 the technique could operate broadly across other frequency bands if the Fresnel cone material is engineered with a specifically chosen refractive index. It is also possible that even if a less-than-ideal refractive index is used for a given wavelength, this could be accounted for in the analysis, however, the polarimeter accuracy may be reduced (due to not encompassing a sufficient volume of the Poincaré sphere).

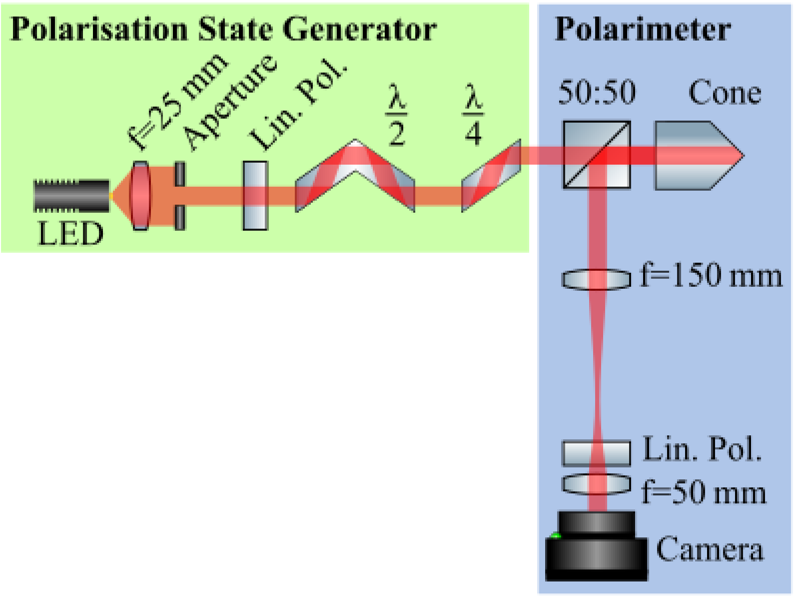

Figure 5.4: Fresnel cone polarimeter experimental setup. Polarisation states are generated using the polarisation state generator in the green box, before analysis by the Fresnel cone polarimeter in the blue box on the right. Figure adapted from [130].

The LED light source used for the demonstration of broadband operation is an incoherent white mounted LED (400 − 700 nm wavelength range) from Thorlabs (MCWHL6) with the LED driver LEDD1B also from Thorlabs. A 25 mm focal length lens (Thorlabs, LA1951-A) is used to collimate the LED source, followed by an iris to produce a beam of white light with the desired diameter[3]. The linear polarisers used were Thorlabs LPVISE100-A, with an operating wavelength range of 400−700 nm. The beam-splitter is a non-polarising 50:50 (reflection:transmission ratio) beam-splitter from Thorlabs, BS013, with an operational range of 400 − 700 nm. The Fresnel rhomb retarders (FR600QM and FR600HM for the quarter- and half-wave retarder respectively) are from Thorlabs. These Fresnel rhomb retarders provide a quarter- (an optional addition if circular/elliptical polarisation input is required) or half-wave retardance for a broad wavelength range (400 − 1550 nm in this case) and the details of their operation is described in subsection 2.4.3. These are essential for use with white light to demonstrate the broadband nature of the Fresnel cone polarimeter. First and second generation cones were tested in the polarimeter device. The 150 mm and 50 mm focal length lenses image the cone surface (this is possible as the optical path lengths for perpendicularly incident light rays are all equal regardless of which transverse position the light enters the cone) to the camera, as well as provide a de-magnification of $\frac{50}{150}$ of the beam so that it fits onto the camera sensor. The lenses, linear polarisers and non-polarising beam-splitter have an anti-reflective coating for use in the visible wavelength range. The camera is a colour CMOS camera with 1280 × 1024 pixels, Thorlabs DCC1645C, which is connected to a computer via USB 2.0.

The first step is to generate arbitrarily polarised light, for testing of the polarimeter. As light from the LED source is unpolarised, the first linear polariser is set to have its axis horizontally aligned (arbitrarily chosen) and the half-wave Fresnel rhomb retarder is rotated to generate all linear inputs (with the quarter-wave Fresnel rhomb retarder removed from the setup). This quarter-wave Fresnel rhomb retarder is replaced and fixed to have its fast axis horizontally aligned, and the half-wave Fresnel rhomb retarder is again rotated to generate a range of circular through elliptical input states. The non-polarising 50:50 beam-splitter then allows $\sim 50\%$ of the light to be transmitted to the Fresnel cone. The light is then back-reflected from the Fresnel cone (as described in section 3.4), of which $\sim 50\%$ is then reflected towards the polarisation state analysis arm. The polarisation state analyser arm

---

[3] The beam diameter used depended on the Fresnel cone being used, either 10, 15 or 25 mm depending on the generation of cone.

of the system consists of a pair of imaging lenses and a horizontally aligned linear polariser, producing an intensity pattern on the camera for analysis.

In the case described above, the device is only $\sim 25\%$ efficient due to the two passes through the non-polarising beam-splitter, however, high efficiency Fresnel cone coupling ($\sim$ 100%) has since been investigated as was explained in subsection 3.4.1. This could likely be applied to this device, though has not yet been tested.

5.3.3 Stokes vector recovery

In this section I will first describe the details of how to recover the full Stokes vector given an ideal system with perfect optical components. I will then go into detail on the differences that less-than-ideal optical components introduce to the analysis. Equation 5.12 contains the four initial Stokes parameters S_0, S_1, S_2 and S_3, so the initial full Stokes vector can be recovered by solving Equation 5.12 for a minimum of at least four experimental θ_i measurements[4]. To do this, Equation 5.12 is a truncated Fourier series in θ_i as

$$I(\theta_i) = \frac{1}{2}\Big[a_0 + b_2\sin(2\theta_i) + a_4\cos(4\theta_i) + b_4\sin(4\theta_i)\Big], \tag{5.13}$$

where a_0, b_2, a_4 and b_4 are the discrete Fourier coefficients, which, for N discrete angles are

$$a_0 = S_0 + \frac{S_1}{2} = \frac{2}{N}\sum_{i=1}^{N} I_i, \tag{5.14}$$

$$b_2 = -S_3 = \frac{4}{N}\sum_{i=1}^{N} I_i\sin(2\theta_i), \tag{5.15}$$

$$a_4 = \frac{S_1}{2} = \frac{4}{N}\sum_{i=1}^{N} I_i\cos(4\theta_i) \text{ and} \tag{5.16}$$

$$b_4 = \frac{S_2}{2} = \frac{4}{N}\sum_{i=1}^{N} I_i\sin(4\theta_i). \tag{5.17}$$

After background correction and normalisation image processing steps of the measured cone intensity pattern (of which I will go into more detail shortly), Fourier analysis can be applied to the intensity signal $I(\theta)$ by performing a Fast Fourier

---

[4] Where θ_i corresponds to the i^{th} azimuthal angle around the cone tip.

transform to provide values corresponding to the right hand side of Equations 5.15-5.18. These four equations can be expressed in matrix form as

$$\underbrace{\begin{bmatrix} 1 & \frac{1}{2} & 0 & 0 \\ 0 & 0 & 0 & -\frac{1}{2} \\ 0 & \frac{1}{2} & 0 & 0 \\ 0 & 0 & \frac{1}{2} & 0 \end{bmatrix}}_{\mathbf{M}} \underbrace{\begin{bmatrix} S_0 \\ S_1 \\ S_2 \\ S_3 \end{bmatrix}}_{\mathbf{S}} = \underbrace{\begin{bmatrix} a_0 \\ b_2 \\ a_4 \\ b_4 \end{bmatrix}}_{\mathbf{C}} . \tag{5.18}$$

The matrix **M** is known from theory and the vector **C** is obtained from Fourier analysis of measured data, so by multiplying both sides of Equation 5.18 by $\mathbf{M}^{-1}$, the result is

$$\mathbf{S} = \mathbf{M}^{\text{-}\mathbf{1}}\mathbf{C}, \tag{5.19}$$

and the initial Stokes vector **S** can be found.

This analysis is true for systems which contain ideal optical components that do not diattenuate[5], deflect or retard an incident beam. In reality however, many optical components, such as the 50:50 non-polarising beam-splitter in the Fresnel cone polarimeter setup, can cause detrimental phase shifts or diattenuation, leading to a deviation of the experimental Mueller matrix from its theoretical form **M**.

In subsection 2.3.4 I show that it is possible to measure the experimental Mueller matrix of an optical component (or series thereof) by following the steps detailed in [69]. A total of 36 intensity measurements are made in order to construct a Mueller matrix by generating and analysing in the six polarisation basis states, H, V, A, D, R and L. As there are only 16 unknown values in a Mueller matrix in theory it is possible to measure a Mueller matrix from only 16 experimental measurements, however, the focus of this work is Stokes polarimetry and I will not go further into this here. When taking experimental measurements to determine the Mueller matrix, due to measurement noise and imprecisely calibrated components (wave plates, polarisers etc.), the Stokes vector recovery shown above can return non-physical Stokes vectors without careful normalisation of the 4 × 4 experimental Mueller matrix[6]. I chose to follow the Mueller matrix normalisation described in [163] to avoid non-physical Mueller matrices, where it is shown that the matrix

---

[5] A differential absorption of light polarised parallel and perpendicular to an orientation axis.

[6] Note that this normalisation does not correct for errors in the result from incorrect components, it only coerces any non-physical Stokes parameters to be their closest physically realisable value.

for an optical component can be parameterised as

$$\mathbf{M} = \begin{bmatrix} 1 & a & b & 0 \\ a & u & v & -x \\ b & v & w & y \\ 0 & x & -y & p \end{bmatrix}, \tag{5.20}$$

where

$$\begin{gathered} p = \sin(2\psi)\cos(\delta) \cong 0, \\ r = \sin(2\psi)\sin(\delta) \cong 1, \\ s = \cos(2\psi) \cong 0, \\ a = s\cos(2C), \\ u = f\cos(4C) + (1-f), \\ b = s\sin(2C), \\ v = f\sin(4C), \\ x = r\sin(2C), \\ w = -f\cos(4C) + (1-f), \\ y = r\cos(2C), \\ \text{and } f = (1-p)/2 \backsimeq 0.5. \end{gathered} \tag{5.21}$$

It is important to note that this normalisation method assumes no depolarisation (loss of polarisation) or diattenuation (differential absorption of s and p polarised light) in the optical component under investigation and that it is possible to parameterise the Mueller matrix by three angles, namely a phase-shift induced between s and p polarisation components (δ), a rotation of the linear polarisation components (ψ), and an orientation of the optical component from the horizontal (C). I choose to calculate the above matrix $\mathbf{M}$ for 300 values of the three angles (δ, ψ and C) ranging from 0 to π. I then determine the sum of the squared difference between each calculated Mueller matrix and my experimentally measured matrix, and select the matrix with the smallest difference to be the normalised Mueller matrix representing the real system.

The effects of the imperfect non-polarising 50:50 beam-splitter can be accounted for by including the beam-splitter transmission ($\mathbf{B}_{\text{trans}}$) and reflection ($\mathbf{B}_{\text{refl}}$) in the Mueller matrix equation representing the system, which now becomes

$$\mathbf{S'} = \mathbf{M}_{\text{pol}}\mathbf{B}_{\text{refl}}\mathbf{R}(-\theta)\mathbf{M}_{\text{wedge}}\mathbf{R}\mathbf{B}_{\text{trans}}(\theta)\mathbf{S}. \tag{5.22}$$

I carried out experimental Mueller matrix measurements to find $\mathbf{B}_{\text{refl}}$ and $\mathbf{B}_{\text{trans}}$ for each of the red, green and blue colour channels separately as I aimed to demonstrate the broadband operation of the Fresnel cone polarimeter using white light and a colour CCD camera. Using the normalised versions of these experimental Mueller matrices in the analysis results in $\mathbf{M}$ in Equation 5.18 becoming a 5×4 matrix rather than a 4×4 matrix, and $\mathbf{C}$ in Equation 5.18 gaining an additional term. As an example of one such case, for the red frequency band Equation 5.18 becomes

$$\underbrace{\begin{bmatrix} \frac{31}{237} & \frac{52}{1301} & -\frac{1}{23754} & \frac{1}{1176} \\ \frac{1}{10822} & -\frac{1}{38210} & -\frac{1}{300} & -\frac{1}{430} \\ \frac{1}{460} & \frac{1}{1453} & -\frac{5}{203} & -\frac{9}{118} \\ \frac{1}{1944} & \frac{22}{551} & \frac{1}{322} & \frac{1}{6482} \\ -\frac{1}{1452} & -\frac{1}{480} & \frac{13}{310} & -\frac{3}{322} \end{bmatrix}}_{\mathbf{M}} \underbrace{\begin{bmatrix} s_0 \\ s_1 \\ s_2 \\ s_3 \end{bmatrix}}_{\mathbf{S}} = \underbrace{\begin{bmatrix} a_0 \\ a_2 \\ b_2 \\ a_4 \\ b_4 \end{bmatrix}}_{\mathbf{C}}, \tag{5.23}$$

where the a_2 Fourier component has emerged and is

$$a_2 = \frac{4}{N} \sum_{i=1}^{N} I_i \cos 2\theta_i. \tag{5.24}$$

The set of linear equations is now over-determined as there are five equations with just four unknown values. This results in the matrix $\mathbf{M}$ no longer being a square 4×4 matrix and so the pseudo-inverse of $\mathbf{M}$ must be used. This is calculated by using an in-built LabVIEW function, based on the singular value decomposition method.

5.3.4 Results and discussion

The experimental setup for the Fresnel cone polarimeter is shown in Figure 5.4, where the actual polarimeter device is shown in the blue box and the green box encompasses the optical setup used to generate desired input states for testing. As mentioned, different input polarisation states to the polarimeter generate different intensity patterns on the camera, such as those shown in Figure 5.3. For calibration I first record a background image with the light source powered off, which is subtracted from the intensity pattern data images to reduce background noise. I also record two images for normalisation - one with the analyser-arm linear polariser horizontally aligned and one where it is vertically aligned. The intensity pattern data images are normalised to the sum of these two images, to reduce local intensity modulations present within the input beam which would lead to deterioration of the Fourier signal.

Figure 5.5 shows an example of how the data images are processed ready for Fourier analysis. In Figure 5.5a), a data image has been background corrected and normalised (as explained above) where a region of interest (ROI) is highlighted which will later be cropped to avoid the central tip area. This central tip area is often noisy due to insufficient manufacturing capability to acquire a fine cone tip. This image is then unwrapped from an x-y Cartesian coordinate system to an r-θ polar coordinate system, where the result of this is shown in Figure 5.5b). The resulting ROI is shown in Figure 5.5c), where it can be seen that as expected the intensity varies only azimuthally and appears constant radially. This feature can be used to reduce the error from noise in the system by averaging the $I(\theta)$ values radially. I note here that the resolution appears lower at smaller radii in Figure 5.5b) and c) due to an artifact of the coordinate transformation.

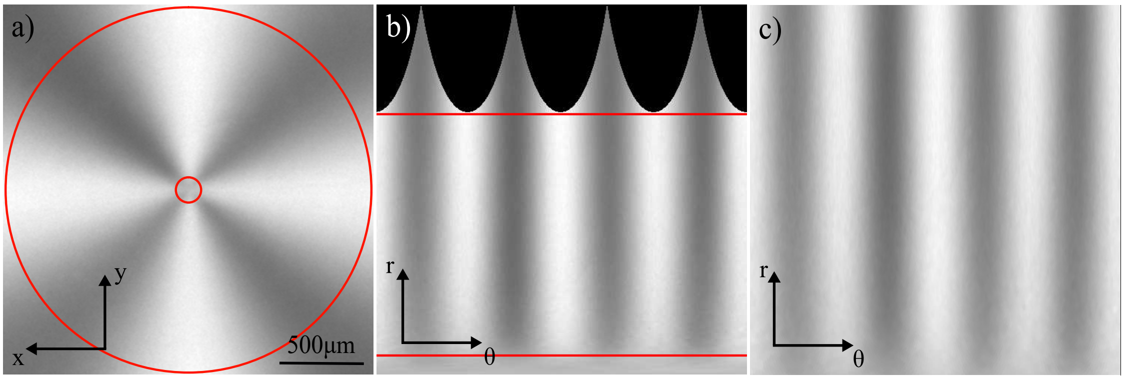

FIGURE 5.5: This is an example of how data images are processed ready for the Fourier analysis. In this case the intensity pattern is for an input of horizontally polarised light. a) shows cone intensity image in x-y coordinate system with ROI highlighted, b) shows cone intensity image unwrapped to r-θ coordinate system, c) shows resulting ROI cropped in r-θ. Image adapted from [130].

An example of the resulting averaged one-dimensional intensity profile is shown below in Figure 5.6 for the data example shown in Figure 5.5c). This intensity profile is $I(\theta_i)$ in Equation 5.13, from which a Fast Fourier Transform (FFT) is performed in order to extract the Fourier coefficients a_0, a_2, b_2, a_4 and b_4 (elements of C in Equation 5.23).

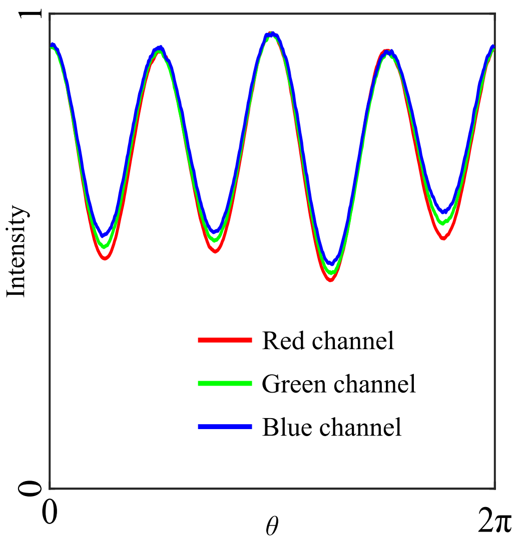

Figure 5.6: An example of the averaged radial intensity profile for the red, green and blue colour channels individually. The y-axis shows normalised intensity and x-axis shows azimuthal angle around the cone tip. Image adapted from [130].

To characterise the performance of the polarimeter quantitatively, I consider the polarised and unpolarised portions of the measured light independently. I evaluate the measurement of the polarised component by determining the angular accuracy of the resulting Stokes vector. This can be visualised as the difference in angle of the measured Stokes vector and the incident Stokes vector on the Poincaré sphere - described in subsection 2.3.5 and shown in Figure 5.7 below.

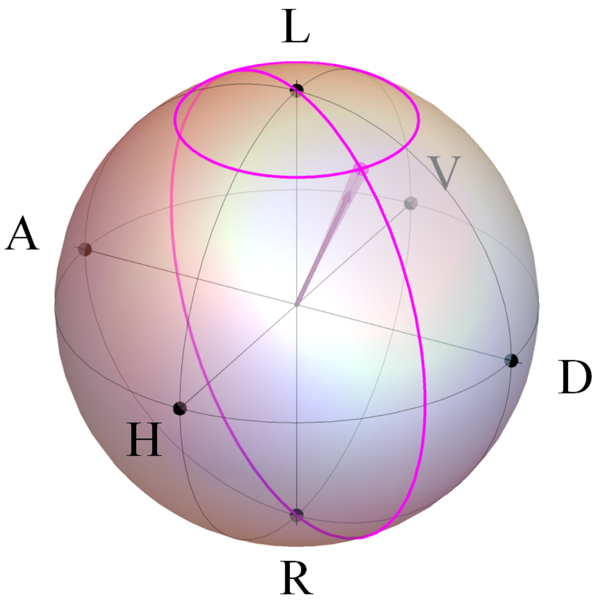

Figure 5.7: A Poincaré sphere representation of the Fresnel cone polarimeter accuracy, where the angular accuracy is shown as a solid cone and degree of polarisation is shown as the length of the vector inside the sphere. The angular accuracy in this case is set to 3.6° and the degree of polarisation is set to 0.85. Image adapted from [130].

I define the angular accuracy with the following equation,

$$\alpha = \cos^{-1}\left(\frac{\mathbf{S}_{123}\cdot\mathbf{S}'_{123}}{|\mathbf{S}_{123}||\mathbf{S}'_{123}|}\right), \tag{5.25}$$

where $\mathbf{S}_{123} = [s_1, s_2, s_3]^T$ and $\mathbf{S}'_{123} = [s'_1, s'_2, s'_3]^T$. Note that this only takes into account the angle between the direction of the theoretical incident and experimentally measured Stokes vectors and not the length of the vector (degree of polarisation) as previously stated - i.e. this is a characterisation of the performance for measuring the polarised component of the light. I characterise the performance of the unpolarised component measurement by assessing the degree of polarisation, defined as

$$\text{DOP} = \sqrt{\mathrm{s}_1'^2 + \mathrm{s}_2'^2 + \mathrm{s}_3'^2}. \tag{5.26}$$

The DOP accuracy of the polarimeter is determined by the magnitude difference of the theoretical incident and experimentally measured DOP. The characterisation of the DOP accuracy is also visualised in Figure 5.7, where the DOP is shown as the length of the Stokes vector inside the sphere.

When characterising the accuracy of the polarimeter device it is important to test it over a large range of input states. I chose to test it for two sets of inputs, firstly a set of linear polarisation states with varying orientation, and secondly a set of states with varying ellipticity. I generated the linear input states by rotating a linear polariser in front of the unpolarised light source, in increments of 5° over a 180° range. This spans the equator of the Poincaré sphere. For the elliptically polarised input states I again rotate a linear polariser in front of the unpolarised light source, followed by a horizontally aligned quarter-wave Fresnel rhomb. Again this is done in 5° increments over a 180° range and the polarisation states this system generates on the Poincaré sphere is depicted in Figure 5.8. Testing the polarimeter against these two sets of input states is not testing for all possible polarisation input states, however, it is testing for full variation of both ellipticity and orientation of major axis of the polarisation ellipse.

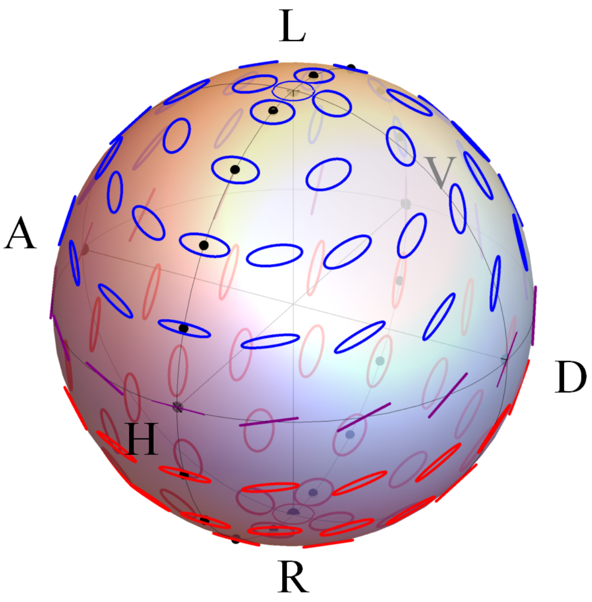

FIGURE 5.8: This Poincaré sphere diagram shows where the elliptically polarised input states lie (black dots), which are generated by rotating a linear polariser in front of a horizontally aligned quarter-wave Fresnel rhomb for characterising the polarimeter performance. Image adapted from [130].

By setting the DOP to be equal to 1, I am able to visualise the angular accuracy, where Figure 5.9 and Figure 5.10 show the theoretical and measured Stokes parameters S_1, S_2 and S_3 in this case for the two input ranges (linearly and elliptically polarised light). Also shown in these two figures are the averaged angular accuracy for these inputs.

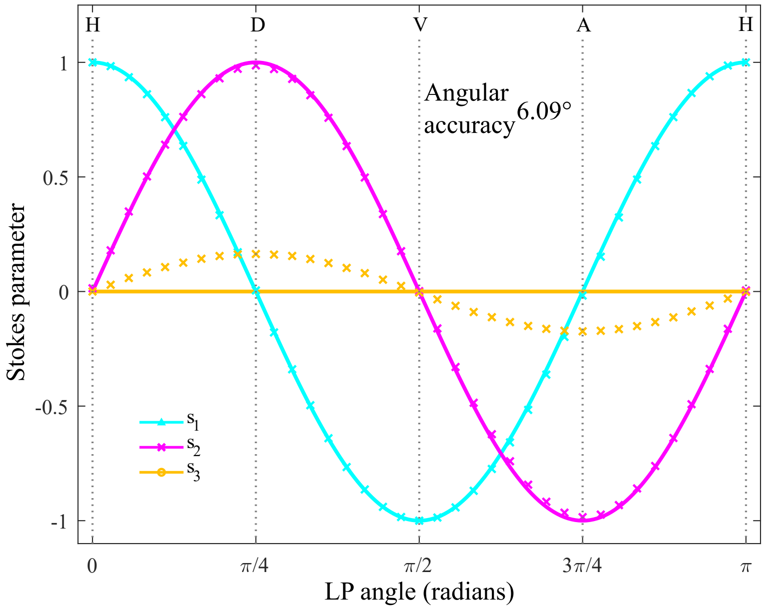

FIGURE 5.9: Demonstration of the Fresnel cone polarimeter effectiveness for measuring the Stokes parameters S_1 (cyan), S_2 (magenta) and S_3 (yellow) for linearly polarised input states. The solid line represents the ideal Stokes parameter value from theory and the markers show experimental data.

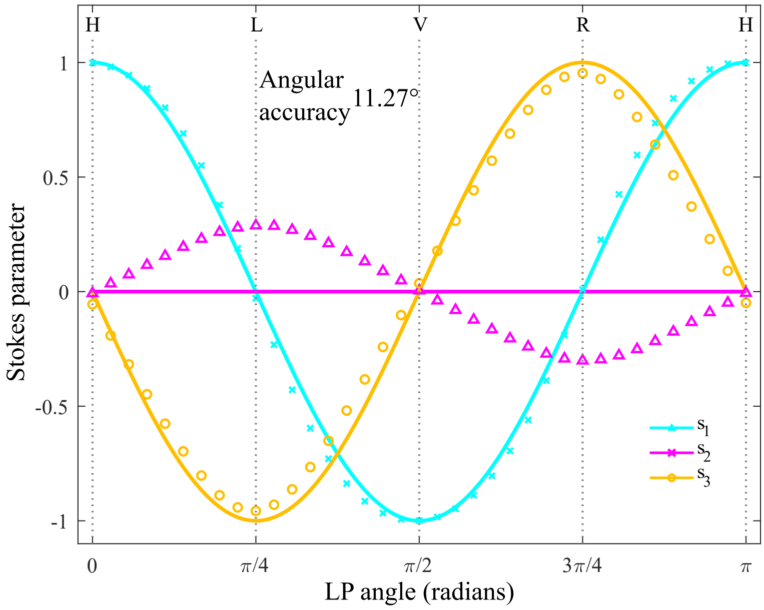

FIGURE 5.10: Demonstration of the Fresnel cone polarimeter effectiveness for measuring the Stokes parameters S_1 (cyan), S_2 (magenta) and S_3 (yellow) for elliptically polarised input states. The solid line represents the ideal Stokes parameter value from theory and the markers show experimental data.

Here I note that the Stokes vector result is actually calculated for each the red, green and blue colour channels of the camera individually in the proof of principle experiment, the angular accuracy characteristic chosen to represent the polarimeter device is an average of the angular accuracy of the red, green and blue results.

Certain optical components chosen for this experiment, such as the non-polarising beam-splitter, are suggested for operation across a broad wavelength range (encompassing the visible spectrum in this case), however, these components can still possess slight frequency dependencies. Hence in order to enhance the accuracy of the technique, I performed full Mueller matrix measurement of the supposed non-polarising beam-splitter in the polarimeter system for each the red, green and blue camera channels (for both the transmission and reflection). After accounting for the measured Mueller matrices, the enhanced results are shown below in figures Figure 5.11 and Figure 5.12. These show results for the same two input sets as the previous two figures. Visually inspecting the measured data points it is clear that the results are of higher accuracy, confirmed by an enhanced angular accuracy average. The achieved angular accuracy is comparable to commercial devices and suitable for applications in laser characterisation and microscopy, however, higher accuracy is likely required for space-based applications (such as in the search for life [147]).

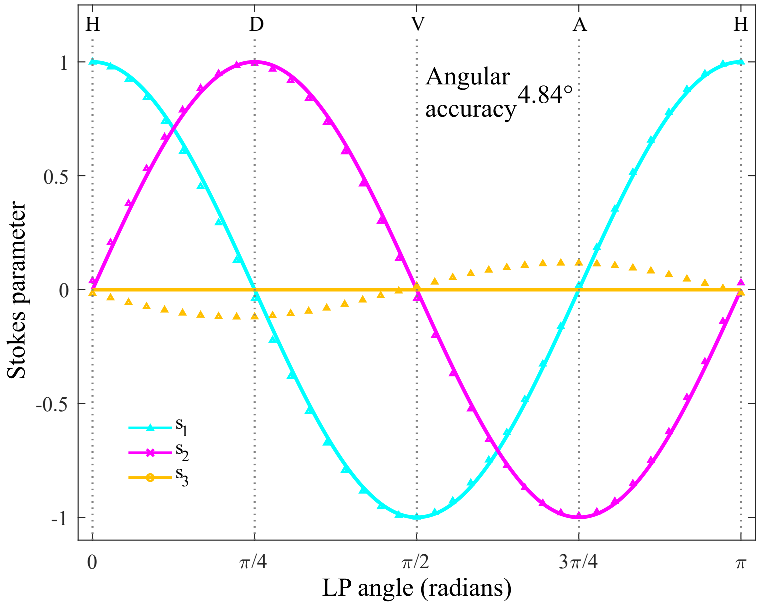

FIGURE 5.11: Demonstration of the Fresnel cone polarimeter effectiveness for measuring the Stokes parameters S_1 (cyan), S_2 (magenta) and S_3 (yellow) for linearly polarised input states, after taking into account the non-ideal beamsplitter Mueller matrices in the analysis. The solid line represents the ideal Stokes parameter value from theory and the markers show experimental data.

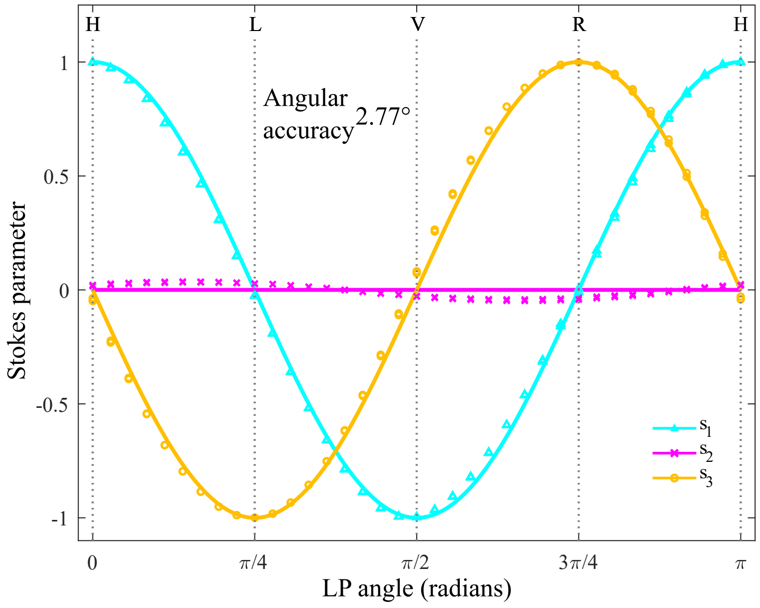

FIGURE 5.12: Demonstration of the Fresnel cone polarimeter effectiveness for measuring the Stokes parameters S_1 (cyan), S_2 (magenta) and S_3 (yellow) for elliptically polarised input states, after taking into account the non-ideal beamsplitter Mueller matrices in the analysis. The solid line represents the ideal Stokes parameter value from theory and the markers show experimental data.

I note here that from the camera intensity image of the Fresnel cone surface plane, the intensity value $I(\theta)$ for all θ values is recorded simultaneously, however, not all are needed to recover the incident Stokes vector. Stokes vector recovery could instead be achieved by accurately positioning five individual photo-diode detectors, ideally positioned at equally spaced intervals covering half of the Fresnel cone output light beam. Even though there are four unknown values, five measurements are needed to obtain the 0^{th}, 2^{nd} and 4^{th} azimuthal frequency components (required to solve the linear system such as in the example Equation 5.24). For the current Fresnel cone polarimeter setup however, by using a camera I record quasi-continuous values of $I(\theta)$, where in the analysis I use 499 values of $I(\theta)$.

In my setup I use a colour camera (Thorlabs DCC1645C) from which I obtain 24-bit colour images of the Fresnel cone intensity pattern. From these images I can obtain an 8-bit colour image for the red, green and blue channels, which allows me to observe the polarimeter performance in the visible wavelength range to demonstrate the broadband nature of the device, as shown in Figure 5.13. Here I note that the experimental Mueller matrices $\mathbf{B}_{\text{trans}}$ and $\mathbf{B}_{\text{refl}}$ were each measured for the red, green and blue colour channels, so that during the analysis of the three individual 8-bit colour images these could each be applied to enhance accuracy.

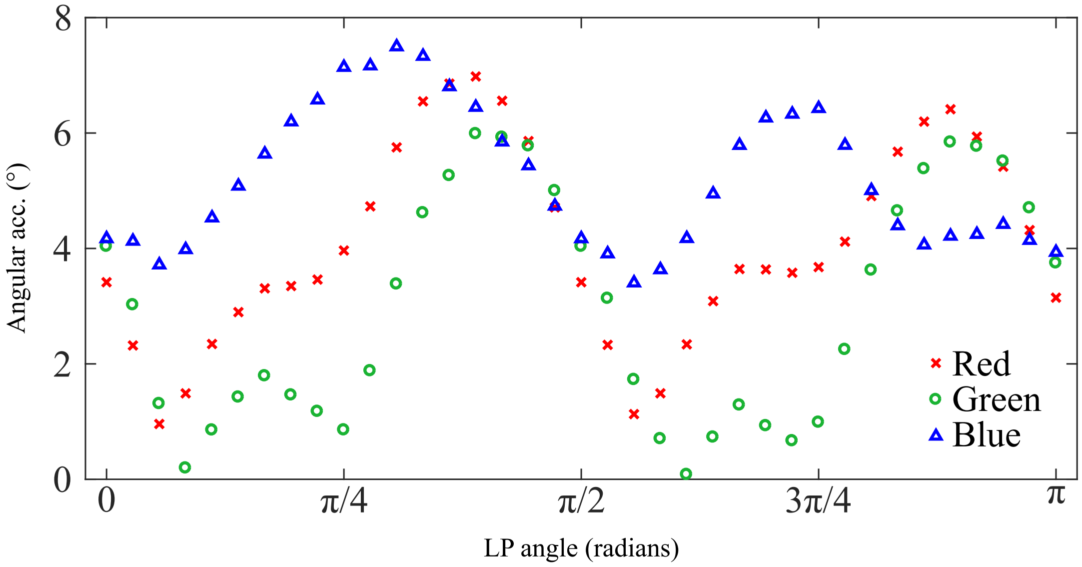

FIGURE 5.13: This figure shows how the polarimeter performance is relatively consistent throughout the visible spectrum, by observing the angular accuracy for the red, green and blue colour camera channels (for elliptical input states). Image adapted from [130].

Figure 5.13 shows that there is very little deviation in the angular accuracy between the red, green and blue colour camera camera channels, providing evidence that the device operates across a broad spectrum (visible spectrum). Although, I note that the average angular accuracy is slightly worse in the blue frequency which is attributed to the anti-reflection coating of the beam-splitter in the system being less efficient at this frequency. Furthermore, although other polarimeters can claim they allow broadband operation this is often through re-calibration depending on what wavelength is being investigated, while the Fresnel cone polarimeter allows simultaneous broadband operation across a broad spectrum.

The Fresnel cone imparts a total phase-shift between s and p polarisation components upon TIR of $\sim 90°$ ($\pi/2$, see section 3.3), however, it has been shown that the optimal retardance of a polarimeter of this nature to be $\sim 132°$ [164]. As the Fresnel cone can be engineered with different refractive indices depending on the type of glass used, the angular accuracy could further be enhanced by manufacturing a Fresnel cone from LaSF9 glass, providing a refractive index of ~ 1.86 across the visible spectrum and a phase-shift of $\sim 132°$.

5.4 Conclusions

In this chapter I demonstrated the use of a Fresnel cone to measure the polarisation property of an incident light beam in a single-shot polarimeter device. I first discussed the usefulness of these devices in a number of important research areas and described some real-world applications. I showed that although the use of polarimeters is widespread, different polarimeter devices are tailored to different measurement problems.

The Fresnel cone polarimeter may be beneficial where true broadband polarimetry is required, as it is capable of performing Stokes measurements simultaneously across a broad spectrum. Often commercial polarimeters that claim broadband operation rely on re-calibration of the system depending on the wavelength being used. Another area where the Fresnel cone polarimeter may be beneficial is for applications in space, as it contains no moving parts and is relatively robust. The proof of principle device I demonstrated in this chapter relies on the incident polarisation state to be uniform across the cone front surface (if not, the result will be an average). As the incident polarisation must be uniform, this does not allow imaging polarimetry with this device, however, it could be possible if coupled with a scanning technique such as confocal or two-photon microscopy.

Future work could involve enhancing the accuracy and speed of the Fresnel cone polarimeter, the development of a Mueller matrix polarimeter technique and testing with ultra-short pulse high power lasers. These thoughts will be discussed more in chapter 6.

Chapter 6

Conclusions

'All you really need to know for the moment is that the universe is a lot more complicated than you might think, even if you start from a position of thinking it's pretty damn complicated in the first place.' - Douglas Adams

In this chapter I will first summarise my thesis, highlighting the enhancements made to the original experiment, my main findings for uses of Fresnel cone vector beams in tight focussing and single-shot polarimetry, and the potential impact of the work. I will then discuss future work for these projects that follows from the results of this thesis.

6.1 Thesis summary

I was first introduced to the Fresnel cone during a short Master's project, where I worked on an experiment devised to measure the polarisation structures generated through its use. This was for the most part an investigation of curiosity, to investigate what was possible. Following this short project it became apparent that certain beams generated by a Fresnel cone could be useful in technology. Thus, I began my PhD research in an attempt to exploit this Fresnel cone polarisation structuring for application in both microscopy and polarimetry.

Following necessary background and theoretical considerations in chapter 2, in chapter 3 I showed the theory and experimental technique of Fresnel cone polarisation structuring. I first presented results showing improved polarisation fidelity of the well-known radial and azimuthal polarisation states, since the original publication in 2016 [46]. I then detailed an experiment devised to enhance the efficiency of the coupling of light into and out of a Fresnel cone, which was previously restricted to a maximum of 25%. This new coupling technique allows in theory an efficiency of 100%, and was measured experimentally to be $\sim$ 83%. Reasons for not reaching the theoretical value were discussed, concluding higher efficiency should be possible if more suitable optical components with anti-reflection coating are used. Not only does this coupling method allow high efficiency, but generates a high NA annular beam profile, potentially useful for microscopy applications. I showed results for the annular beam intensity generated as well as confirming generation of radial and azimuthal polarisation states is still possible. A manuscript is currently in preparation to report on the new axicon-based coupling technique.

In chapter 4, I showed results from simulation where I confirmed that the azimuthally polarised beam generated using a Fresnel cone can focus below that of both conventional circular and radial polarised beams. Through further simulation, I investigated the effects on focal spot for increasing centre-stop radius at the objective aperture, showing that the spot size for a radial beam approaches that of the Fresnel cone azimuthal for the increasing radius. Unfortunately, practically major issues were encountered when focussing the Fresnel cone beams, which appeared visually distorted, noisy and much larger than expected (true even for low-NA focussing). To investigate, I devised an interferometry experiment to obtain fringe patterns from a Fresnel cone beam overlapped with a reference beam. Using these fringe patterns and Fourier analysis techniques, I discovered raised elevations on the physical Fresnel cone surface. I further showed through simulations that distortions to the phase of the generated beam of this nature can be detrimental to the focussing properties. Aspects of this work, including an experimental technique developed to pre-compensate a vector beam for transmission through a microscope system, were presented in SPIE proceedings for the Photonics Europe 2020 event [62].

In chapter 5, I established the importance of polarisation characterisation - discussing the recent literature on polarimetry techniques and applications. I then presented the details of a proof of principle experiment where I show that a Fresnel cone can be used in a simple polarimeter setup to achieve single-shot full Stokes polarimetry. I showed that theoretically the Stokes recovery operation of the device reveals the Fresnel cone polarimeter to be a spatial analogue to the popular rotating wave-plate technique. Not only this, but compared to temporally modulated techniques the Fresnel cone approach is robust, low-cost and allows broadband operation. I note that the potential drawback of the system is the requirement for uniformly polarised light across the input to the cone, limiting its use in imaging polarimetry to scanning systems. This work was presented in a Scientific Reports publication in 2019 [130].

6.2 Future work

Following from the experiments performed to generate various beams using the Fresnel cone, further investigation could be carried out on the propagation of these beams. For all the experiments reported on in this thesis, the plane of the Fresnel cone surface is imaged to a camera plane and so propagation of the cone-beam is not relevant. As discussed in chapter 3, when circularly polarised light is back-reflected from a Fresnel cone, the generated beam contains $2\hbar$ units of OAM in one circular component and none in the other. These two components do not propagate in the same way, with the component possessing OAM diverging at a greater rate than the other. Preliminary simulations have shown that after a sufficient propagation distance, a full Poincaré beam is found. These beams possess simultaneously all polarisation states spanning the surface of the Poincaré sphere, and may be useful in polarimetry or more fundamental investigations.

Though eventually there were implications in the practical realisation of strongly focussed Fresnel cone beams, these Fresnel cone beams could be generated artificially using a spatial light modulator system for validation of the focussing properties. These techniques however are inherently low-efficiency for vector beam generation and would not suit application in a real microscope system. Alternatively, given that the topology of the Fresnel cone was measured in chapter 4, the associated phase aberrations could perhaps be pre-compensated for using a spatial light modulator and polarisation structuring still performed using a Fresnel cone. Combined with the newly developed axicon coupling technique, high efficiency annular vector vortex beams that have been phase-corrected for focussing could be achieved.

Following the proof-of-principle Fresnel cone polarimeter experiment reported in chapter 5, funding has been secured to continue this work in the form of an Impact Acceleration Account - an award to support impact generation from research funded by the Engineering and Physical Sciences Research Council (EPSRC) and knowledge exchange. This is currently a six month project with the primary aim of building a compact demonstrator of the Fresnel cone polarimeter to take to companies and industry exhibits. During this time, recent knowledge gained in high efficiency Fresnel cone coupling and polarimeter accuracy will be applied to the demonstrator. The use of carefully positioned photo-diodes instead of the camera in the polarimetry setup will be investigated to enhance speed, as well as making the software more efficient and user interface more stream-lined. A number of industry and academic partners are involved in the project, including an optical component specialist who will assist with the optics, a laser development company for testing with high-power lasers, as well as a cancer research institute for testing with ultra-short pulse lasers in a biomedical research environment. Funding has also been secured to travel with the demonstrator to industry exhibit events, however, this is dependent on travel restrictions due to the global pandemic.

Progressing on from Stokes vector measurement, devices that can measure the full Mueller matrix of a sample are also desirable, for biomedical research, diagnosis and in the field of chemistry to name a few. While a Stokes vector uses a dynamic polarisation state analyser to perform multiple polarisation measurements, a Mueller matrix polarimeter would also require a dynamic polarisation state generator for input to a sample. I have shown that the Fresnel cone can act as a single-shot polarisation state analyser for Stokes measurement, however, the requirement of Mueller matrix measurement for each generated state to be analysed by numerous polarisation state analysers does not allow a Fresnel cone to also be used as the generation source. An additional degree of freedom is needed here, and perhaps the use of a graded-index (GRIN) lens provides this, as these components possess a radially varying phase-shift magnitude. This was previously considered an unwanted artifact of the manufacturing process but is recently providing fruitful for vector beam generation [81, 165].

6.3 Final thoughts

The field of structured light has grown drastically in the recent decades, from structuring simple two-dimensional intensity patterns in a single plane to control over amplitude, phase and polarisation in three-dimensions - for example, the optical polarisation Mobius strip [166]. Availability of technology such as spatial light modulators (and research into new ways to exploit this technology) is fuelling research into fundamental physics, such as experimentation with cold atoms and the study of classical analogues to quantum systems, as well as in practical application. Developments in the areas of imaging and microscopy are also expected, where challenges are not only with resolution limits due to diffraction (as was highlighted in this thesis), but also in deep imaging through scattering media - such as tissue samples. Complementary to the various methods developed for generating these beams, techniques for detection are also an area of active study.

Simulation investigations into the amplitude and phase of longitudinal field components in a strong focussing regime provided surprising results (subsection 4.3.1). These longitudinal focal field components are only recently beginning to be investigated in the community [123] - such as the azimuthal phase variation of the longitudinal field component of a radially polarised vector vortex beam. Further research into these fields that result from the complicated interference that occurs in the focussing volume of a strong lens is desirable, though in this early stage currently lacks potential application. Conversely, there may be value in considering the shaping of the orthogonal magnetic field component in these cases, perhaps for uses in the field of condensed matter physics.

Many demonstrations of the interesting effects of structured light are currently found only as large experiments on optical research tables, it is anticipated that the near future will see miniaturisation of these systems and industrial implementation [26]. While many structured light systems rely on complicated devices, expensive nanofabrication abilities and extended complex optical setups, simple solutions are still discovered today - such as the vector vortex beam generation, and single-shot polarisation detection, from a simple glass cone [46, 130].

Bibliography

[1] Olivier Darrigol. *A History of Optics from Greek Antiquity to the Nineteenth Century.* OUP Oxford, illustrated edition, 2012.

[2] Brian A Curran. *Encyclopaedia of the History of Science, Technology, and Medicine in Non-Western Cultures.* 2016.

[3] Engel Sluiter. The Telescope Before Galileo. *Journal for the History of Astronomy*, 28(3):223–234, 1997.

[4] William Swindell. *Polarized Light.* John Wiley & Sons Inc, 1975.

[5] R. M. A. Azzam. The intertwined history of polarimetry and ellipsometry. *Thin Solid Films*, 519(9):2584–2588, 2011.

[6] Eugene Hecht. *Optics.* Addison-Wesley, 4th edition, 2001.

[7] S. A. Empedocles, R. Neuhauser, and M. G. Bawendi. Three-dimensional orientation measurements of symmetric single chromophores using polarization microscopy. *Nature*, 399(6732):126–130, 1999.

[8] J. Scott Tyo, Dennis L. Goldstein, David B. Chenault, and Joseph A. Shaw. Review of passive imaging polarimetry for remote sensing applications. *Applied Optics*, 45(22):5453, 2006.

[9] Stefan Richtberg and Raimund Girwidz. Use of Linear and Circular Polarization: The Secret LCD Screen and 3D Cinema. *The Physics Teacher*, 55(7):406–408, 2017.

[10] Yan Han and Guifang Li. Coherent optical communication using polarization multiple-input-multiple-output. *Optics Express*, 13(19):7527, 2005.

[11] T. Scharf, K. Puthankovilakam, J. Bernasconi, M. Kim, H. P. Herzig, U. Vogler, A. Bramati, and R. Völkel. Lightfields behind amplitude and

phase masks applications in high resolution proximity lithography. In *2015 14th Workshop on Information Optics (WIO)*, pages 1–3, 2015.

[12] Lóránd Kelemen, Sándor Valkai, and Pál Ormos. Parallel photopolymerisation with complex light patterns generated by diffractive optical elements. *Optics Express*, 15(22):14488, 2007.

[13] M. V. Berry and S. Klein. Integer, fractional and fractal Talbot effects. *Journal of Modern Optics*, 43(10):2139–2164, 1996.

[14] Jianming Wen, Yong Zhang, and Min Xiao. The Talbot effect: recent advances in classical optics, nonlinear optics, and quantum optics. *Advances in Optics and Photonics*, 5(1):83, 2013.

[15] L. Allen, S.M. Barnett, and M.J. Padgett. *Optical Angular Momentum.* Optics and Optoelectronics. Institute of Physics Publishing, Bristol, UK, March 2003.

[16] J. Arlt and M. J. Padgett. Generation of a beam with a dark focus surrounded by regions of higher intensity:the optical bottle beam. *Opt. Lett.*, 25(4):191–193, Feb 2000.

[17] S. Franke-Arnold, J. Leach, M. J. Padgett, V. E. Lembessis, D. Ellinas, A. J. Wright, J. M. Girkin, P. Öhberg, and A. S. Arnold. Optical ferris wheel for ultracold atoms. *Optics InfoBase Conference Papers*, 15(14):169–175, 2007.

[18] Jonathan Leach, Mark R. Dennis, Johannes Courtial, and Miles J. Padgett. Knotted threads of darkness. *Nature*, 432(7014):166–166, 2004.

[19] Alan E. Willner, Hao Huang, Yan Yan, Yongxiong Ren, Nisar Ahmed, Goudong Xie, Changjing Bao, Z. Zhao, Long Li, Yinwen Cao, Jian Wang, Martin Lavery, Mosche Tur, Siddharth Ramachandram, Andrew F. Molisch, Nima Ashrafi, and Solyman Ashrafi. Optical communications using orbital angular momentum beams. *Advances in Optics and Photonics*, 7(1):66–106, March 2015.

[20] Miles Padgett and Richard Bowman. Tweezers with a twist. *Nature Photonics*, 5(6):343–348, 2011.

[21] Filippo Cardano, Ebrahim Karimi, Sergei Slussarenko, Lorenzo Marrucci, Corrado de Lisio, and Enrico Santamato. Polarization pattern of vector vortex beams generated by q-plates with different topological charges. *Appl. Opt.*, 51(10):C1–C6, Apr 2012.

[22] Melanie McLaren, Thomas Konrad, and Andrew Forbes. Measuring the non-separability of vector vortex beams. *Phys. Rev. A*, 92:023833, Aug 2015.

[23] Ebrahim Karimi and Robert W. Boyd. Classical entanglement? *Science*, 350(6265):1172–1173, 2015.

[24] E. Karimi and R. W. Boyd. Physics. classical entanglement? *Science*, 350(6265):1172–3, 2015.

[25] Qiwen Zhan. Cylindrical vector beams: from mathematical concepts to applications. *Advances in Optics and Photonics*, 1(1):1, 2009.

[26] Halina Rubinsztein-Dunlop, Andrew Forbes, M. V. Berry, M. R. Dennis, David L. Andrews, Masud Mansuripur, Cornelia Denz, Christina Alpmann, Peter Banzer, Thomas Bauer, Ebrahim Karimi, Lorenzo Marrucci, Miles Padgett, Monika Ritsch-Marte, Natalia M. Litchinitser, Nicholas P. Bigelow, C. Rosales-Guzmán, A. Belmonte, J. P. Torres, Tyler W. Neely, Mark Baker, Reuven Gordon, Alexander B. Stilgoe, Jacquiline Romero, Andrew G. White, Robert Fickler, Alan E. Willner, Guodong Xie, Benjamin McMorran, and Andrew M. Weiner. Roadmap on structured light. *Journal of Optics (United Kingdom)*, 19(1), 2017.

[27] Andrew Forbes, Michael de Oliveira, and Mark R. Dennis. Structured Light. *Nature Photonics*, 15(April):253–262, 2021.

[28] Thomas W. Clark, Rachel F. Offer, Sonja Franke-Arnold, Aidan S. Arnold, and Neal Radwell. Comparison of beam generation techniques using a phase only spatial light modulator. *Optics Express*, 24(6):6249, 2016.

[29] Grigory Lazarev, Po-Ju Chen, Johannes Strauss, Nicolas Fontaine, and Andrew Forbes. Beyond the display: phase-only liquid crystal on Silicon devices and their applications in photonics [Invited]. *Optics Express*, 27(11):16206, 2019.

[30] Stirling Scholes, Ravin Kara, Jonathan Pinnell, Valeria Rodríguez-Fajardo, and Andrew Forbes. Structured light with digital micromirror devices: a guide to best practice. *Optical Engineering*, 59(4):1 – 12, 2019.

[31] Carmelo Rosales-Guzmán, Xiao Bo Hu, Adam Selyem, Pedro Moreno-Acosta, Sonja Franke-Arnold, Ruben Ramos-Garcia, and Andrew Forbes.

Polarisation-insensitive generation of complex vector modes from a digital micromirror device. *Scientific Reports*, 10(1):1–9, 2020.

[32] Bruno Piccirillo, Vincenzo D'Ambrosio, Sergei Slussarenko, Lorenzo Marrucci, and Enrico Santamato. Photon spin-to-orbital angular momentum conversion via an electrically tunable q -plate. *Applied Physics Letters*, 97(24):4085–4090, 2010.

[33] Andrew Forbes. Structured Light from Lasers. *Laser and Photonics Reviews*, 13(11):1–19, 2019.

[34] M. F. Andersen, C. Ryu, Pierre Cladé, Vasant Natarajan, A. Vaziri, K. Helmerson, and W. D. Phillips. Quantized rotation of atoms from photons with orbital angular momentum. *Phys. Rev. Lett.*, 97:170406, Oct 2006.

[35] K. C. Wright, L. S. Leslie, and N. P. Bigelow. Optical control of the internal and external angular momentum of a bose-einstein condensate. *Phys. Rev. A*, 77:041601, Apr 2008.

[36] N. Radwell, G. Walker, and S. Franke-Arnold. Cold-atom densities of more than 10^{12} cm^{-3} in a holographically shaped dark spontaneous-force optical trap. *Phys. Rev. A*, 88:043409, Oct 2013.

[37] Matthew P. Edgar, Graham M. Gibson, Richard W. Bowman, Baoqing Sun, Neal Radwell, Kevin J. Mitchell, Stephen S. Welsh, and Miles J. Padgett. Simultaneous real-time visible and infrared video with single-pixel detectors. *Scientific Reports*, 5:1–8, 2015.

[38] A. Nicolas, L. Veissier, L. Giner, E. Giacobino, D. Maxein, and J. Laurat. A quantum memory for orbital angular momentum photonic qubits. *Nature Photonics*, 8(3):234–238, 2014.

[39] Aniceto Belmonte, Carmelo Rosales-Guzmán, and Juan P. Torres. Measurement of flow vorticity with helical beams of light. *Optica*, 2(11):1002, 2015.

[40] Stefan W. Hell and Jan Wichmann. Breaking the diffraction resolution limit by stimulated emission: stimulated-emission-depletion fluorescence microscopy. *Opt. Lett.*, 19(11):780–782, Jun 1994.

[41] Jeeva Anandan. The geometric phase. *Nature*, 360(6402):307–313, 1992.

[42] L. Marrucci, C. Manzo, and D. Paparo. Pancharatnam-Berry phase optical elements for wave front shaping in the visible domain: Switchable helical mode generation. *Applied Physics Letters*, 88(22):1–4, 2006.

[43] M. V. Berry. Quantal phase factors accompanying adiabatic changes. *A Half-Century of Physical Asymptotics and Other Diversions*, 57:72–84, 1984.

[44] Xingjie Ni, Alexander V. Kildishev, and Vladimir M. Shalaev. Metasurface holograms for visible light. *Nature Communications*, 4, 2013.

[45] Tao Zhan, Jianghao Xiong, Yun-Han Lee, Ran Chen, and Shin-Tson Wu. Fabrication of Pancharatnam-Berry phase optical elements with highly stable polarization holography. *Optics Express*, 27(3):2632, 2019.

[46] N. Radwell, R. D. Hawley, J. B. Götte, and S. Franke-Arnold. Achromatic vector vortex beams from a glass cone. *Nature Communications*, 7:10564, 2016.

[47] B Richards and E Wolf. Electromagnetic diffraction in optical systems II. Structure of the image field in an aplanatic system. *Proceedings of the Royal Society of London Series a-Mathematical and Physical Sciences*, 253(1274):3580379, 1959.

[48] Lukas Novotny and Bert Hecht. *Principles of Nano-Optics*. Cambridge University Press, 2006.

[49] Ralf Dorn, Susanne Quabis, and Gerd Leuchs. The focus of light—linear polarization breaks the rotational symmetry of the focal spot. *Journal of Modern Optics*, 50(12):1917–1926, 2003.

[50] S Quabis, R Dorn, M Eberler, O. Glöckl, and G Leuchs. Focusing light to a tighter spot. *Optics Communications*, 179(1):1–7, 2000.

[51] K. S. Youngworth and T. G Brown. Focusing of high numerical aperture cylindrical-vector beams. *Optics Express*, 7(2):77, 2000.

[52] R. Dorn, S. Quabis, and G. Leuchs. Sharper focus for a radially polarized light beam. *Physical Review Letters*, 91(23):1–4, 2003.

[53] Qiwen Zhan and James Leger. Focus shaping using cylindrical vector beams. *Optics Express*, 10(7):324, 2002.

[54] Eileen Otte, Christina Alpmann, and Cornelia Denz. Tailored vectorial light fields: flower, spider web and hybrid structures. *Optical Manipulation Conference*, 10252(April 2017):102520D, 2017.

[55] Eileen Otte, Kemal Tekce, and Cornelia Denz. Tailored intensity landscapes by tight focusing of singular vector beams. *Optics Express*, 25(17):20194, 2017.

[56] Eileen Otte. *Structured Singular Light Fields*. Springer International Publishing, 2021.

[57] Xiang Hao, Cuifang Kuang, Tingting Wang, and Xu Liu. Phase encoding for sharper focus of the azimuthally polarized beam. *Opt. Lett.*, 35(23):3928–3930, Dec 2010.

[58] Qiwen Zhan. Trapping metallic Rayleigh particles with radial polarization. *Optics Express*, 12(15):3377, 2004.

[59] M. Meier, V. Romano, and T. Feurer. Material processing with pulsed radially and azimuthally polarized laser radiation. *Applied Physics A: Materials Science and Processing*, 86(3):329–334, 2007.

[60] Avner Yanai and Uriel Levy. Plasmonic focusing with coaxial illuminated by radially polarized light. *Optics InfoBase Conference Papers*, 17(2):924–932, 2008.

[61] Godofredo Bautista, Mikko J. Huttunen, Jouni Mäkitalo, Juha M. Kontio, Janne Simonen, and Martti Kauranen. Second-harmonic generation imaging of metal nano-objects with cylindrical vector beams. *Nano Letters*, 12(6):3207–3212, 2012.

[62] R. D. Hawley, R. Offer, N. Radwell, and S. Franke-Arnold. Tight focal spots using azimuthally polarised light from a Fresnel cone. In Jürgen Popp and Csilla Gergely, editors, *Biomedical Spectroscopy, Microscopy, and Imaging*, volume 11359, pages 180–186. International Society for Optics and Photonics, SPIE, 2020.

[63] Frans Snik, Julia Craven-Jones, Michael Escuti, Silvano Fineschi, David Harrington, Antonello De Martino, Dimitri Mawet, Jérôme Riedi, and J. Scott

Tyo. An overview of polarimetric sensing techniques and technology with applications to different research fields. *Polarization: Measurement, Analysis, and Remote Sensing XI*, 9099:90990B, 2014.

[64] R. M. A. Azzam and N. M. Bashara. *Ellipsometry and polarized light.* North-Holland, 1987.

[65] R. C. Jones. A New Calculus for the Treatment of Optical Systems. *Optical Society of America*, 51(I):55–236, 1941.

[66] M. J. Walker. Matrix Calculus and the Stokes Parameters of Polarized Radiation. *American Journal of Physics*, 22(4):170, 1954.

[67] José J. Gil. Interpretation of the coherency matrix for three-dimensional polarization states. *Physical Review A - Atomic, Molecular, and Optical Physics*, 90(4):1–11, 2014.

[68] William S. Bickel and Wilbur M. Bailey. Stokes vectors, Mueller matrices, and polarized scattered light. *American Journal of Physics*, 53(5):468–478, 1985.

[69] H. Fujiwara. *Spectroscopic ellipsometry: Principles and applications.* Wiley-Blackwell, 2007.

[70] Jeremy Tatum. Book: Physical Optics (Tatum), 8 2020. [Online; accessed 2021-03-19].

[71] S. Chandrasekhar. The transfer of radiation in stellar atmospheres. *Bulletin of the American Mathematical Society*, 53(7):641–711, 1947.

[72] E Wolf. Electromagnetic diffraction in optical systems, II. Structure of the image field in an aplanatic system. *Proceedings of the Royal Society of London. Series A. Mathematical and Physical Sciences*, 253(1274):358–379, 1959.

[73] K. S. Youngworth and T. G Brown. Focusing of high numerical aperture cylindrical-vector beams. *Optics Express*, 7(2):77, 2000.

[74] Carmelo Rosales-Guzmán, Bienvenu Ndagano, and Andrew Forbes. *A review of complex vector light fields and their applications.* IOP Publishing, 2018.

[75] Qiwen Zhan and James R. Leger. Microellipsometer with radial symmetry. *Appl. Opt.*, 41(22):4630–4637, Aug 2002.

[76] S. Quabis, R. Dorn, and G. Leuchs. Generation of a radially polarized doughnut mode of high quality. *Applied Physics B: Lasers and Optics*, 81(5):597–600, 2005.

[77] G Machavariani, Y Lumer, I Moshe, A Meir, and S Jackel. Efficient extracavity generation of radially and azimuthally polarized beams. 32(11):1468–1470, 2007.

[78] Psang Dain Lin. *Advanced Geometrical Optics.* Springer Singapore, 2017.

[79] Peng Chen, Wei Ji, Bing Yan Wei, Wei Hu, Vladimir Chigrinov, and Yan Qing Lu. Generation of arbitrary vector beams with liquid crystal polarization converters and vector-photoaligned q-plates. *Applied Physics Letters*, 107(24), 2015.

[80] Andrea Rubano, Filippo Cardano, Bruno Piccirillo and Lorenzo Marrucci. Q-plate technology: a progress review [Invited]. 36(5):70–87, 2019.

[81] Honghui He, Ran Liao, Nan Zeng, Pengcheng Li, Zhenhua Chen, Xi Liu, and Hui Ma. Mueller matrix polarimetry-An emerging new tool for characterizing the microstructural feature of complex biological specimen. *Journal of Lightwave Technology*, 37(11):2534–2548, 2019.

[82] Komal Kampasi, Daniel F. English, John Seymour, Eran Stark, Sam McKenzie, Mihály Vöröslakos, György Buzsáki, Kensall D. Wise, and Euisik Yoon. Dual color optogenetic control of neural populations using low-noise, multishank optoelectrodes. *Microsystems and Nanoengineering*, 4(1), 2018.

[83] David M. Huland, Christopher M. Brown, Scott S. Howard, Dimitre G. Ouzounov, Ina Pavlova, Ke Wang, David R. Rivera, Watt W. Webb, and Chris Xu. In vivo imaging of unstained tissues using long gradient index lens multiphoton endoscopic systems. *Biomed. Opt. Express*, 3(5):1077–1085, May 2012.

[84] Long Zhu and Jian Wang. Arbitrary manipulation of spatial amplitude and phase using phase-only spatial light modulators. *Scientific Reports*, 4:1–7, 2014.

[85] Eliot Bolduc, Nicolas Bent, Enrico Santamato, Ebrahim Karimi, and Robert W. Boyd. Exact solution to simultaneous intensity and phase encryption with a single phase-only hologram. *Opt. Lett.*, 38(18):3546–3549, Sep 2013.

[86] Tamás Sarkadi, Ádám Kettinger, and Pál Koppa. Spatial filters for complex wavefront modulation. *Appl. Opt.*, 52(22):5449–5454, Aug 2013.

[87] Andrey S. Ostrovsky, Carolina Rickenstorff-Parrao, and Víctor Arrizón. Generation of the perfect optical vortex using a liquid-crystal spatial light modulator. *Opt. Lett.*, 38(4):534–536, Feb 2013.

[88] Christian Maurer, Alexander Jesacher, Severin Fürhapter, Stefan Bernet, and Monika Ritsch-Marte. Tailoring of arbitrary optical vector beams. *New Journal of Physics*, 9, 2007.

[89] E. Otte, C. Alpmann, and C. Denz. Higher-order polarization singularitites in tailored vector beams. *Journal of Optics (United Kingdom)*, 18(7):1–7, 2016.

[90] Kevin J. Mitchell, Sergey Turtaev, Miles J. Padgett, Tomáš Čižmár, and David B. Phillips. High-speed spatial control of the intensity, phase and polarisation of vector beams using a digital micro-mirror device. *Opt. Express*, 24(25):29269–29282, Dec 2016.

[91] Yu Xuan Ren, Rong De Lu, and Lei Gong. Tailoring light with a digital micromirror device. *Annalen der Physik*, 527(7-8):447–470, 2015.

[92] J. Mitchell, Kevin, Sergey Turtaev, Miles J. Padgett, Tomas Cizmar, and David B. Phillips. High-speed spatial control of the intensity, phase and polarisation of vector beams using a digital micro-mirror device. *Optics Express*, 24(25), 2016.

[93] Yu-Xuan Ren, Zhao-Xiang Fang, Lei Gong, Kun Huang, Yue Chen, and Rong-De Lu. Digital generation and control of hermite–gaussian modes with an amplitude digital micromirror device. *Journal of Optics*, 17(12), 2015.

[94] H Kobayashi, K Nonaka, and M Kitano. Helical mode conversion using conical reflector. 20(13):1401–1407, 2012.

[95] Frédéric Bouchard, Harjaspreet Mand, Mohammad Mirhosseini, Ebrahim Karimi, and Robert W. Boyd. Achromatic orbital angular momentum generator. *New Journal of Physics*, 16, 2014.

[96] Toshitaka Wakayama, Kazuki Komaki, Yukitoshi Otani, and Toru Yoshizawa. Achromatic axially symmetric wave plate. *Optics Express*, 20(28):29260, 2012.

[97] Toshitaka Wakayama, Oscar G. Rodríguez-Herrera, J. Scott Tyo, Yukitoshi Otani, Motoki Yonemura, and Toru Yoshizawa. Generation of achromatic, uniform-phase, radially polarized beams. *Optics Express*, 22(3):3306, 2014.

[98] Andrey G. Sedukhin. Beam-preshaping axicon focusing. *Journal of the Optical Society of America A*, 15(12):3057, 1998.

[99] Christian Vetter, Ralf Steinkopf, Klaus Bergner, Marco Ornigotti, Stefan Nolte, Herbert Gross and Alexander Szameit. Realization of Free-Space Long-Distance Self-Healing Bessel Beams, 2019.

[100] Oto Brzobohatý, Tomáš Cižmár, and Pavel Zemánek. High quality quasi-Bessel beam generated by round-tip axicon. *Optics Express*, 16(17):12688, 2008.

[101] J. Durnin. Exact solutions for nondiffracting beams i the scalar theory. *Journal of the Optical Society of America A*, 4(4), 1987.

[102] V. G. Niziev and A. V. Nesterov. Influence of beam polarization on laser cutting efficiency. *Journal of Physics D: Applied Physics*, 32(13):1455–1461, 1999.

[103] Martin Neugebauer, Pawel Wozniak, Ankan Bag, Gerd Leuchs, and Peter Banzer. Polarization-controlled directional scattering for nanoscopic position sensing. *Nature Communications*, 48(7):829–834, 2016.

[104] J. van Zuylen. The microscopes of antoni van leeuwenhoek. *Journal of Microscopy*, 121(3):309–328, 1981.

[105] Bo Huang, Sara A. Jones, Boerries Brandenburg, and Xiaowei Zhuang. Whole-cell 3D STORM reveals interactions between cellular structures with nanometer-scale resolution. *Nature Methods*, 5(12):1047–1052, 2008.

[106] Benjamin Harke, Jan Keller, Chaitanya K. Ullal, Volker Westphal, Andreas Schönle, and Stefan W. Hell. Resolution scaling in STED microscopy. *Optics Express*, 16(6):4154, 2008.

[107] Giuseppe Vicidomini, Paolo Bianchini, and Alberto Diaspro. STED super-resolved microscopy. *Nature Methods*, 15(3):173–182, 2018.

[108] S W Hell and M Kroug. Ground-state-depletion fluorscence microscopy: a concept for breaking the diffraction resolution limit. *Applied Physics B: Lasers and Optics*, 60(7310):495–497, 1995.

[109] Shasha Chong, Wei Min, and X. Sunney Xie. Ground-state depletion microscopy: Detection sensitivity of single-molecule optical absorption at room temperature. *Journal of Physical Chemistry Letters*, 1(23):3316–3322, 2010.

[110] Joanna Oracz, Karl Adolfsson, Volker Westphal, Czesław Radzewicz, Magnus T. Borgström, Steffen J. Sahl, Christelle N. Prinz, and Stefan W. Hell. Ground State Depletion Nanoscopy Resolves Semiconductor Nanowire Barcode Segments at Room Temperature. *Nano Letters*, 17(4):2652–2659, 2017.

[111] Eric Betzig, George H. Patterson, Rachid Sougrat, O. Wolf Lindwasser, Scott Olenych, Juan S. Bonifacino, Michael W. Davidson, Jennifer Lippincott-Schwartz, and Harald F. Hess. Imaging intracellular fluorescent proteins at nanometer resolution. *Science*, 313(5793):1642–1645, 2006.

[112] Michael J. Rust, Mark Bates, and Xiaowei Zhuang. Sub-diffraction-limit imaging by stochastic optical reconstruction microscopy (STORM). *Nature Methods*, 3(10):793–795, 2006.

[113] Colin J. R. Sheppard. High-aperture beams. *J. Opt. Soc. Am. A*, 18(7):1579–1587, Jul 2001.

[114] Jia Wang, Xiaobin Wu, Rui Wang, and Mingqian Zhang. Detection of Carbon Nanotubes using Tip-Enhanced Raman Spectroscopy. *Electronic Properties of Carbon Nanotubes*, 2011.

[115] Hao Chen, Santosh Tripathi, and Kimani C Toussaint. Demonstration of flat-top focusing under radial polarization illumination. *Optics letters*, 39(4):834–7, 2014.

[116] Yi Xue, Cuifang Kuang, Shuai Li, Zhaotai Gu, and Xu Liu. Sharper fluorescent super-resolution spot generated by azimuthally polarized beam in STED microscopy. *Optics Express*, 20(16):17653, 2012.

[117] Yong Liu, Cuifang Kuang, and Xu Liu. The use of azimuthally polarized sinh-gauss beam in STED microscopy. *Journal of Optics*, 17(4):045609, mar 2015.

[118] Geon Lim, Wan-Chin Kim, and No-Cheol Park. Investigation of excitation beam modulation using azimuthal polarization to improve sted resolution. *2019 24th Microoptics Conference Proceedings (MOC)*, pages 72–73, 2019.

[119] Chen-Kuan Chou, Wei-Liang Chen, Peter Tramyeon Fwu, Sung-Jan Lin, Hsuan-Shu Lee, and Chen-Yuan Dong. Polarization ellipticity compensation in polarization second-harmonic generation microscopy without specimen rotation. *Journal of Biomedical Optics*, 13(1):014005, 2008.

[120] P. E. Mackay, Ironside-Smith J. G. Franke-Arnold, S., and N. M. Radwell. Dual cone-based polarizer. *US Patent & Trademark Office*, Patent 10248032, 2019.

[121] Mitsuo Takeda, Hideki Ina, and Seiji Kobayashi. Fourier-Transform Method of Fringe-Pattern Analysis for Computer-Based Topography and Inteferometry. *Journal of the Optical Society of America*, 72(1):156–160, 1982.

[122] S. Otahal and P. Vaclavik. Moire topography. *Lekar a Technika*, 20(4):89–93, 1989.

[123] V. V. Kotlyar, A. G. Nalimov, A. A. Kovalev, A. P. Porfirev, and S. S. Stafeev. Spin-orbit and orbit-spin conversion in the sharp focus of laser light: Theory and experiment. *Phys. Rev. A*, 102:033502, Sep 2020.

[124] Konstantin Y. Bliokh and Franco Nori. Transverse and longitudinal angular momenta of light. *Physics Reports*, 592:1–38, 2015.

[125] Nirmalya Ghosh. Tissue polarimetry: concepts, challenges, applications, and outlook. *Journal of Biomedical Optics*, 16(11):110801, 2011.

[126] Shane Robert Cloude and Eric Pettier. A review of target decomposition theorems in radar polarimetry. *IEEE Transactions on Geoscience and Remote Sensing*, 34(2):498–518, 1996.

[127] Costel Flueraru, Sofiane Latoui, Johann Besse, and Pierre Legendre. Error analysis of a rotating quarter-wave plate Stokes polarimeter. *IEEE Transactions on Instrumentation and Measurement*, 57(4):731–735, 2008.

[128] Andreas Furchner, Christoph Kratz, and Karsten Hinrichs. Sub-second infrared broadband-laser single-shot phase–amplitude polarimetry of thin films. *Opt. Lett.*, 44(17):4387–4390, Sep 2019.

[129] Mahdi Eshaghi and Aristide Dogariu. Single-shot omnidirectional stokes polarimetry. *Opt. Lett.*, 45(15):4340–4343, Aug 2020.

[130] R. D. Hawley, J. Cork, N. Radwell, and S. Franke-Arnold. Passive broadband full Stokes polarimeter using a Fresnel cone. *Scientific Reports*, 9(1):1–8, 2019.

[131] P. M. Johnson, D. A. Olson, S. Pankratz, T. Nguyen, J. Goodby, M. Hird, and C. C. Huang. Structure of the liquid-crystal ferrielectric phases as determined by ellipsometry. *Physical Review Letters*, 84(21):4870–4873, 2000.

[132] N. N. Kovaleva, A. V. Boris, C. Bernhard, A. Kulakov, A. Pimenov, A. M. Balbashov, G. Khaliullin, and B. Keimer. Spin-Controlled Mott-Hubbard Bands in $\mathrm{LaMnO_3}$ Probed by Optical Ellipsometry. *Physical Review Letters*, 93(14):147204, 2004.

[133] Maria Losurdo, Michael Bergmair, Giovanni Bruno, Denis Cattelan, Christoph Cobet, Antonello De Martino, Karsten Fleischer, Zorana Dohcevic-Mitrovic, Norbert Esser, Melanie Galliet, Rados Gajic, Dušan Hemzal, Kurt Hingerl, Josef Humlicek, Razvigor Ossikovski, Zoran V. Popovic, and Ottilia Saxl. Spectroscopic ellipsometry and polarimetry for materials and systems analysis at the nanometer scale: State-of-the-art, potential, and perspectives. *Journal of Nanoparticle Research*, 11(7):1521–1554, 2009.

[134] Enrico Costa, Paolo Soffitta, Ronaldo Bellazzini, Alessandro Brez, Nicholas Lumb, and Gloria Spandre. An efficient photoelectric X-ray polarimeter for the study of black holes and neutron stars. *Nature*, 411(6838):662–665, 2001.

[135] B. W. Lites, M. Kubo, H. Socas-Navarro, T. Berger, Z. Frank, R. Shine, T. Tarbell, A. Title, K. Ichimoto, Y. Katsukawa, S. Tsuneta, Y. Suematsu, T. Shimizu, and S. Nagata. The Horizontal Magnetic Flux of the Quiet-Sun Internetwork as Observed with the Hinode Spectro-Polarimeter. *The Astrophysical Journal*, 672(2):1237–1253, 2008.

[136] Michael F. Sterzik, Stefano Bagnulo, and Enric Palle. Biosignatures as revealed by spectropolarimetry of Earthshine. *Nature*, 483(7387):64–66, 2012.

[137] David S. Greenfield, Robert W. Knighton, and Xiang Run Huang. Effect of corneal polarization axis on assessment of retinal nerve fiber layer thickness by scanning laser polarimetry. *American Journal of Ophthalmology*, 129(6):715–722, 2000.

[138] Jérémy Vizet, Jean Rehbinder, Stanislas Deby, Stéphane Roussel, André Nazac, Ranya Soufan, Catherine Genestie, Christine Haie-Meder, Hervé Fernandez, François Moreau, and Angelo Pierangelo. In vivo imaging of uterine cervix with a Mueller polarimetric colposcope. *Scientific Reports*, 7(1):1–12, 2017.

[139] David J Diner, Ab Davis, Bruce Hancock, Gary Gutt, Russell a Chipman, and Brian Cairns. Dual-photoelastic-modulator-based polarimetric imaging concept for aerosol remote sensing. *Applied optics*, 46(35):8428–8445, 2007.

[140] R. Imazawa, Y. Kawano, T. Ono, and K. Itami. Development of real-time rotating waveplate Stokes polarimeter using multi-order retardation for ITER poloidal polarimeter. *Review of Scientific Instruments*, 87(1), 2016.

[141] Peng Liu, Xiaofeng Li, John J. Qu, Wenguang Wang, Chaofang Zhao, and William Pichel. Oil spill detection with fully polarimetric UAVSAR data. *Marine Pollution Bulletin*, 62(12):2611–2618, 2011.

[142] Guannan Li, Ying Li, Bingxin Liu, Peng Wu, and Chen Chen. Marine oil slick detection based on multi-polarimetric features matching method using polarimetric synthetic aperture radar data. *Sensors (Switzerland)*, 19(23), 2019.

[143] David B Chenault, Justin P Vaden, Douglas A Mitchell, and Erik D Demicco. New IR polarimeter for improved detection of oil on water. *SPIE Newsroom*, pages 3–6, 2016.

[144] Pierre Yves Deschamps, Jean Claude Buriez, François Marie Bréon, Marc Leroy, Alain Podaire, Annick Bricaud, and Geneviève Sèze. The POLDER Mission: Instrument Characteristics and Scientific Objectives. *IEEE Transactions on Geoscience and Remote Sensing*, 32(3):598–615, 1994.

[145] Roselyne Lacaze, Jing M. Chen, Jean Louis Roujean, and Sylvain G. Leblanc. Retrieval of vegetation clumping index using hot spot signatures measured by POLDER instrument. *Remote Sensing of Environment*, 79(1):84–95, 2002.

[146] Frans Snik, Julia Craven-Jones, Michael Escuti, Silvano Fineschi, David Harrington, Antonello De Martino, Dimitri Mawet, Jérôme Riedi, and J. Scott Tyo. An overview of polarimetric sensing techniques and technology with applications to different research fields. 9099:90990B, 2014.

[147] Frans Snik, Christoph Keller, David Doelman, Jonas Kühn, Lucas Patty, Jens Hoeijmakers, Vidhya Pallichadath, Daphne Stam, Antoine Pommerol, Olivier Poch, and Brice-Olivier Demory. A snapshot full-Stokes spectropolarimeter for detecting life on Earth. *arXiv*, (May):10, 2019.

[148] William B. Sparks, Thomas A. Germer, and Rebecca M. Sparks. Classical polarimetry with a twist: A compact, geometric approach. *Publications of the Astronomical Society of the Pacific*, 131(1001):75002, 2019.

[149] W. B. Sparks, J. H. Hough, L. Kolokolova, T. A. Germer, F. Chen, S. DasSarma, P. DasSarma, F. T. Robb, N. Manset, I. N. Reid, F. D. Macchetto, and W. Martin. Circular polarization in scattered light as a possible biomarker. *Journal of Quantitative Spectroscopy and Radiative Transfer*, 110(14-16):1771–1779, 2009.

[150] Richard J. Maude, Wanchana Buapetch, and Kamolrat Silamut. Short report: A simplified, low-cost method for polarized light microscopy. *American Journal of Tropical Medicine and Hygiene*, 81(5):782–783, 2009.

[151] D. W. I. Ramadhani, S. I. T. I. Nurhayati, and T. U. R. Rahardjo. Haemozoin Detection in Mouse Liver Histology Using Simple Polarized Light Microscope. *Hayati Journal of Biosciences*, 21(1):48–52, 2014.

[152] Chao Chen, Liang Gao, Wanru Gao, Cong Ge, Xinyuan Du, Zha Li, Ying Yang, Guangda Niu, and Jiang Tang. Circularly polarized light detection using chiral hybrid perovskite. *Nature Communications*, 10(1):1–7, 2019.

[153] Sanaz Alali and Alex Vitkin. Polarized light imaging in biomedicine: emerging Mueller matrix methodologies for bulk tissue assessment. *Journal of Biomedical Optics*, 20(6):061104, 2015.

[154] José J. Gil. Review on Mueller matrix algebra for the analysis of polarimetric measurements. *Journal of Applied Remote Sensing*, 8(1):081599, 2014.

[155] Eric Compain and Bernard Drevillon. Polarimeter Based on Uncoated Prisms. *Applied Optics*, 1998.

[156] Wei-Liang Hsu, Graham Myhre, Kaushik Balakrishnan, Neal Brock, Mohammed Ibn-Elhaj, and Stanley Pau. Full-Stokes imaging polarimeter using an array of elliptical polarizer. *Optics Express*, 22(3):3063, 2014.

[157] Gerard van Harten, Frans Snik, Jeroen H. H. Rietjens, J. Martijn Smit, and Christoph U. Keller. Spectral line polarimetry with a channeled polarimeter. *Applied Optics*, 53(19):4187, 2014.

[158] Yanwei Liu, Grenville A. Jones, Yong Peng, and Tiehan H. Shen. Generalized theory and application of Stokes parameter measurements made with a single photoelastic modulator. *Journal of Applied Physics*, 100(6), 2006.

[159] Oriol Arteaga, John Freudenthal, Baoliang Wang, and Bart Kahr. Mueller matrix polarimetry with four photoelastic modulators: theory and calibration. *Applied Optics*, 51(28):6805, 2012.

[160] Juan M. Bueno. Polarimetry using liquid-crystal variable retarders: Theory and calibration. *Journal of Optics A: Pure and Applied Optics*, 2(3):216–222, 2000.

[161] Alba Peinado, Angel Lizana, Josep Vidal, Claudio Iemmi, and Juan Campos. Optimized Stokes polarimeters based on a single twisted nematic liquid-crystal device for the minimization of noise propagation. *Applied Optics*, 50(28):5437, 2011.

[162] Jintao Chang, Nan Zeng, Honghui He, Yonghong He, and Hui Ma. Single-shot spatially modulated Stokes polarimeter based on a GRIN lens. *Optics Letters*, 39(9):2656, 2014.

[163] P. S. Hauge. Mueller matrix ellipsometry with imperfect compensators. *Journal of the Optical Society of America*, 68(11):1519, 1978.

[164] D S Sabatke, M R Descour, E L Dereniak, W C Sweatt, S A Kemme, and G S Phipps. Optimization of retardance for a complete Stokes polarimeter. *Opt. Lett.*, 25(11):802–804, 2000.

[165] Chao He and Martin J Booth. Full poincaré polarimetry for enhanced microscopic sensing. In *Biophotonics Congress 2021*, page NM1C.2. Optical Society of America, 2021.

[166] Thomas Bauer, Peter Banzer, Ebrahim Karimi, Sergej Orlov, Andrea Rubano, Lorenzo Marrucci, Enrico Santamato, Robert W. Boyd, and Gerd Leuchs. Observation of optical polarization Möbius strips. *Science*, 347(6225):964–966, 2015.